Switchable waveguiding in photonic liquid crystal microstructures

Von der Fakultät für Naturwissenschaften
der Universität Paderborn akzeptierte
DISSERTATION
zur Erlangung des akademischen Grades eines
Doktors der Naturwissenschaften
- Dr. rer. nat. –

von
Alexander Lorenz, M.Sc.
(aus Korbach)
Paderborn 2010

Die vorliegende Arbeit entstand im Zeitraum Oktober 2007 bis Juni 2010 im Fachgebiet Physikalische Chemie (Arbeitskreis Prof. Dr. Kitzerow) der Fakultät für Naturwissenschaften der Universität Paderborn.

1. Gutachter: Prof. Dr. Heinz-Siegfried Kitzerow
2. Gutachter: Prof. Dr. Rolf Schuhmann

Die Arbeit wurde eingereicht am: 2.6.2010
Tag der mündlichen Prüfung: 1.7.2010

Danksagung

Mein besonderer Dank gilt Herrn Prof. Dr. Heinz-Siegfried Kitzerow für die interessante Themenstellung und die vielfältige Förderung während der gesamten Promotionszeit und bereits davor. Ich bedanke mich außerdem für die hervorragenden Arbeitsbedingungen die grundlegend zu einem so schnellen Gelingen dieser Arbeit beigetragen haben.

Bei Herrn Prof. Dr. Rolf Schuhmann bedanke ich mich für wichtige Impulse und Anregungen sowie für die Unterstützung beim Bearbeiten eines für mich teils völlig neuen Themenbereichs. Natürlich bedanke ich mich darüber hinaus für das bereitwillige Übernehmen des Korreferates.

Für die Einführung in die grundlegenden experimentellen Techniken mit den verschiedensten Typen von Glasfasern, sowie für das Bereitstellen von Proben Photonischer Kristallfasern bedanke ich mich bei Herrn Prof. Dr. Hartmut Bartelt, Herrn Dr. Jens Kobelke und Frau Anka Schwuchow am IPHT Jena.

Der Deutschen Forschungsgemeinschaft danke ich für die Förderung des Projektes im Rahmen des Graduiertenkollegs 1464 „Mikro- und Nanostrukturen in Optoelektronik und Photonik“. Ich bedanke mich auch bei allen Teilnehmern des Graduiertenkollegs für die tolle Atmosphäre bei den gemeinsamen Aktivitäten. In diesem Sinne bedanke ich mich besonders bei Frau Olga Kasdorf, Frau Marina Panfilova, Herrn Frank Bayer, Herrn Christoph Classen, Herrn Stephan Declair, Herrn Torsten Frers und Herrn Andreas Redler.

Allen Mitarbeiterinnen und Mitarbeitern der Physikalischen Chemie danke ich für das hervorragende Arbeitsklima und die angenehme Atmosphäre. Besonders Frau Gisela Jünnemann hat durch Ihre zuverlässige Unterstützung bei der Präparation der filigranen Proben entscheidend zum zügigen Fortschreiten der Experimente beigetragen. Für die Unterstützung bei einer Vielzahl von organisatorischen Abläufen bedanke ich mich bei Frau Isabella Koralewicz. Für vielfältige technische Unterstützung und Diskussionsbereitschaft sei an dieser Stelle Herrn Dr. Andreas Hoischen gedankt. Herrn Dr. Karl Hiltrop danke ich für die Aufnahmen mit dem Rasterelektronenmikroskop. Bei Herrn Frank Bayer, Herrn Dr. Andreas Hoischen, Herrn Dr. Sebastian Lages und Herrn Dr. Richard Szopko bedanke ich mich für die freundschaftliche Atmosphäre während der Arbeit und darüber hinaus. Herrn Dr. Sebastian Lages danke ich außerdem für das Proofreading.

Den Mitarbeitern der mechanischen Werkstatt danke ich für ihre professionelle und begeisterte Unterstützung bei der Konstruktion und für die Herstellung der aufwändigen mechanischen Teile des spektral auflösenden Jelly´schen Mikrorefraktometers und anderer Geräte.

Mein Dank gilt außerdem allen Aktiven des GDCh Jungchemikerforums (JCF) in Paderborn für das Gelingen zahlreicher Veranstaltungen - besonders für die fantastische Beteiligung am „JCF International Get-Together“. Herrn Stephan Cludius-Brandt danke ich besonders weil wir diese Veranstaltungsreihe gemeinsam ins Leben gerufen haben. Herrn Sebastian Lange danke ich für die publikumswirksamen Verlosungen. Bei Frau Ramona Wortmann, Frau Mareike Busse und Frau Sandra Janke bedanke ich mich für die schöne produktive gemeinsame Zeit im Paderborner JCF-Vorstand („Sprecherteam“).

Meinen Eltern danke ich für ihre große Unterstützung während des Studiums und während der Promotion. Ohne sie wäre dies alles nicht möglich gewesen.

Sometimes, caught between dreaming and waking,

the human mind is surprisingly attracted by formulas:

Adding 1 to the square of a number $x \in \boldsymbol{N}$ *and subtracting the square of its next smaller neighbor* $(x-1)^2$ *results 2x:* $x = \frac{1 + x^2 - (x-1)^2}{2}$.

The square of this number x can be calculated by taking the sum of the first x uneven numbers:

$$x^2 = \sum_{k=1}^{x} (2k-1).$$

Kurzfassung

Die vorliegende Dissertation behandelt die Untersuchung der Lichtwellenleiter-eigenschaften von flüssigkristallgefüllten mikrostrukturierten Glasfasern.
Diese Photonischen Kristallfasern verfügen über eine zweidimensional periodisch mikrostrukturierte Querschnittsfläche, die das Führen von Licht mit einer Ausbreitungskonstanten senkrecht zum Faserquerschnitt erlaubt. Licht kann in diesen Fasern über längere Distanzen geführt werden. Bereits die ersten technisch realisierten Typen Photonischer Kristallfasern waren in vielen Bereichen konventionellen Glasfasern überlegen, wie z. B. dem Kerndurchmesser von sog. Einmodenfasern, die in der Lasertechnik Anwendung finden. In Photonischen Kristallfasern kann auch über lange Distanzen von Lichtführungsmechanismen mit hochbrechendem Cladding Gebrauch gemacht werden. Als Cladding wird die nächste Umgebung des lichtführenden Kerns bezeichnet. Prinzipiell ist eine ausreichend hohe Reflektivität des Claddings erforderlich, um Licht im Kernbereich eines Lichtwellenleiters einzuschließen und so zu führen.
Flüssigkristalle zeigen hochinteressante optische Eigenschaften. Aufgrund ihres fluiden Charakters und ihrer herausragenden optischen Anisotropie sind sie prädestiniert, um als aktive Elemente in optischen Modulatoren angewendet zu werden. Obwohl typische nematische Flüssigkristalle im sichtbaren und nahen infraroten Spektralbereich kaum absorbieren, zeigen sie dennoch eine hohe und zudem anisotrope optische Dämpfung. Die Anwendung von Flüssigkristallen als Kernmaterial für Lichtwellenleiter ist deswegen nur begrenzt möglich. Für faseroptische Modulatoren sind allerdings vergleichsweise kurze Faserstücke mit Längen im Zentimeterbereich eher von Interesse als extrem lange Fasern.
Es hat sich in den letzten Jahren etabliert, das zweidimensional periodisch mikrostrukturierte Cladding von geeigneten Photonischen Kristallfasern mit Flüssigkistallen zu füllen. Im Rahmen dieser Dissertation wird eine Technik zum homogenen Füllen längerer Faserstücke entwickelt, um systematische Analysen durchzuführen. Die Dämpfungseigenschaften flüssigkristallgefüllter Photonischer Kristallfasern und ihr Schaltverhalten werden experimentell und mithilfe von elektromagnetischen Feldsimulationen untersucht.
Es wird experimentell gezeigt, dass zwei gefüllte Photonische Quarzglasfasern mit festem Kern im sichtbaren Spektralbereich strukturierte Dämpfungsspektren mit spektralen Bereichen kleiner Dämpfung zeigen. Die Dämpfung innerhalb dieser Bereiche kann Werte kleiner als 1 dB/cm erreichen. Schaltexperimente führen zu faseroptischen Modulatoren, die polarisationsunabhängige und polarisationsabhängige Effekte zeigen. Darüber hinaus werden die elektrooptischen Schaltzeiten optimiert.
Die Dämpfungseigenschaften der Fasern werden mit elektromagnetischen Feldsimulationen nachvollzogen. Dabei wird als Dämpfungsmodell die Lichtstreuung aufgrund der thermischen Fluktuation der mittleren molekularen Orientierung des Flüssigkristalls verwendet. Die Einflussparameter des experimentellen Systems werden in den Simulationen abgebildet. Die Übereinstimmung der experimentellen Ergebnisse und der Simulationsergebnisse ist geeignet, um detaillierte Einblicke in die Funktionsweise des untersuchten Systems zu gewähren.

Abstract

This dissertation is focused on the investigation of the waveguiding properties of liquid crystal-filled microstructured fibers. These photonic crystal fibers exhibit a two-dimensional periodic microstructured profile. The latter microstructure enables the guidance of electromagnetic radiation with a propagation constant perpendicular to the profile. Light can be guided in these fibers over longer distances. Even the first photonic crystal fibers in practical existence had superior waveguiding properties compared to conventional optical fibers. For example, single-mode fibers, which are used in laser applications, could be improved by enhancing the core diameter. Furthermore, waveguiding mechanisms with a high index cladding can be applied in photonic crystal fibers in order to guide light over large distances. 'Cladding' is a technical term for the surrounding of the waveguiding core region of a fiber. Generally, a high reflectivity of the cladding is required in order to confine and guide light in the core.

Liquid crystals show highly interesting optical properties. These fluidic and optically highly anisotropic substances are predetermined to be applied as active elements in optical modulators. Typical nematic liquid crystals are only weakly absorbing in the visible and near infrared spectral region. Even though, the latter show a high and additionally anisotropic optical damping. The application as core material in terms of waveguides is possible only very limitedly for liquid crystals. However, only relatively short fibers in the range of several to several tens of millimeters are required in the field of fiberoptical modulators.

It is well established to fill the microstructured cladding of selected photonic crystal fibers with liquid crystals. In the current dissertation, a technique is developed to homogeneously fill rather long pieces of photonic crystal fibers. Systematical investigations are conducted. The attenuation properties and the switching characteristics of liquid crystal-filled photonic crystal fibers are investigated experimentally and by means of electromagnetic field simulations.

Two liquid crystal-filled microstructured silica glass fibers are investigated in the experimental part. The fibers show structured attenuation spectra with intervals of small attenuations where values even lower than 1 dB/cm are achieved. Fiber optical modulators are shown in switching experiments where polarization dependent and independent responses are investigated. Moreover, the response times of these modulators are optimized.

Electromagnetic field simulations are conducted in order to obtain approximate theoretical attenuation spectra. In this model, the light scattering due to thermal fluctuations of the molecular orientation of the liquid crystal is considered as damping mechanism. The parameters of the experimental system are considered in the simulations. Reasonable agreement of the simulations and the experimental results is obtained. Thus, the simulation can be used as a tool in order to understand the attenuation properties of real fibers in more detail.

Contents

1. Introduction

Light in the ultraviolet, visible and infrared spectral region is required for the visual inspection of surfaces, the characterization of transparent and absorbing materials, the transmission of signals over any conceivable distances, and the manipulation of photo active systems.

In the field of integrated optics or in displays, waveguides are applied in order to guide light over short distances. Flexible waveguides with intermediate length where light is guided in liquids or bundles of thin fibers are useful to construct high power cold light sources. The transmission of light signals in specialized waveguides with length > 100 km is nowadays practical applied in long-haul fiber optic communication systems. One half of the Nobel Prize in Physics was awarded to Charles K. Kao in 2009 ‘for groundbreaking achievements concerning the transmission of light in fibers for optical communication’. In 1966, Kao calculated carefully that ‘with a fiber of purest glass it would be possible to transmit light signals over 100 kilometers – compared to only 20 meters in the 1960s’ [1].

Conventional optical fibers [2,3] consist of an all-solid structure where a glass core with a high refractive index is surrounded by a cladding region which consists of a glass with a lower refractive index. The light is guided in the core region due to total internal reflection [4]. The waveguiding properties of conventional optical fibers can be extensively modified by adjusting the core size and the refractive index contrast of the different glasses [2]. Losses even lower than 0.5 $dB \cdot km^{-1}$ can be achieved due to glasses with high purity in conventional single-mode optical fibers [8]. Small refractive index contrasts and adequate gradual doping rather than drastic index steps are applied. Careful design leads to selective propagation of just one core mode with low losses in a selected wavelength region (within the infrared spectral region).

Generally, light can be guided and delivered safely in fiber optics. The high energy density of coherent light is maintained due to outstanding confinement in a small core region of fiber optical waveguides. Just as well, weak signals can be guided over long distances in order to be evaluated with e. g. a single photon detector. Furthermore, it is possible to manipulate the transmission of light, to amplify, or to filter the intensity of the guided radiation in active waveguides.

Since the last 14 years, photonic crystal fibers are in practical existence [5,6]. These fibers with a periodic transverse microstructure open new possibilities to design waveguides with outstanding properties. In hollow core fibers, the light is guided in air so that absorption losses by the glass become less important. The waveguiding is due to photonic bandgaps of the cladding. Consequently, the refractive index of the waveguiding core can very well be smaller than the average refractive index of the cladding in these fibers. Compared to conventional optical fibers, the variety of transmission characteristics of photonic crystal fibers is enriched by all possible features of a periodic transverse microstructure. This can lead to bandgap or index guiding depending on the application. Additionally, the high optical nonlinearity, group velocity dispersion or sensibility to external control parameters make photonic crystal fibers suitable for frequency conversion or intensity modulation, thereby enabling active fiber optical devices with limited length, where absorption is negligible.

Surprisingly, all-solid photonic band gap fibers have become candidates to achieve low attenuations by applying the photonic band gap effect and maintaining an all-solid structure [5,7,8,9]. Commonly, in this type of fiber, cylindrical high index inclusions in a background material with lower refractive index are arranged in a trigonal array forming a 2-dimensional microstructure. In the center of this microstructure, one inclusion is missing and guided modes are confined in this central low index core. Such fibers show attenuation spectra where low-loss windows are separated by regions with high losses. All-solid photonic band gap fibers were discussed as simple bandgap fibers [10] where the waveguiding properties are determined by resonances of the entities in the cladding [11,12].

Principally, there are two ways to realize all-solid microstructured fibers. Fibers longer than several meters are drawn from a macroscopic preform already consisting of the intended materials in an adequate geometry [7,9]. But also, shorter pieces suffice for optical modulators or filters. A fiber with air inclusions can be filled with high index materials. Such short pieces of all-solid photonic band gap fibers have been demonstrated by pressing molten high index tellurite glass into a microstructured silica glass fiber with a silica glass core surrounded by an array of air inclusions [13].

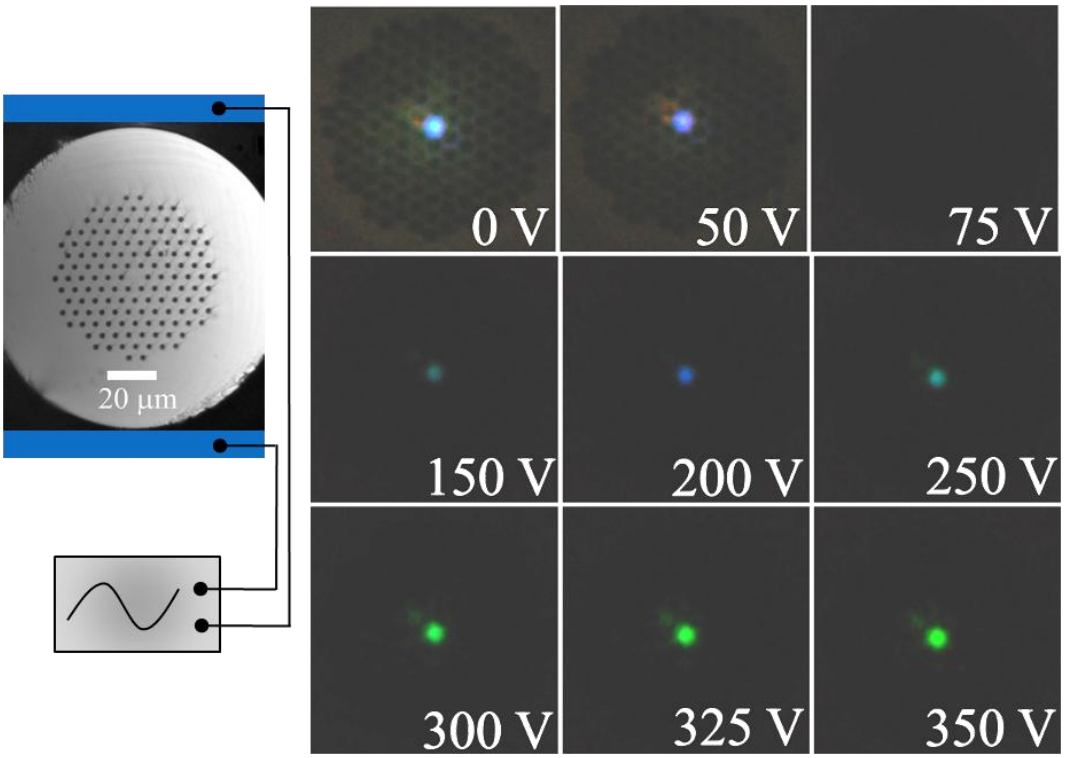

Fig. 1. Optical micrographs of a photonic crystal fiber (LMA-8, NKT-photonics) filled with the liquid crystal E7, planar anchoring. White light is coupled to the core. After a propagation length of 15 mm, the color coordinates of the transmitted light correspond to blue in the 0 V-state. A.c. (1 kHz) voltages are applied transversal to the propagation direction as indicated to the left. The indicated voltages are V_{rms}. The color vanishes if the voltage exceeds a threshold. At higher voltages, the transmission of green light appears.

Photonic crystal fibers with air inclusions can easily be filled with isotropic liquids or liquid crystals. While bulk wave guiding in liquid crystals is limited by high attenuation in the range of 20 to 40 $dB \cdot cm^{-1}$[14,15], a solid core photonic crystal fiber with liquid crystal-filled inclusions exhibits guided core modes which have just small field components in the liquid crystal-filled sections. Consequently, solid core photonic crystal fibers with a high index liquid crystal-filled microstructure show lower attenuation than microstructured fibers with nematic liquid crystals in the core. The optical properties of liquid crystals are highly sensitive to the external conditions [16]. In photonic crystal fibers with liquid crystal inclusions, wave guiding becomes possible combining the intense, fast, and reversible response of liquid crystals with reasonable transmission. Altogether, liquid crystal-filled photonic crystal fibers are active fibers where thermal [17-23], electrical [20-23, 24-31], and optical [22-24, 32] tuning of the attenuation properties are feasible.

The optical properties of the liquid crystal inclusions depend strongly on the molecular alignment inside the inclusions and the dielectric permittivity is a tensor of second rank. Accordingly, the attenuation properties of liquid crystal-filled inclusions are commonly treated theoretically with electromagnetic field simulations rather than with analytical approximations. Some groups have studied basic effects theoretically assuming a uniform alignment of the liquid crystals [33,34,35]. Currently, there is a trend of using more realistic expressions for the anisotropic dielectric permittivity tensor in the liquid crystal-filled regions [26,36,37].

To mention two examples, theoretical investigations considering the infrared spectral region were published for a fiber [36] with splay aligned nematic liquid crystals and for a similar system using a fiber with larger inclusion diameters [26]. The infrared transmission spectra were estimated by calculating the coupling loss of a filled and an unfilled photonic crystal fiber eventually taking into account the influence of external electric fields in these works.

Systematical variations of the fiber structure and investigations in the visible spectral region are still necessary. This work is intended to give such a systematical analysis of photonic crystal fibers with cylindrical liquid crystal-filled inclusions. In the experimental part, two commercial photonic crystal fibers are filled with nematic liquid crystals. Each of the fibers consists of fused silica and has a solid core, which is surrounded by a regular lattice of cylindrical inclusions with uniform diameter. The inclusion radii of the two fibers are 1.2 μm and 1.5 μm, respectively. Thus, the inclusion radii are systematically varied in the experiments. The anchoring condition of the liquid crystal and accordingly the molecular alignment inside the inclusions is varied, additionally. A spectroscopic setup is constructed in order to record adequate attenuation spectra of the filled fibers by using the well-known cut-back technique. Furthermore, addressing experiments are conducted with a two and a four electrode setup in order to vary the attenuation properties of the fibers. These addressing experiments show highly interesting polarization dependent and independent effects with short response times. In the theoretical part, electromagnetic field simulations are conducted where the complete fiber geometry and the dispersion of the materials are considered. The simulations are based on the assumption that the propagation losses are caused by scattering due to thermal fluctuations of the molecular alignment of the liquid crystal.

2. Background

2.1 Waveguiding

Guiding of sound or electromagnetic energy in material structures requires appropriate materials and a guiding mechanism with low damping to provide a controlled energy delivery at the output and low losses.

Due to the wave–particle duality, electromagnetic energy shows both wave-like and particle-like properties. Sound (phonons) and electromagnetic energy (photons) can be treated as waves. The propagation of phonons and photons in matter is in particular due to their wave nature and thus, guiding structures for these are named waveguides.

An appropriate description of electromagnetic waves inside a waveguide is given by Maxwell's equations (with the total charge density ρ):

$$\nabla \times \vec{H} = \vec{J}_f + \frac{\partial}{\partial t}\vec{D}, \qquad \text{(Eq. 1)}$$

$$\nabla \times \vec{E} = -\frac{\partial}{\partial t}\vec{B}, \qquad \text{(Eq. 2)}$$

$$\nabla \cdot \vec{D} = \rho, \qquad \text{(Eq. 3)}$$

$$\nabla \cdot \vec{B} = 0. \qquad \text{(Eq. 4)}$$

Maxwell-Ampères's law (Eq. 1) relates the magnetic field $\vec{H}$ to the free current density $\vec{J}_f$ and the time derivative of the electric flux energy density. Faraday's law (Eq. 2) relates the electric field $\vec{E}$ to the time derivative of the magnetic flux density $\vec{B}$. The product of $\vec{E}$ and the electric conductivity σ_{el} is assumed to be equal to the free current density σ_{el} $\left(\vec{J}_f = \sigma_{el}\vec{E}\right)$. The correlations of the dielectric displacement $\vec{D}$ with $\vec{E}$ and the magnetic displacement $\vec{B}$ with $\vec{H}$ are assumed to be linear ($\vec{D} = \varepsilon_r\varepsilon_0\vec{E}$, $\vec{B} = \mu_r\mu_0\vec{H}$; linear materials). Here ε_0 is the dielectric permittivity of the vacuum, ε_r the relative dielectric permittivity inside a material, μ_0 the magnetic permeability of the vacuum, and μ_r the magnetic permeability inside a material. The two curl equations are then transformed:

$$\nabla \times \vec{H} = \sigma_{el}\vec{E} + \frac{\partial \varepsilon_r \varepsilon_0 \vec{E}}{\partial t}$$
$$\Leftrightarrow \varepsilon_r^{-1} \nabla \times \vec{H} = \varepsilon_r^{-1}\sigma_{el}\vec{E} + \frac{\partial \varepsilon_0 \vec{E}}{\partial t} \qquad \text{(Eq. 5)}$$

$$\nabla \times \vec{E} = -\mu_r \mu_0 \frac{\partial \vec{H}}{\partial t} \qquad \text{(Eq. 6)}$$

The relative dielectric constant is scalar for isotropic materials and a tensor of second rank for anisotropic materials like liquid crystals. The two equations 5 and 6 can be combined. Taking the curl of Eq. 5 and considering that the Nabla-operator ∇ is not time dependent results:

$$\nabla \times \left(\varepsilon_r^{-1} \nabla \times \vec{H}\right) = \nabla \times \left(\varepsilon_r^{-1}\sigma_{el}\vec{E} + \varepsilon_0 \frac{\partial}{\partial t}\vec{E}\right)$$
$$\Leftrightarrow \nabla \times \left(\varepsilon_r^{-1} \nabla \times \vec{H}\right) = \nabla \times \sigma_{el}\varepsilon_r^{-1}\vec{E} + \varepsilon_0 \frac{\partial}{\partial t}\nabla \times \vec{E}. \qquad \text{(Eq. 7)}$$

The right side of Eq. 7 can be further transformed. Generally, the second summand, which contains no spatial derivatives, can be replaced by using Eq. 6. The conductivity and the dielectric tensor can be assumed constant $\left(\sigma_{el,iso},\ \varepsilon_{r,iso}^{-1}\right)$ in the case of isotropic, homogeneous materials, where the relative dielectric constant is not dependent on the spatial variables. Under these circumstances, $\nabla \times \vec{E}$ in the first summand can as well be replaced by using Eq. 6. Thereby, the dependences of the electric field are eliminated:

$$\nabla \times \left(\varepsilon_{r,iso}^{-1} \nabla \times \vec{H}\right) = -\mu_0 \mu_r \sigma_{el,iso} \varepsilon_{r,iso}^{-1} \frac{\partial}{\partial t}\vec{H} - \mu_r \mu_0 \varepsilon_0 \frac{\partial^2}{\partial t^2}\vec{H}. \qquad \text{(Eq. 8)}$$

In a similar approach, the dependences of the magnetic field can be eliminated by taking the curl of Eq. 6 and inserting Eq. 5. This time, a constant relative magnetic permeability $\mu_{r,iso}$ is considered in the last step:

$$\nabla \times \left({\mu_r}^{-1} {\mu_0}^{-1} \nabla \times \vec{E}\right) = -\nabla \times \frac{\partial}{\partial t}\vec{H}$$
$$\Leftrightarrow \nabla \times \left({\mu_r}^{-1} {\mu_0}^{-1} \nabla \times \vec{E}\right) = -\frac{\partial}{\partial t}\nabla \times \vec{H}, \qquad \text{(Eq. 9)}$$

$$\nabla \times \left(\nabla \times \vec{E}\right) = -\frac{\partial}{\partial t}\mu_{r,iso}\mu_0\sigma_{el}\vec{E} - \frac{\partial^2}{\partial t^2}\mu_{r,iso}\mu_0\varepsilon_r\varepsilon_0\vec{E}. \qquad \text{(Eq. 10)}$$

Eq. 8 and Eq. 10 have both the form of damped wave equations [4]. The damping term contains the first time derivative of the respective field variable and the electric conductivity. This type of loss (ohmic loss [4]) can be neglected for

dielectric materials $(\sigma_{el} = 0)$. In contrast, absorption losses and scattering losses occur in dielectric materials very well. The relative magnetic permeability of numerous dielectric materials can be approximated by the relative permeability of the vacuum $(\mu_r = 1)$. For ideal dielectric materials, the differential equations Eq. 8 and Eq. 10 are thus transformed into wave equations where the second spatial derivatives of the particular field variable appear in one term and the second time derivative of the particular field variable appears in one additional term.

The wave equations can be rewritten with the expression $c_0 = (\varepsilon_0 \mu_0)^{-1/2}$ for the speed of light in vacuum. Here, a dielectric constant ε_r with spatial dependences can be used again.

$$\nabla \times \left(\varepsilon_r^{-1} \nabla \times \vec{H}\right) = -\frac{1}{c_0^2} \frac{\partial^2}{\partial t^2} \vec{H}, \qquad \text{(Eq. 11)}$$

$$\nabla \times \left(\nabla \times \vec{E}\right) = -\frac{\varepsilon_r}{c_0^2} \frac{\partial^2}{\partial t^2} \vec{E}. \qquad \text{(Eq. 12)}$$

An electromagnetic problem in dielectric media like the propagation of electromagnetic radiation in waveguiding structures can be completely described by solving the wave equation for the magnetic field (Eq. 11). The respective geometry, the respective dielectric functions ε_r and adequate boundary conditions have to be considered in this description (with the refractive index $n^2 = \varepsilon_r \mu_r$).

$$\vec{H} = \vec{H}_0 \cos(\omega t - n\vec{k}_0 \vec{r}) = \mathrm{Re}\left(\vec{H}_0 e^{-jn\vec{k}_0 \vec{r}} e^{j\omega t}\right) = \mathrm{Re}\left(\vec{H}_{sp} e^{j\omega t}\right) \qquad \text{(Eq. 13)}$$

$$\begin{aligned}
&\nabla \times \left(\varepsilon_r^{-1} \nabla \times \vec{H}\right) = -\frac{1}{c_0^2} \frac{\partial^2}{\partial t^2} \mathrm{Re}\left(\vec{H}_{sp} e^{j\omega t}\right) \\
\Leftrightarrow\ &\nabla \times \left(\varepsilon_r^{-1} \nabla \times \vec{H}\right) = -\frac{1}{c_0^2} \mathrm{Re}\left(\vec{H}_{sp} \frac{\partial^2}{\partial t^2} e^{j\omega t}\right) \\
\Leftrightarrow\ &\nabla \times \left(\varepsilon_r^{-1} \nabla \times \vec{H}\right) = \frac{1}{c_0^2} \mathrm{Re}\left(\vec{H}_{sp} \omega^2 e^{j\omega t}\right) \\
\Leftrightarrow\ &\nabla \times \left(\varepsilon_r^{-1} \nabla \times \vec{H}\right) = k_0^2\, \mathrm{Re}\left(\vec{H}_{sp} e^{j\omega t}\right) \\
\Leftrightarrow\ &\nabla \times \left(\varepsilon_r^{-1} \nabla \times \vec{H}_{sp}\right) = k_0^2 \vec{H}_{sp}
\end{aligned} \qquad \text{(Eq. 14)}$$

Inserting the time harmonic ansatz Eq. 13 for a propagating wave (characterized by the vacuum wave vector $\left|\vec{k}_0\right| = \omega / c_0$ and the complex valued spatial amplitude $\vec{H}_{sp}$) into the wave equation Eq. 11 yields Eq. 14. This differential equation is the formulation of an eigenvalue problem for the wave function $\vec{H}$. A valid solution is a wave function $\vec{H}$ which by application of the left side operator transforms into itself multiplied by a constant factor, the eigenvalue $k_0^{\,2}$. The solutions for this type of eigenvalue problem are referred to as modes. A mode consists of a valid wave function $\vec{H}$, its eigenvalue and additionally the electric wave function which is provided by the curl equation Eq. 5. This is shown by using the time harmonic ansatz Eq. 13 and considering again $\sigma_{el} = 0$. Thus, the electric field is easily obtained from a known magnetic field function:

$$\begin{aligned} \nabla \times \vec{H} = \varepsilon_0 \varepsilon_r \vec{E}_{sp} \frac{\partial}{\partial t} e^{j\omega t} &= j\omega \varepsilon_0 \varepsilon_r \vec{E} \\ \Leftrightarrow \vec{E} &= \frac{\nabla \times \vec{H}}{j\omega \varepsilon_0} \varepsilon_r^{-1}. \end{aligned} \qquad \text{(Eq. 15)}$$

The time averaged flux density of electromagnetic energy is described by the Poynting vector [4]:

$$\bar{S} = \frac{1}{2} \mathrm{Re}\left(\vec{E}_{ph} \times \vec{H}_{ph}^{\,*}\right) \qquad \text{(Eq. 16)}$$

In this formula (Eq. 16), $\vec{E}_{ph}$ is a complex electric field amplitude and $\vec{H}_{ph}^{\,*}$ is the conjugate complex of a magnetic field amplitude (phasor form, see 'Time averaged flux of electromagnetic energy' in the appendix). For photons, the time averaged flux of electromagnetic energy is also commonly referred to as intensity.

In summary, electromagnetic energy transport on well defined pathways can be described by Maxwell's equations. The question how much of the input intensity is still present at the output is discussed in the following chapter.

2.1.1 Attenuation

The transfer of energy over some distance from an arbitrary source such as an antenna or an emitting molecule to a random receiver is necessarily burdened with loss - even in the vacuum where no energy conversion takes place. This becomes

clear by a gedankenexperiment with a transmitter/receiver setup in free space under the assumption that transmitter and receiver have approximately the same size. If no energy conversion occurs, the integral over the iradiated intensity I_r remains constant on any random surface A surrounding the source:

$$const = \int_A I_r dA. \qquad \text{(Eq. 17)}$$

Consequently, the time averaged energy density $I = \int_A I_r dA \Big/ A$ of the electromagnetic radiation steadily decreases with growing propagation distance r because the surface A grows proportional to r^2 . If source and receiver have approximately the same size $A_{source} = A_{receiver}$, the maximum receivable energy is necessarily smaller than the emitted energy (if more than one photon is transmitted):

$$\max\left(IA_{receiver}\right) < \int_A I_r dA \qquad \text{(Eq. 18)}$$

Energy can only be transferred to a receiver partially; the power at the receiver $P_{receiver}$ is smaller than the power emitted by the source P_{source}. A measure T for the quality of a transmission setup can be gained by a comparison of $P_{receiver}$ and P_{source} :

$$T = \frac{P_{receiver}}{P_{source}} < 1. \qquad \text{(Eq. 19)}$$

Convergent radiation can only be generated by constructive interference of more than one (at least virtual) source (Huygens–Fresnel principle). Commonly an ideal point source of electromagnetic radiation is regarded describing the propagation of electromagnetic waves. In this picture, the emitted electromagnetic wave with a vacuum wavelength λ_0 propagates as spherical wave in the near field of the source. The curvature of the phase fronts is almost negligible and the wave can be treated as a plane wave [4] in the far field of a point source ($r >> \lambda$). A plane wave function for the electric field can be written in terms of the propagation distance z :

$$\vec{E}(z) = \mathrm{Re}\left(\vec{E}_0 e^{j(\omega t - k_0 z)}\right). \qquad \text{(Eq. 20)}$$

The propagation of a plane wave is undisturbed in vacuum but disturbed in matter. The perturbation caused by a material is described by a complex factor, the refractive index n :

$$n = n' - jn'' = -jn'' + (n' - 1) + 1,$$
$$\mathrm{Re}(n) = n',\ \mathrm{Im}(n) = -n''. \qquad \text{(Eq. 21)}$$

The medium causes a phase retardation which is described by the exponential $e^{-jk_0 z(n'-1)}$, which contains the real part of the refractive index. Further, the medium causes a decay of the amplitude $e^{-k_0 n'' z}$, which is described by the imaginary part of the refractive index. These perturbations are identified as individual exponential terms:

$$\vec{E}(z) = \mathrm{Re}\left(\vec{E}_0 e^{j(\omega t - nk_0 z)}\right) = \mathrm{Re}\left(\vec{E}_0 e^{-k_0 n'' z} e^{-jk_0 z(n'-1)} e^{j(\omega t - k_0 z)}\right). \qquad \text{(Eq. 22)}$$

The decay of the amplitude of an electromagnetic plane wave can be due to absorption and thus energy conversion. As well, it can be due to scattering which is caused by local variations of the refractive index. Remaining again in the picture of energy transfer, a medium causes loss which is described as exponential decay by Beer-Lambert's law [4] with an attenuation coefficient α:

$$I(z) = I_0 e^{-\alpha z}. \qquad \text{(Eq. 23)}$$

In terms of wave optics, the time averaged flux density of the electromagnetic energy is described by the Poynting vector $\bar{S}(z)$ (Eq. 16):

$$\bar{S}(z) = \frac{1}{2}\mathrm{Re}\left(\vec{E}_{ph} \times \vec{H}_{ph}^{\,*}\right)$$
$$\Leftrightarrow \bar{S}(z) = \frac{1}{2}\mathrm{Re}\left(\vec{E}_0 e^{-jn'k_o z} e^{-n''k_o z} \times \vec{H}_0^{*} e^{-n''k_o z} e^{jn'k_o z}\right) \qquad \text{(Eq. 24)}$$

In terms of plane waves, both fields are perpendicular and in phase. In order to calculate the norm of Eq. 24, the cross product may be replaced by a scalar product considering also the angle between the two vectors. The imaginary exponentials cancel. Further, the relation $\vec{H}_0 = \varepsilon_0 c_0 \vec{E}_0$ can be applied and thus Beer-Lamberts-law is rewritten:

$$\left|\bar{S}(z)\right| = \frac{1}{2}\varepsilon_0 c_0\ \mathrm{Re}\left(\left|\vec{E}_0 e^{-jn'k_o z} e^{-n''k_o z}\right| \cdot \left|\vec{E}_0^{*} e^{-n''k_o z} e^{jn'k_o z}\right| \sin(90°)\right)$$
$$= \frac{1}{2}\varepsilon_0 c_0 \left|\vec{E}_0 e^{-n''k_o z}\right|^2 = I(z) \qquad \text{(Eq. 25)}$$

Comparison of Eq. 23 and Eq. 24 results a proportionality of the attenuation coefficient α and the imaginary part of the refractive index $(-n'')$:

$$\frac{c_0\mu_0}{2}\vec{E}_0^{\,2}e^{-\alpha\Delta z} = \frac{c_0\mu_0}{2}\left(\vec{E}_0 e^{-k_0 n''\Delta z}\right)^2$$
$$\Leftrightarrow e^{-\alpha\Delta z} = e^{-2k_0 n''\Delta z} \qquad \text{(Eq. 26)}$$
$$\Leftrightarrow \alpha = 2k_0 n'' = \frac{4\pi}{\lambda_0} n''.$$

Summarizing, the loss of energy during the transfer through a medium is properly described by these equations. In the following, the measurement of the loss occurring in waveguides by using a cut-back technique is described and a method of calculating the power loss is presented.

2.1.1.1 Measuring the loss of waveguides by cutting back

Interestingly, Eq. 19 is easy to understand intuitively but cannot be transferred to measurement setups without discussion. Waveguides guide energy on predefined pathways and can reduce the loss. However, a waveguide typically accepts only the radiation within a critical angle of beam spread θ_{acc}. Additionally, reflections at the input or output interfaces of a waveguide may also reduce the transmission. These perturbations can be expressed by a coefficient γ_1. If a waveguide with the length z is coupled to a source, only a part of the iradiated intensity I_s enters the waveguide. The intensity at the entrance of the waveguide $(I_{z=0})$ can be expressed as:

$$I_{z=0} = I_s \cdot \gamma_1. \qquad \text{(Eq. 27)}$$

The intensity is further attenuated as the wave travels along the waveguide. Commonly, this loss is approximated as exponential decay with base 10 and an attenuation coefficient a which is commonly given in a unit dB/z. Thus, a factor 0.1 is considered in the exponent (1 dB = 0.1 B). Single-mode optical cables which are used in telecommunications have usually attenuations as low as 0.5 dB/km. In contrast, the unit of the attenuation coefficient is usually given in dB/cm for shorter waveguides.

$$I_z = I_{z=0} 10^{-0.1 \cdot a \cdot z} \qquad \text{(Eq. 28)}$$

The quantum- and coupling-efficiencies of the detector can be expressed as coefficient γ_2. Summarizing, this yields the detected intensity.

$$I_d = \gamma_1 \cdot \gamma_2 \cdot 10^{-0.1 \cdot a \cdot z} \qquad \text{(Eq. 29)}$$

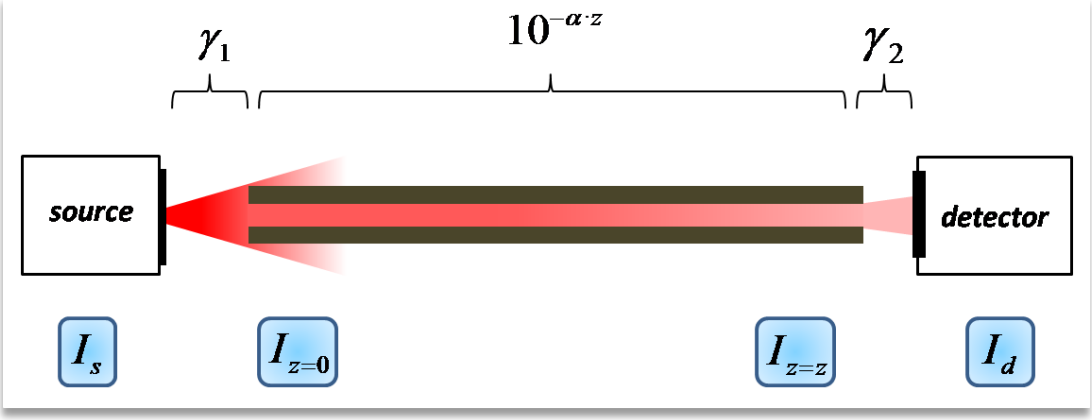

Fig. 2. Attenuation in a waveguide of a length z as exponential decay. The combined quantum- and coupling-efficiencies of the source and the detector are characterized by a parameter γ_1 and γ_2, respectively.

For experimental investigations on the waveguiding mechanism and thus the loss inside the waveguide, the coefficients γ_1 and γ_2 can be eliminated by a cut-back experiment. In a first step, electromagnetic radiation is coupled to a long piece of the waveguide and the transmitted intensity $I_{d,z}$ is detected. Subsequently, the length of the piece is reduced by cutting away a shorter piece with a length l. Now the optical output power $I_{d,z-l}$ is detected while the identical light source, coupling situation and detector are maintained. Accordingly, the attenuation can be calculated by a comparison of the two detected intensities:

$$\frac{I_{d,z}}{I_{d,z-l}} = \frac{10^{-0.1 \cdot a \cdot z}}{10^{-0.1 \cdot a \cdot (z-l)}} = 10^{-0.1 \cdot a \cdot l},$$
$$a = 10 \cdot \lg\left(\frac{I_{d,z}}{I_{d,z-l}}\right) \cdot l^{-1} \qquad \left[dB/cm\right] \qquad \text{(Eq. 30)}$$

Although waveguiding structures generally guide electromagnetic waves by quite complex mechanisms including the penetration of the guided modes into more than one material, a waveguide can be treated as an effective optical medium with an attenuation spectrum $a(\lambda_0)$. Highly interesting insights into the waveguiding mechanism can be obtained by spectroscopic analysis of a waveguide.

Even using the cut-back technique, still one problem remains. Waveguides commonly consist of layer structures. The guided radiation is confined to a core using a cladding structure, which consists of some kind of highly reflecting interfaces like a photonic crystal structure or a Bragg-mirror. If the cut-back

technique is applied, typically the whole profile of the waveguide is analyzed. However, undesired modes can be excited in the cladding. The experimental setup has to be properly adjusted to analyze selectively the attenuation of a particular mode in the core of the waveguide. In some cases, simple techniques already suffice to exclude undesired modes from the analysis. For example, when measuring the attenuation of optical fibers, commonly very long fibers (longer than 50 m) are used because only the desired modes have a very low attenuation [8]. Accordingly, the undesired modes have disappeared after a long propagation distance. In contrast, an aperture needs to be placed at the output face of the waveguide in order to measure the attenuation of rather short waveguides.

2.1.1.2 Calculating the loss of waveguides: The power loss method

Each mode exhibits an individual attenuation. Losses are caused by various mechanisms including absorption loss, scattering loss, loss caused by modal conversion, and in some cases confinement loss. The main source of loss is normally a leaky confinement in photonic crystal waveguides, where the confinement of the radiation to the waveguide core is highly dependent on λ_0. Theoretically, single-mode waveguides with total internal reflection as guiding mechanisms are lossless if the material absorption is neglected. In contrast, even single-mode photonic crystal waveguides are thought to exhibit loss due to imperfect modal confinement because the thickness of the photonic crystal cladding is finite [8]. Nevertheless, the bend loss achieved in photonic bandgap fibers today is already lower than the bend losses in total internal reflecting waveguides [7]. The main source of loss of the photonic bandgap guiding fibers investigated in this work is scattering, because liquid crystals have an extremely high scattering cross section compared to isotropic liquids. The attenuation caused by scattering can be estimated by calculating perturbations.

The time average of the energy flux density is described by the Poynting vector (Eq. 16). The fields in a waveguide can be approximated for example by a two dimensional electromagnetic field simulation considering lossless materials with real refractive indices. This yields the power flow $N(z)$ in the whole waveguide profile $A_{waveguide} = \sum_k A_k$, whereas the waveguide consist of the individual sections k:

$$N(z) = \int_{A_{waveguide}} \bar{S}(z) \cdot dA = \int_{A_{waveguide}} \frac{1}{2} \mathrm{Re}\left(\vec{E}(z) \times \vec{H}^{*}(z)\right) \cdot dA. \qquad \text{(Eq. 31)}$$

The complex refractive index and the complex dielectric constant are correlated:

$$\varepsilon_r = n^2 \Rightarrow \varepsilon_r = n'^2 - 2jn'n'' - n''^2, \qquad \text{(Eq. 32a)}$$

$$\mathrm{Re}(\varepsilon_r) = n'^2 - n''^2 = \varepsilon_r', \qquad \text{(Eq. 32b)}$$

$$\mathrm{Im}(\varepsilon_r) = -2n'n'' = -\varepsilon_r''. \qquad \text{(Eq. 32c)}$$

The absorption loss of electromagnetic energy is due to conversion into heat. This dielectric loss is described by the imaginary part of the relative dielectric constant [4]. In a waveguide with multiple sections, various types of loss are possible. In this case, the loss can also be evaluated by an imaginary part of the relative dielectric constant $\varepsilon_{r,k}$ inside of the individual sections k of a waveguide. It is possible to approximate the power loss density $p_{V,k}$ by using the undisturbed electric fields $\vec{E}_k$:

$$p_{V,k} = \frac{1}{2} \omega \varepsilon_0 \varepsilon_{r,k}'' \left| \vec{E}_k \right|^2. \qquad \text{(Eq. 33)}$$

As perturbation of the ideal lossless case, the power loss per length $P'(z)$ is obtained by integrating Eq. 33:

$$P'(z) = \frac{1}{\Delta z} \sum_k \int_{V_k} p_{V,k} dV = \sum_k \int_{A_k} p_{V,k} dA. \qquad \text{(Eq. 34)}$$

The loss of the waveguide $a_{waveguide}$ is finally obtained by a comparison of the power loss per length and the undisturbed power flow:

$$a_{waveguide} = \frac{P'(z)}{N(z)}. \qquad \text{(Eq. 35)}$$

2.1.2 Waveguiding mechanisms

Electromagnetic radiation is confined in the core and guided along the core of a waveguide (Fig. 3). The core region of the waveguide is clad by a second medium in order to create a high reflectivity at the interface. There are several methods to generate high reflectivities by using dielectric materials [4,5,8]. Once radiation with a vaccum wavelength λ_0 is confined in the core of a waveguide with the refractive index n_{core}, the wave vector $\vec{k}_{core}$ inside of the core is defined:

$$\left|\vec{k}_{core}\right| = n_{core}\frac{2\pi}{\lambda_0}. \qquad \text{(Eq. 36)}$$

The wave vector $\vec{k}_{core}$ has a component β in propagation direction:

$$\beta = n_{eff}\frac{2\pi}{\lambda_0}. \qquad \text{(Eq. 37)}$$

Along with this propagation constant β, the effective refractive index n_{eff} is introduced. The wave is free to propagate inside the core if $\beta < \left|\vec{k}_{core}\right|$ [5]. Accordingly, a mode can be guided in the core if $n_{eff} < n_{core}$.

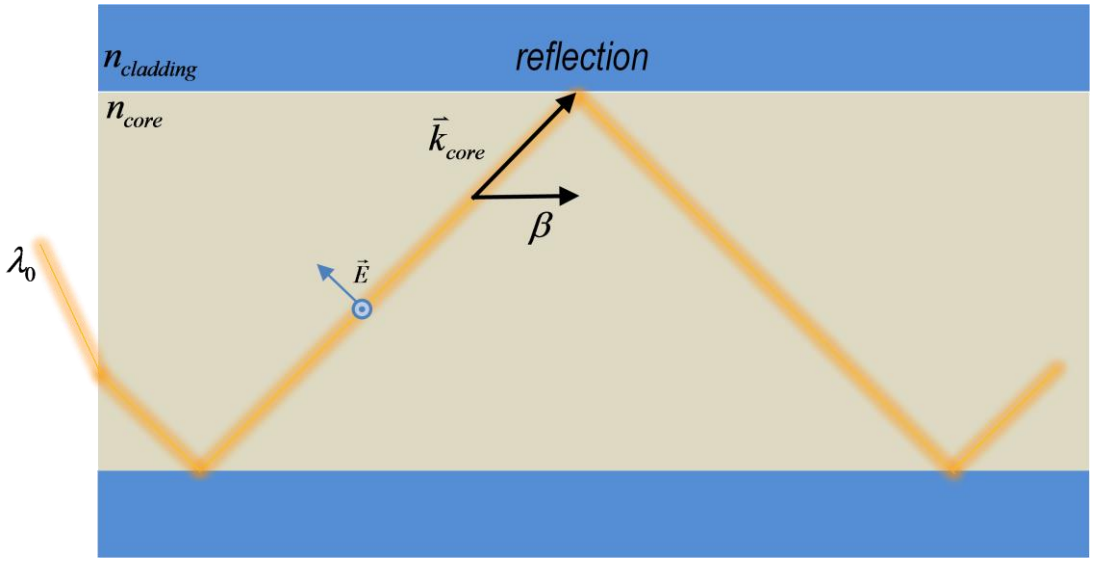

Fig. 3. Scheme of a waveguide were light is confined in a core region by a highly effective reflection mechanism.

2.1.2.1 Total internal reflecting waveguides

The behavior of electromagnetic waves at the interface of two different media is well understood[1] [4,38]. Snell's law of refraction correlates the angle of incidence θ_1 with the angle of refraction θ_2 (Fig. 4):

$$\sin\theta_1 = \frac{n_2}{n_1}\sin\theta_2. \qquad \text{(Eq. 38)}$$

[1] Although, new insights on metamaterials with surprising refractive properties were gained even in the last years [38].

Snell's law follows directly from the condition of continuity of the tangential component of the electric field vector [4]. The wave vectors k_i correspond to the incident wave, k_r to the reflected wave, and k_t to the transmitted wave (Fig. 4).

For lossless media, a 100 % reflection which is independent of the state of polarization (total internal reflection) is theoretically possible for a wave which travels in a high index medium (n_1) and is reflected at the interface with a medium of lower refractive index n_2. Total internal reflection occurs if the angle of incidence exceeds the critical angle θ_c (Fig. 4, middle, $\theta_2 = 90°$). Total internal reflection can be used as guiding mechanism at the interface of the core and the cladding of a waveguiding structure. The core, where the light is guided, has in this case a higher refractive index than the cladding. Modes with $\beta < |\vec{k}_{core}|$ are guided. The relation $\beta = |\vec{k}_{core}| \Rightarrow n_{eff} = n_{core}$ corresponds to the case if the critical angle is reached [5].

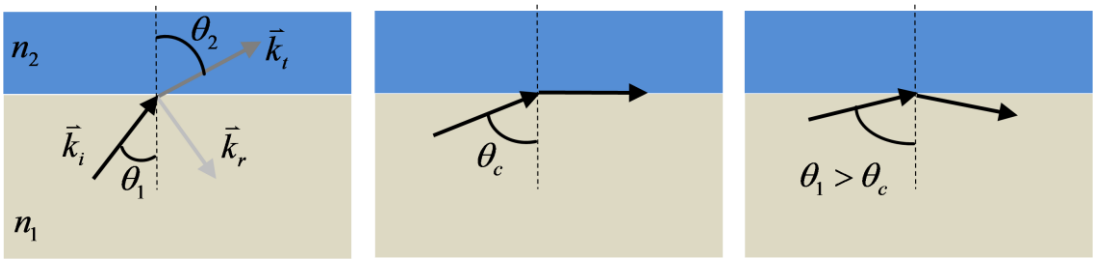

Fig. 4. Refraction at an interface of two media with refractive indices $n_1 > n_2$.

Conventional optical fibers with cylindrical cores are waveguides perfectly suited for extremely long propagation lengths. Moreover, this type of waveguide has a special relevance for the current work because the high index inclusions of the filled photonic crystal fibers have also cylindrical symmetry. The waveguiding properties of isotropic high index inclusions are well-known to have great influence on the guiding properties of photonic crystal fibers with such inclusions as cladding entities [10,11,12].

An optical fiber consists of a cylindrical core with low imaginary part of the refractive index. The core is embedded in a cladding which has lower refractive index than the core. The cladding has also a low imaginary part of the refractive index. The cladding is surrounded by a coating. The coating (commonly a polymer

coating) protects the cladding from mechanical damage and can be very useful to dampen undesirable cladding modes.

$$\nabla^2 \vec{E} + \vec{k}_0 n^2(r)\vec{E} = 0. \qquad \text{(Eq. 39)}$$

In the literature [2] the wave equation (Eq. 39) for the electric field is solved in cylindrical coordinates.

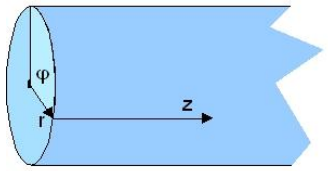

Fig. 5. Cylindrical coordinates *r*, φ and *z*.

The analysis presented in [2] assumes electric field solutions of the form:

$$\vec{E} = \vec{E}(r,\varphi)e^{-j\beta z}. \qquad \text{(Eq. 40)}$$

These solutions propagate in *z*-direction. For a step-index fiber with a core radius R_{core} and a cladding radius $R_{cladding}$ the refractive index depends on the radial coordinate r [$n(r < R_{core}) = n_{core}$, $n(R_{core} < r < R_{cladding}) = n_{cladding}$]. Thus, the two different refractive indices have to be considered in two wave equations (one in the core and one in the cladding.) and the continuity (natural) boundary condition has to be fulfilled. Wave equations for a general *z*-propagating sinusoidal field are formulated in cylindrical coordinates with a transverse Laplacian $\nabla_t^2(r,\varphi)$ and $\beta_t^{\,2} = (k_0^2 n^2 - \beta^2)$ [2]:

$$\nabla_t^2 E_z + \beta_t^{\,2} E_z = 0 \qquad \text{(Eq. 41)}$$

The separation of the dependences on r , φ , and z leads to a series of solutions:

$$E_{z,i} = R_i(r)\,\Phi_i(\phi)\exp(j\beta_i z). \qquad \text{(Eq. 42)}$$

Each individual solution $E_{z,i}$ can be inserted into Eq. 41 in order to obtain:

$$\frac{r^2}{R}\frac{dR}{dr^2} + \frac{r}{R}\frac{dR}{r} + r^2\beta_t^2 = -\frac{1}{\Phi}\frac{d^2\Phi}{d\phi^2}. \qquad \text{(Eq. 43)}$$

Each side of Eq. 43 depends on only one variable r or φ. It follows that each side of Eq. 43 equals a constant, since r and φ vary independently. The differential equation dependent on the azimuth is defined by using a constant q^2:

$$\frac{d^2\Phi}{d\phi^2} + q^2\Phi = 0. \qquad \text{(Eq. 44)}$$

The solutions of Eq. 44 are of the form:

$$\Phi(\varphi) = e^{iq\varphi} \quad q \in \boldsymbol{N}.. \qquad \text{(Eq. 45)}$$

With the same constant q^2, the radial part of Eq. 43 can be described:

$$\frac{\partial^2 R(r)}{\partial r^2} + \frac{1}{r}\frac{\partial R(r)}{\partial r} + \left(\beta_t^{\,2} - \frac{q^2}{r^2}\right)R = 0. \qquad \text{(Eq. 46)}$$

Eq. 46 is a form of Bessel's equation. The solutions are provided by linear combinations of the Bessel functions of the first and the second kind. These solutions of Eq. 46 describe the fields in the core and the cladding region of the step-index fibers and thus the modes. A detailed discussion of the modes of optical fibers is given in [2].

The modes are classified by the mode order q and the radial mode number m. The transverse electric family of modes have $E_z = 0$. The only nonzero field components are H_r, H_z, and E_ϕ. These modes are designated TE_{0m} modes because they cannot have another mode order than 0. Likewise, the transverse magnetic modes cannot have another mode order than $q = 0$ (TM_{0m}). The nonzero components in this case will be E_r, E_z, and H_ϕ. The mode order is $q \neq 0$ for the hybrid modes which have z-components of $\vec{E}$ and $\vec{H}$. These modes are either designated EH_{qm} or HE_{qm}.

Some of the lower order modes degenerate to linear polarized modes in the weakly guiding approximation $\frac{n_{core} - n_{cladding}}{n_{cladding}} << 1$ [3]. These modes are designated LP_{lm} modes. The fundamental mode of an optical fiber is the HE_{11} mode. The LP-designation for this mode is LP_{01}. The fundamental mode is twofold degenerate. The TE_{01}, TE_{01}, and TE_{0m} modes together form the LP_{11} set which is fourfold degenerate. The electric field amplitude profiles of some low order LP-modes are shown in Fig. 6 [39].

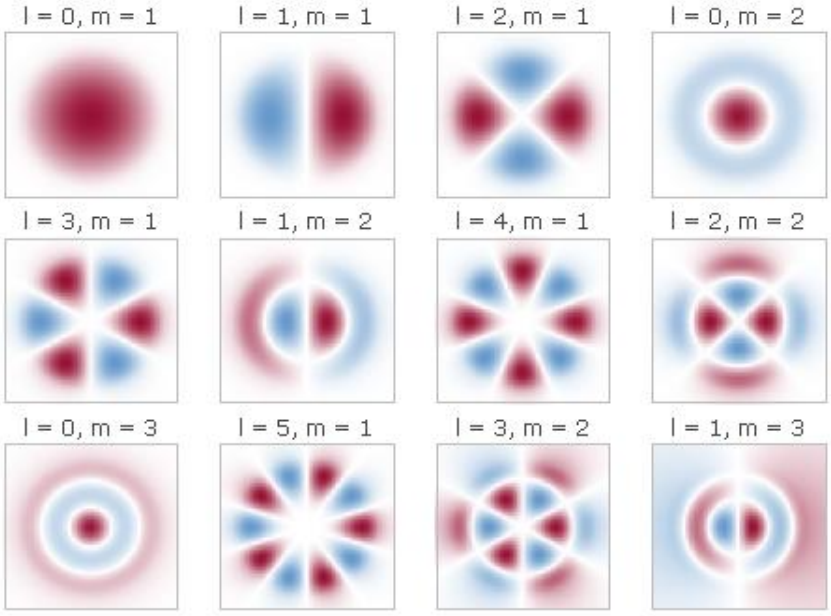

Fig. 6. Electric field amplitude profiles of the LP_{lm}-modes.The two colors indicate different signs of electric field values. Figure copied from [39].

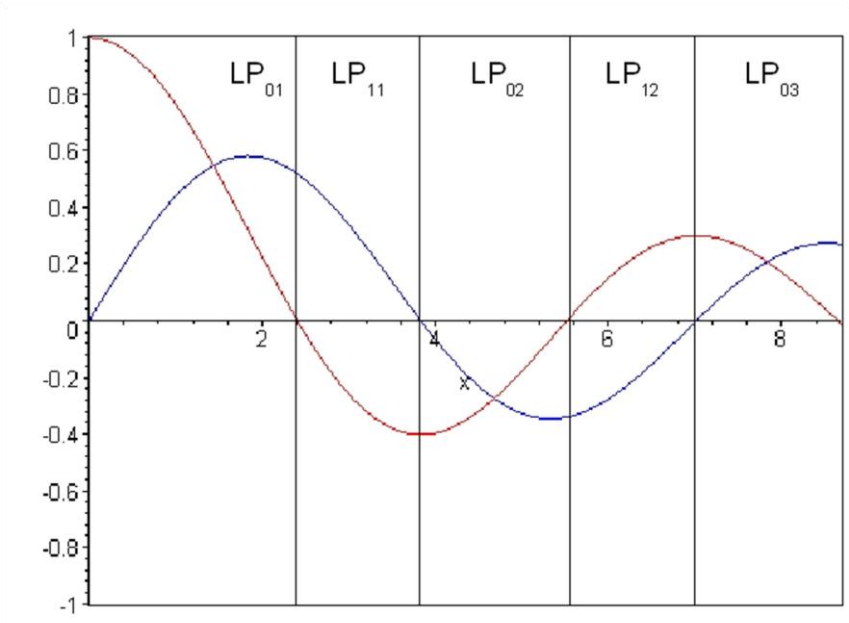

Fig. 7. Plot of the Bessel functions J_0 (red) and J_1 with correlated mode labels in the weakly guiding approximation (LP_{lm}-modes) [3].

The number of modes supported by an optical fiber depends on the core radius r_{core} and the refractive index contrast of the core and the cladding. The modal cut-off is described with the fiber parameter V :

$$V = \beta_t^2 \cdot r_{core} \approx \frac{2\pi r_{core}}{\lambda_0} \cdot \sqrt{n_{core}^2 - n_{cladding}^2}. \qquad \text{(Eq. 47)}$$

V increases with the core radius r_{core} and decreases with the wavelength λ_0. The fundamental mode LP_{01} has no cut-off wavelength, it is free to propagate for any value of V. Additional modes are allowed to propagate in the fiber if the Bessel functions $J_i(\beta_t r)$ exceed their first null at 2.405 (Fig. 7). The number of modes increases with the zeros of the Bessel functions. The corresponding modes are indicated in Fig. 7. With increasing wavelength, the number of modes decreases. A fiber with a constant core radius supports at lower wavelength a larger number of modes. Very interestingly, the quality of the power confinement for all modes decreases with increasing wavelength. Some modes have a very low confinement at the cut-off wavelength where the critical angle is reached $n_{eff}(\lambda_0) = n_{core}$. This phenomenon leads to the occurrence of resonances which will be discussed in the next chapter in more detail.

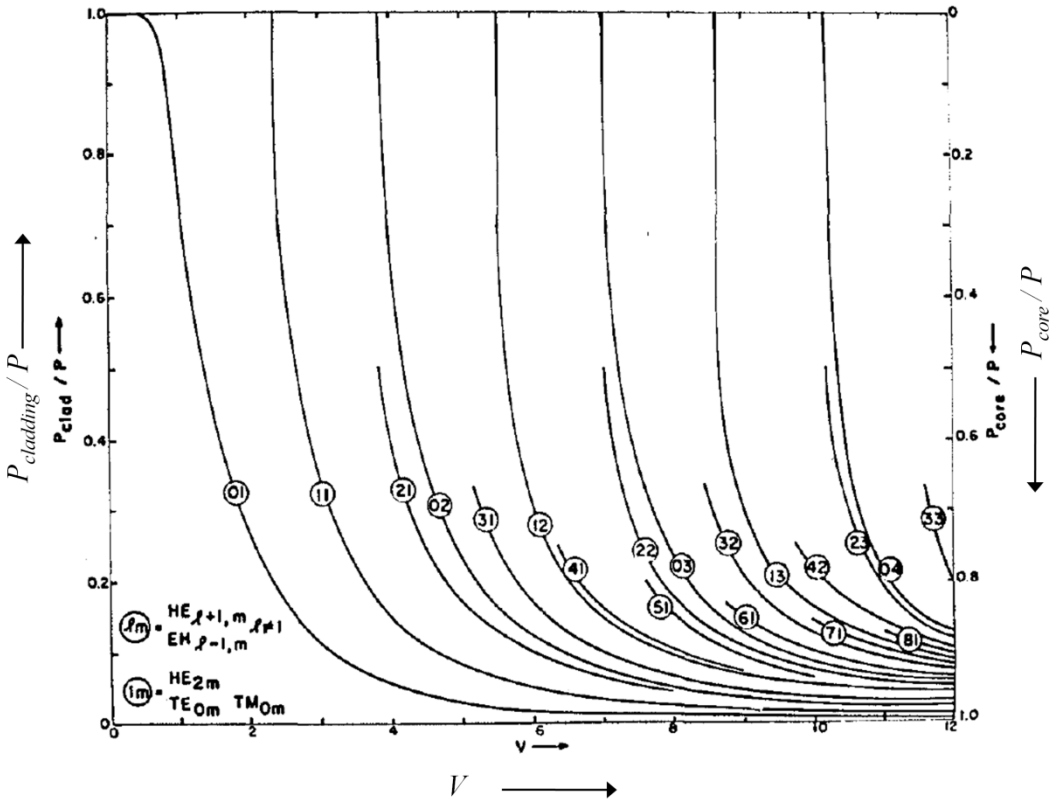

Fig. 8. Quality of the modal power confinement in the core of an optical fiber or a high index cylindrical inclusion. Right scale: $P_{core}/P = 1$ corresponds to a high confinement in the core, $P_{core}/P << 1$ corresponds to a high leakage from the core. Figure copied from [3], labels repeated.

Another interesting property is the chromatic dispersion of the LP_{01} mode. The chromatic dispersion D compares the temporal spreading (in ps) of a pulse to the bandwidth of the pulse (in nm) that occurs during the propagation through the fiber (in km). The group velocity of pulses and the chromatic dispersion are defined as follows:

$$v_g = \left(\frac{\partial \omega}{\partial k}\right) = \frac{c}{n_{eff}\,\omega \dfrac{dn_{eff}}{d\omega}}, \qquad \text{(Eq. 48)}$$

$$D = \frac{\omega^2}{2\pi c v_g}\frac{dv_g}{d\omega}. \qquad \text{(Eq. 49)}$$

The chromatic dispersion of a dielectric waveguide can be understood as a sum of different contributions (Fig. 9) [2].

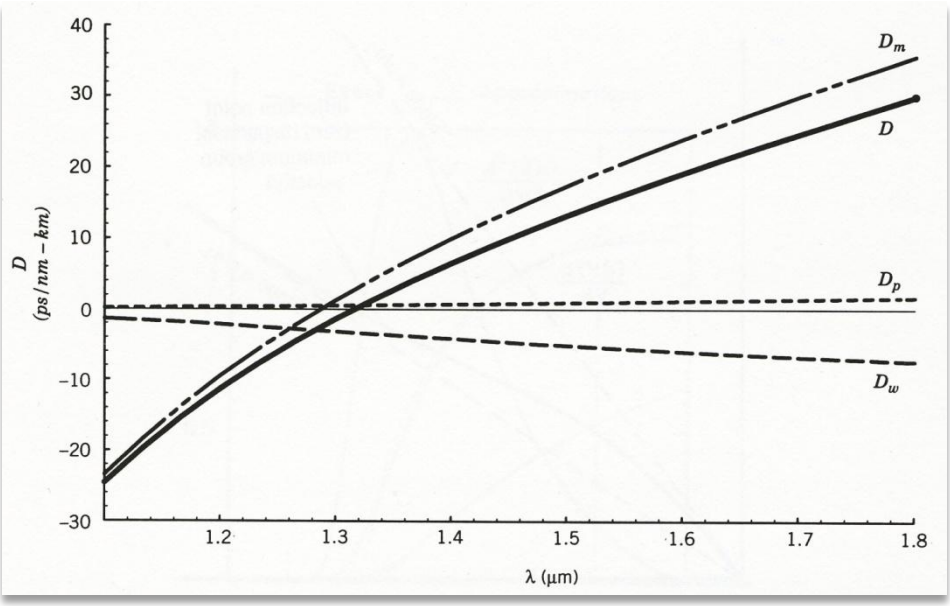

Fig. 9. Chromatic dispersion D of a step-index fiber. The chromatic dispersion is a sum of different contribution: composite material dispersion D_m, waveguide dispersion D_w, profile dispersion D_p. Figure copied from [2].

In conventional optical fibers, losses even lower than 0.5 dB/km can be achieved in the infrared spectral region. Such low losses are possible in conventional single-mode optical fibers for wavelength where only the LP_{01} modes are supported.

Waveguides which have a rectangular profile can be used for shorter propagation lengths. These waveguides are widely applied in the field of integrated optics. In the 1970s, the waveguiding properties of liquid crystal waveguides with

rectangular shape were investigated [14,40]. In these structures, light is guided by total internal reflection in a liquid crystal-filled rectangular core, which is surrounded by an isotropic cladding with lower refractive index. Unfortunately, such liquid crystal waveguides exhibit very high losses (25 dB/cm) due to the high scattering cross section of liquid crystals.

2.2 Photonic crystal fibers

Photonic crystal fibers have been in practical existence as low-loss waveguides since the last 14 years [5,6]. These fibers with a periodic transverse microstructure open new possibilities to design waveguides with outstanding properties. Photonic crystal fibers exhibit an extraordinary flexibility of fiber design, thereby enabling to tailor the dispersion relation and to make use of linear and nonlinear optical properties, very efficiently. These opportunities have lead to various developments, for example the fabrication of endlessly single-mode fibers or the generation of supercontinuum spectra by pulsed light.

Hollow core photonic band gap fibers guiding light in gases have gained great interest as (air-filled) low-loss waveguides, as extremely elongated cuvettes for the analysis of gases, or even in fluidic experiments [41]. A complete photonic bandgap is the frequency region where the density of states inside a periodic composite material (photonic crystal) is *0*, independent of the polarization. A photonic crystal can have an extraordinary high reflectivity for radiation within the photonic bandgap. It is possible to compare some composite materials to simple planar Bragg-stacks. However, conventional Bragg stacks have no complete photonic bandgap for all states of polarization in the case of other than perpendicular incidence. In contrast, a one dimensional microstructure with complete bandgap is referred to as omnidirectional reflector. Roughly, for the case of perpendicular incidence, the lattice constant of a photonic crystal is comparable to an optical wavelength inside a bandgap. However, a lattice of cylindrical high index inclusions can have a complete photonic bandgap even for very flat angles of incidence (grazing incidence). A detailed description of the effects in photonic crystals is given in [8].

A propagation diagram of a simple photonic crystal cladding is shown in Fig. 10. The periodic transverse microstructure consists of a continuous trigonal lattice of cylindrical air inclusions in fused silica as background material and is completely characterized by the lattice pitch p and the air filling fraction. Such a structure exhibits a well-defined dispersion and band structure. These properties determine the behavior of the guided modes that form at defects such as the core of a photonic crystal fiber. The propagation diagram scales with the pitch. Light propagation is impossible in the gray and black shaded regions of the propagation diagram. The maximum possible value of $\beta \cdot p$ is given by $n_{glass} \cdot k_0 \cdot p$ in the glass and $n_{air} \cdot k_0 \cdot p \approx k_0 \cdot p$ in air. For $\beta > k_0 \cdot n_{glass}$ and $\beta > k_0 \cdot n_{air}$ the light is evanescent in the respective materials. Light can propagate in a glass core if $\beta < k_0 \cdot n_{glass}$. For $\beta = k_0 \cdot n_{glass}$, the critical angle of total internal reflection is reached for light incident from the glass to the glass/air interface. Full two-dimensional photonic bandgaps exist in the black regions of the propagation diagram (where no propagation is possible). Light can be trapped within a hollow core if such a region extents into the region $\beta < k_0$ where light is free to propagate in vacuum. The diagram shows the propagation properties of the cladding structure. Light which is coupled to a defect cannot propagate in the cladding and is thus trapped. The relevant operating region of the current example is to the left of the vacuum line $(\beta = k_0)$. A rather large core and a small pitch (point B) are required for air guiding in this silica/air structure in order to actually confine a mode inside a hollow core [5].

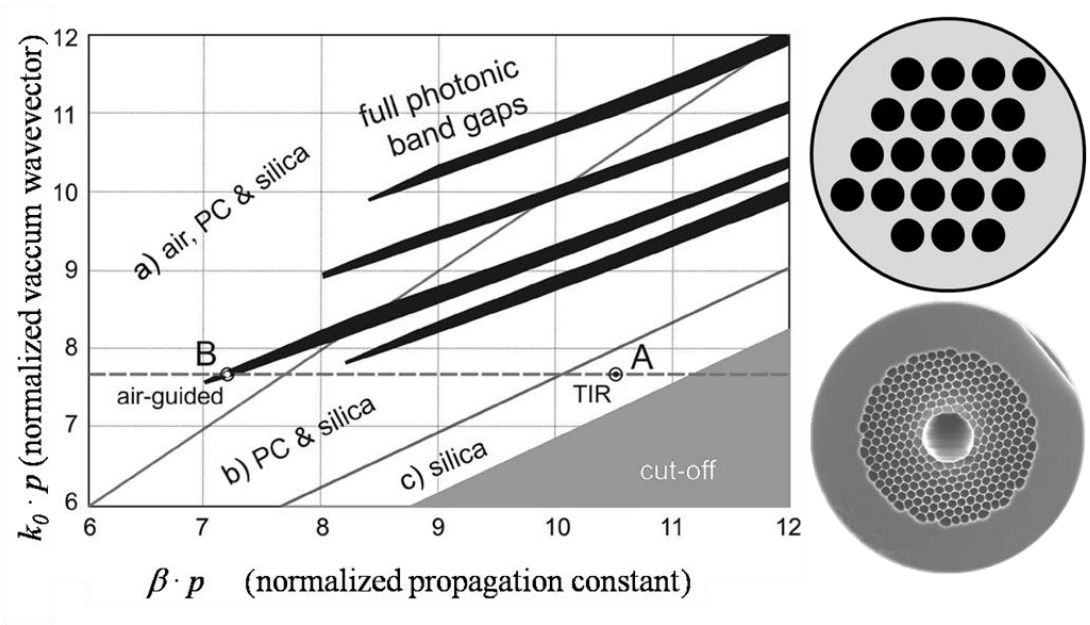

Fig. 10. Out of plane propagation diagram for a 2D photonic crystal which consists of a trigonal lattice of cylindrical air inclusions in a background of silica glass (structure shown top right, with a lattice pitch *p*). The air filling fraction of the lattice is 45%. Light is allowed to propagate a) in all regions, b) in the photonic-crystal cladding and in the silica region, c) only in silica glass. No propagation is possible in the gray and black shaded regions. The black shaded regions indicate the positions of full 2-D photonic band gaps. The profile (SEM-image) of a hollow core fiber [5] with 20.4 µm core diameter and an attenuation as low as 1 dB/km at 1550 nm wavelength is shown as well. Figure copied from [5].

A photonic bandgap fiber with a core diameter of 20 µm where light can be guided in an air core is as well shown in Fig. 10 (lower right). Photonic crystal fibers where light is guided in a glass core are used in the filling experiments described in this work. In the unfilled state, these fibers guide light because the refractive index of the core is larger than the average refractive index of the cladding (modified total internal reflection [5,6]). Even in the visible wavelength range, light is guided selectively by the fundamental mode due to the holey cladding, thereby allowing larger core diameters (~ by a factor 2) than in standard single-mode optical fibers. The fibers show continuous transmission in the unfilled state (Fig. 11).

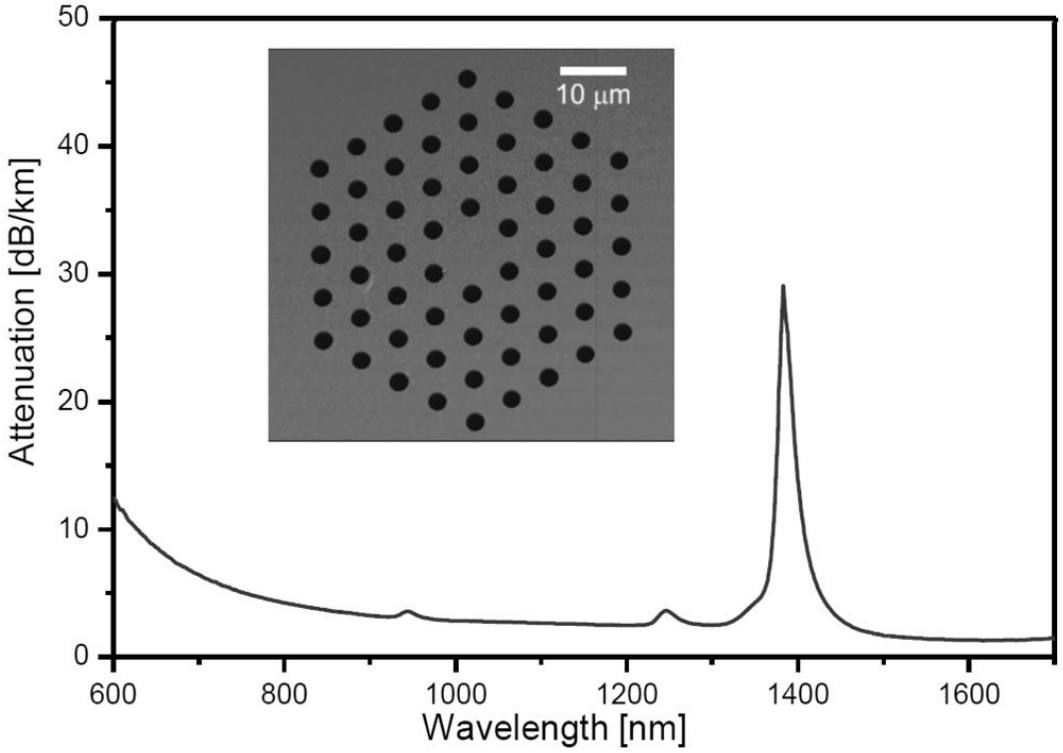

Fig. 11. Attenuation spectrum (courtesy of NKT-Photonics) and profile (SEM-image, scale bar = 10 μm) of the index guiding large mode area fiber LMA-10 (Figure copied from [42]).

2.2.1 All-solid photonic band gap fibers

Surprisingly, all-solid photonic band gap fibers have become candidates to achieve low attenuations by applying the photonic band gap effect and maintaining an all-solid structure [5,8,9,43]. These fibers were discussed as simple bandgap fibers [10] where the waveguiding properties are determined by resonances of the entities in the cladding [11].

Commonly, in this type of fiber, cylindrical high index inclusions in a background material with lower refractive index are arranged in a trigonal array forming a 2-dimensional microstructure. In the center of this microstructure, one inclusion is missing and guided modes are confined in this central low index core. Principally, there are two ways to realize all-solid microstructured fibers. Fibers longer than several m are drawn from a macroscopic preform already consisting of the intended materials in an adequate geometry. But also, shorter pieces are sufficing for optical modulators or filters: Schmidt et al. have shown recently [13], that such

short pieces of all-solid photonic band gap fibers can be fabricated by pressing molten high index tellurite glass into a microstructured silica glass fiber with a silica glass core surrounded by an array of air inclusions.

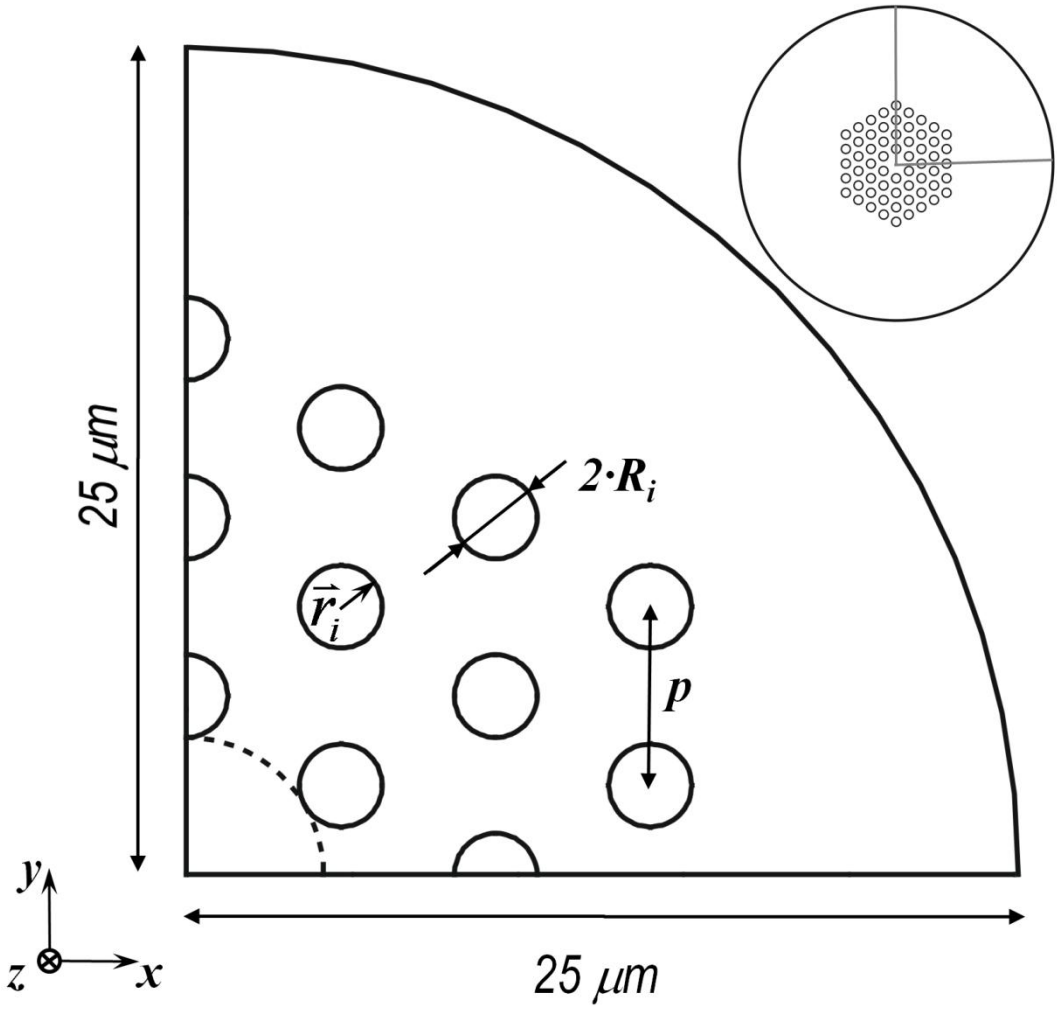

Fig. 12. Structure of a photonic crystal fiber with three rings of cylindrical inclusions. Only a quarter of the structure is shown. The size of the core is indicated by a dashed line. Additionally, a fiber with 4 rings of inclusions is shown as inset. The two gray lines shown in the inset highlight two selected mirror planes of such trigonal arrangements of cylindrical inclusions (the mirror plane parallel to the *x*- and the mirror plane parallel to the *y*-axis).

The guiding properties of such all-solid photonic bandgap fibers with isotropic high index inclusions ($n_{inclusion} > n_{glass}$) can be understood by the analysis of the resonant coupling of the inclusions. Birks et al. [10] reported numerical approximations where the sizes of the low-index regions separating the inclusions are explicitly considered and provided a close representation of the exact band plot. Litchinitser et al. [11,12] reported an analytical approach due to their numerical observation that in such fibers, the scattering properties of the single high index

inclusions determine the spectral transmission characteristics rather than their position and number (antiresonant reflecting optical waveguides (ARROW) [71]). In this model, the core of the photonic crystal fiber is surrounded by inclusions which are treated as individual total internal reflecting waveguides.

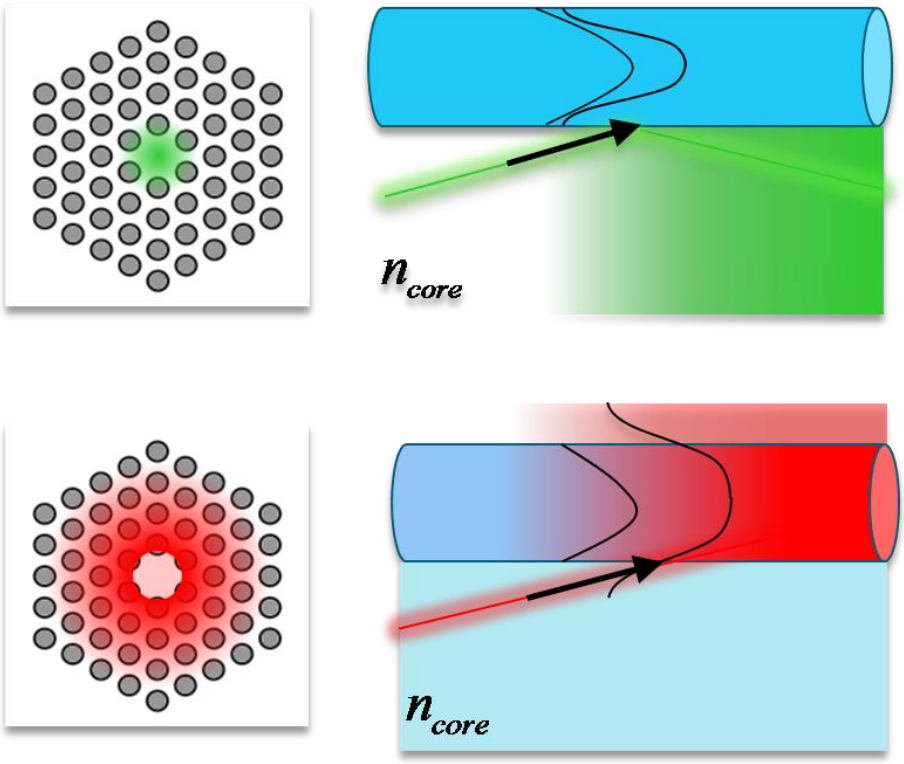

Fig. 13. Visualization of the guiding mechanism in a photonic crystal fiber with high index inclusions in a background material with lower index. Green light is confined in the core region, due to anti-resonance of the inclusions. The inclusions have well confined inclusion modes and a high reflectivity for light impinging from the outside. Red light cannot be confined in the core because of a resonance of the inclusions. There is an inclusion mode which is not very well confined for red light. Energetic crosstalk is possible and the inclusions have a high transmittivity for red light. Thus, red light escapes from the core.

Waveguiding in the core of the photonic crystal fiber is possible due to antiresonant reflection of the individual high-index inclusions. However, in spectral regions where the inclusions show resonances, no waveguiding in the core is possible. The resonances of cylindrical high index inclusions are well-known [2,3,12]. A cylindrical high index inclusion with the refractive index $n_{inclusion}$ embedded in a background material with lower refractive index (for example fused silica, n_{silica}) is a waveguide which can support a reasonable number of modes dependent on the refractive index contrast and the inclusion diameter. Due to the

waveguide dispersion, the effective refractive indices $n_{eff}(\lambda_0)$ of these inclusion modes decrease with increasing wavelength. Resonances of the TE_{0m}, TM_{0m}, HE_{1m}, and HE_{2m} inclusion modes degrade the confinement in the core of the photonic crystal fiber. The inclusion resonances occur if $n_{e_{ff}}(\lambda_0) = n_{silica}(\lambda_0)$ (Fig. 13). The core mode of the photonic crystal fiber expands into the inclusions near such resonances and distinct loss maxima of the core are created because the integral over the power density in the core region of the photonic crystal fiber gets smaller and smaller in propagation direction. The spectral position $\lambda_{\min}$ of the resonances and thus the transmission minima of the core of the photonic crystal fiber can be calculated by analytical approximations for the inclusion modes. For cylindrical inclusions which consist of materials with known refractive indices, the transmission minima generated by resonances of the TE_{0m}, TM_{0m}, HE_{1m} inclusion modes depend on the band number m and the inclusion radius R_i [12]:

$$\lambda_{\min} = \frac{4R_i\sqrt{n_{inclusion}^2 - n_{silica}^2}}{m + 1/2},\ m \in \boldsymbol{N}. \qquad \text{(Eq. 50)}$$

In the current work, bandgap guiding fibers are created by filling fused silica fibers with cylindrical air inclusions and a solid core with nematic liquid crystals with higher refractive index. The attenuation spectra of such fibers with liquid crystal birefringent inclusions are observed experimentally in the visible spectral region. Additionally, electromagnetic field simulations are presented where the complete fiber structure is considered rather than single inclusions. The transmission properties of the filled fibers are due to the resonances of the inclusions. The tendency that resonances occur if the effective refractive index of the inclusion modes equals the refractive index of the background material is described by the ARROW-model. The resonant coupling is nevertheless influenced by the pitch of the inclusions. This is well understood for isotropic inclusions [10]. In contrast to an analysis of the single inclusions, simulations of the complete structure show additionally properties of the guided core modes, like for example the chromatic dispersion.

2.3 Nematic liquid crystals

In crystals, the centers of mass of the crystal building blocks are located in a three dimensional periodic lattice. The precise position of each crystal building block is predetermined in the unit cell and the entire lattice is constructed by translation of the unit cell in all spatial directions. For this reasons, the centers of mass have a long range order. The symmetry of the crystal corresponds to the symmetry of the unit cell. Furthermore, in a molecular crystal consisting of anisometric molecules there is long range order of the molecular orientation. Most of the solids lose any kind of long range order and show a phase transition to an isotropic liquid during the melting process. The building blocks (molecules, atoms or ions) have in principal three translatational degrees of freedom in isotropic liquids.

In the thermotropic or lyotrpic liquid crystalline (or mesomorphic) phases, orientational order is present while the positional order is reduced or may even be absent. As expected by the appearance of long range orientational order in crystals, liquid crystalline phases require anisometric constituent entities.

Pure substances or mixtures of substances which consist of rod like (calamitic) molecules can show numerous thermotropic mesophases. Orientational order appears and the long molecular axes of these molecules are on average parallel to each other in the nematic phase. This average molecular orientation of a liquid crystal varies usually spatially and is thus described with the director field $\vec{\nu}(\Omega)$ (where Ω are the coordinates of an appropriate coordinate system). The director is a pseudo vector which is parallel to the average orientation of the molecular axes. The director field is comparable to a vector field of unity vectors $\left(|\vec{\nu}| = 1\right)$. In contrast to a vector field, the pointing direction of the local director is degenerate with the opposite direction $\vec{\nu} = -\vec{\nu}$ [16,44]. The quality of the parallel alignment of the calamitic molecules can be described by an order parameter S. This order parameter is a scalar in the nematic phase (with β as angle between the local director and the long axis of the molecules):

$$S = \frac{3}{2}\left\langle \cos^2(\beta) - 1 \right\rangle. \qquad \text{(Eq. 51)}$$

S can theoretically vary between $S = 1$, which corresponds to perfect order and $S = 0$, which corresponds to statistic disorder. The scalar order parameter of the nematic phase depends on the temperature T. The temperature dependence is

approximated in the theory of Maier and Saupe (where T_{NI} is the isotropic to the nematic phase transition temperature) [45]:

$$S \approx \left(1 - 0.98\frac{T}{T_{NI}}\right)^{0.22}. \qquad \text{(Eq. 52)}$$

Numerous physical properties are anisotropic in liquid crystals. Two anisotropic optical properties of the nematic phase, namely the birefringence and the anisotropy of the scattering cross section, are especially important for liquid crystal-filled photonic crystal structures. Furthermore, the large dielectric anisotropy in the kHz frequency region can be exploited to induce reorientations of the director due to external addressing fields for selected nematic liquid crystals.

2.3.1 Elastic properties

A liquid crystal is an elastic medium. The director field is in a stable state if the free distortion energy is minimal. Franck [46] described the free energy density F of a liquid crystal by using four elastic coefficients K_{ki} (Franck elastic coefficients):

$$\begin{aligned} F = \frac{1}{2}[&K_{11}(\nabla \cdot \vec{\nu})^2 + K_{22}(\vec{\nu} \cdot \nabla \times \vec{\nu})^2 + K_{33}(\vec{\nu} \times \nabla \times \vec{\nu})^2 \\ &- K_{24}\nabla \cdot (\vec{\nu}(\nabla \cdot \vec{\nu}) + \vec{\nu} \times \nabla \times \vec{\nu})]. \end{aligned} \qquad \text{(Eq. 53)}$$

Each term of Eq. 53 represents one type of distortion, respectively. The distortion free energy density of nematic liquid crystals in the bulk is commonly described by the first three terms of Eq. 53. The first term of Eq. 53 represents pure splay, the second term pure twist, and the third term pure bend deformation of the director field. The fourth term (saddle-splay) describes the surface interaction and can be ignored if the energies in the bulk of the liquid crystal are greater than those due to the surface. However, the fourth term is especially important for liquid crystals confined in small cavities [50]. Generally, a one constant approximation can be used to describe distortions of the director field qualitatively because the Frank elastic constants are of the same order of magnitude. In the one constant approximation, it is assumed that $K_{24} = 0$ and $K_{11} = K_{22} = K_{33} = K$:

$$F = \frac{1}{2}K\left((\nabla \cdot \vec{\nu})^2 + (\nabla \times \vec{\nu})^2\right). \qquad \text{(Eq. 54)}$$

2.3.2 Losses in liquid crystals

Liquid crystals show extraordinary high light scattering losses in the visible spectral region compared to isotropic liquids. A high damping occurs even if the liquid crystal molecules show no absorption bands. The major reason for this high damping is scattering.

Liquid crystals which are applicable at room temperature consist of mixtures of several species. In the visible spectral region, molecules contained in typical nematic mixtures like for instance 4-cyano-4'-pentylbiphenyl (5CB) show no absorption bands. The absorption characteristics of 5CB were reported in the literature [47]. Absorption measurements with a standard dual-beam UV/vis-spectrometer ranging from 185 to 3200 nm were reported. Interestingly, the cuvett in the reported experiments had a thickness d of only $d \approx 0.3$ µm. Experimental results for 5CB from the literature are shown in Fig. 14 and Fig. 15. The absorption losses of this type of compound in the nematic phase are in the visible spectral region three orders of magnitude smaller than the scattering losses.

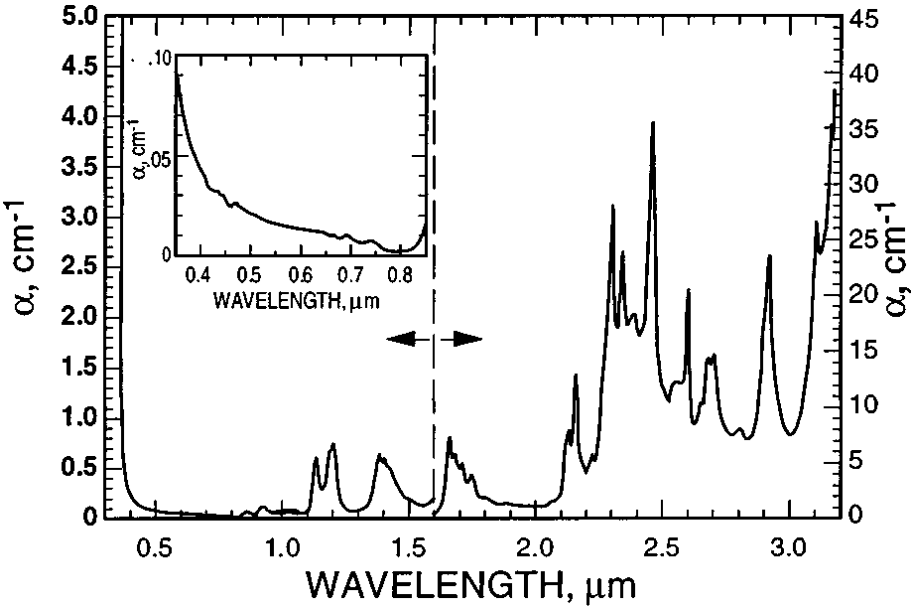

Fig. 14. Absorption coefficient of 5CB at T = 50 °C (isotropic phase). Figure copied from [47].

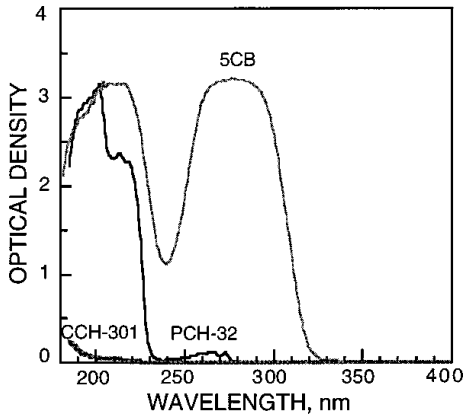

Fig. 15. Optical density of CCH-301, PCH-32 and 5CB [47]. Cell gap d = 0.3 μm. CCH-301 and PCH-32 T = 22 °C, 5CB at T = 50 °C. To convert optical density to absorption coefficient α use: *optical density* = $\alpha \cdot d$ / *2.3*. Figure copied from [47].

In any medium, small local changes of the density or the temperature can cause local variations of the dielectric tensor ε_r. De Gennes [48] has shown that in nematic liquid crystals, fluctuations of ε_r are dominantly caused by fluctuations of the orientation of the director $\vec{v}$. The extent of fluctuations depends on the elastic constants K_{ii} $(i = 1, 2, 3)$. Considering the free elastic energy of bulk material in a thermal equilibrium, de Gennes theoretically derived $d\sigma_{sc,lc}/d\Omega$, the differential scattering cross section of a nematic liquid crystal per solid angle. Accordingly, de Gennes compared the scattering cross section of a typical nematic liquid crystal $\sigma_{sc,lc}$ to the scattering cross section of an isotropic liquid $\sigma_{sc,iso}$. He found $\sigma_{sc,lc} \approx 10^6 \cdot \sigma_{sc,iso}$ as an order of magnitude estimate [16].

The total scattering cross section or turbidity of oriented nematic liquid crystals was calculated by Langevin and Bouchiat [49]. Using their model, they could successfully extract the three elastic constants K_{ii} (i = 1, 2, 3) of a nematic liquid crystal from experimental light scattering data in three selected geometries. In their work, experimental and theoretical investigations of the anisotropy of the scattering loss of the liquid crystal n-(4-methoxybenzylidene)-4-butylaniline (MBBA) were reported. The anisotropy of the scattering cross section (with unit m^2) leads to three scattering coefficients $\alpha_{sc,1}, \alpha_{sc,2}, \alpha_{sc,3}$ (damping coefficients with unit m^{-1}). Each scattering cross section can be measured by evaluating the transmission loss of a uniform director field. The reported experiments were conducted with linear polarized laser light (He/Ne-laser 633 nm) in three selected geometries. The

orientation of the polarization of the incident beam $\vec{i}$ relatively to the director $\vec{v}$ was varied in these experiments. If the director was oriented along the propagation direction of the laser light $\left(\vec{v} \parallel \vec{k}\right)$ and the incident light was polarized perpendicular to the director $\left(\vec{i} \perp \vec{v}\right)$ a scattering cross section $\sigma_{lc,1}$ was investigated. The director was aligned perpendicular to the propagation direction in the further two experiments $\left(\vec{v} \perp \vec{k}\right)$. The scattering cross section $\sigma_{lc,2}$ could be measured if the incident light was again perpendicular to the director $\left(\vec{i} \perp \vec{v}\right)$. The scattering cross section $\sigma_{lc,3}$ was found if the incident light was polarized parallel to the director $\left(\vec{i} \parallel \vec{v}\right)$. Langevin and Bouchiat investigated the transmission through relatively thick layers (1 to 2 mm) of the liquid crystal and realigned the director field by using a permanent magnet [49]. Selected results of the 1.3 mm thick sample are shown in Tab. 1. The values for the detected intensity $I_{detector}$ were reported in a figure and are shown in Tab. 1 in order to give a rough impression of the results. The third row shows the loss calculated by using these values and the initial intensity of the laser light (50 mW).

Tab. 1. Scattering properties of a 1.3 mm thick film of MBBA at room temperature in three selected geometries [49].

	$\vec{v} \parallel \vec{k}, \vec{i} \perp \vec{v}$	$\vec{v} \perp \vec{k}, \vec{i} \perp \vec{v}$	$\vec{v} \perp \vec{k}, \vec{i} \parallel \vec{v}$
α_{lc} (cm^{-1})	4.9	12.1	14.7
$I_{detector}$ (mW)	≈ 25	≈ 10	≈ 7
a (dB/cm)	≈ 23	≈ 54	≈ 66

Although these experiments of Langevin and Bouchiat were performed with a laser at one wavelength only, their model had to consider the wavelength dependence of the turbidity. From the turbidity for different molecular alignments, they derived a formula for an average scattering coefficient $\sigma_{0,cgs}$. Accordingly, an average scattering coefficient $\alpha_{lc,0}$ is used in the current work (SI unit m^{-1}):

$$\alpha_{lc,0} = \frac{\pi}{\lambda_0^{\,2}} \frac{k_B T \Delta\varepsilon}{K_{33} n_o'^{2}} \left[m^{-1}\right] \qquad \text{(Eq. 55)}$$

The scattering cross section of a liquid crystal depends on the elastic properties, the dielectric anisotropy $\Delta\varepsilon$ and the real part of the refractive index n'. The scattering cross section scales with λ_0^{-2}. By using the analysis of Langevin and Bouchiat, the scattering loss of oriented nematic liquid crystals can be evaluated to measure the elastic coefficients.

The anisotropy of the scattering properties was also investigated in nematic liquid crystal waveguides with a rectangular core [14]. Hu and Whinnery [14] reported experiments on the loss of such an MBBA waveguide (with a rectangular profile) which was manufactured by properly aligning glass plates and subsequently filling the gap. A uniform alignment of the liquid crystal was generated by rubbed anchoring coatings. The glass substrates were varied in different experiments. The observed losses were lower than expected by their theoretical predictions based on the model of Langevin and Bouchiat.

The expected tendencies were nevertheless reproduced very well. The waveguide has a rectangular profile. Such a waveguide can be described in a Cartesian coordinate system where the longer edge of the rectangle is parallel to the *x*-direction and the shorter edge is parallel to the *y*-direction. If so, the *z*-direction is the propagation direction. In the reported experiments [14], the scattering cross section $\sigma_{lc,1}$ was observed if the director was oriented parallel to the propagation direction $\left(\vec{\nu} \parallel \vec{k} \parallel z\right)$. $\sigma_{lc,2}$ and $\sigma_{lc,3}$ were observed if the director was oriented parallel to the *x*-direction $\left(\vec{\nu} \parallel x\right)$ and thus perpendicular to $\vec{k}$ $\left(\vec{\nu} \perp \vec{k}\right)$.

$\sigma_{lc,1}$ was observed to be smaller than both $\sigma_{lc,2}$ and $\sigma_{lc,3}$. In a waveguide with a rectangular shape where the long side of the rectangle lays on the *x*-axis, the electric field vector of the *TE*-modes and the magnetic field vector of the *TM*-modes can be assumed to be parallel to the *x*-direction in analogy to the theory of slab-waveguides [2]. In a liquid crystal-filled waveguide with rectangular shape, the losses of the *TE*- and *TM*-modes are degenerate if the director is oriented parallel to the propagation direction. In a similar waveguide where $\vec{\nu} \parallel x$, the anisotropy of the scattering loss leads to higher losses of the *TE*-modes compared to the losses of the *TM*-modes (Tab. 2).

Tab. 2. Losses of a MBBA waveguide with a rectangular shape [14, the data was extracted from a figure].

	$\vec{v} \parallel \vec{k}, TM$	$\vec{v} \parallel \vec{k}, TE$	$\vec{v} \parallel x, TM$	$\vec{v} \parallel x, TE$
$a(theory)$ (dB/cm)	22	22	48	55
$a(fused\ \ silica)$ (dB/cm)	20	22.5	31.5	37
$a(PMMA)$ (dB/cm)	19	19	35	33

2.3.3 Director field inside liquid crystal-filled capillaries (birefringent inclusions)

The equilibrium configurations of liquid crystals in complex geometries have been investigated previously [50]. Already rather simple liquid crystalline phases like nematic and chiral-nematic (cholesteric) phases show various possible director fields in cavities with cylindrical symmetry.

The director fields of nematic liquid crystals in cylindrical capillaries have been studied extensively in the last decades and several director configurations were analyzed. Selected director fields are shown in Fig. 16 and Fig. 17. The director may align parallel to the long axis of a filled cylindrical capillary as shown in Fig. 16a. The liquid crystal has planar anchoring at the boundary interface in this case (parallel director field, [51]). Another possible director field for planar anchoring is the circular planar polar (CPP) director field, where the director is everywhere perpendicular to the capillary long axis (Fig. 17a, [51]). The designations of the director fields in capillaries are varying in the literature. The current work makes use of the designations given in [51]. The director draws two half circles and the director field has two defect lines at the surface of the capillary. The escaped radial director field where the director has perpendicular anchoring at the cavity walls is shown in Fig. 16b and Fig. 17b. Due to the anchoring, the angle Ω between the long axis of the capillary and the local director is 90° near the cavity walls. Ω is varied towards the center of the capillary where the local director is parallel to the capillary long axis $(\Omega = 0°, 180°)$. The director escapes from the profile as seen in Fig. 17b. Defects may occur because both $\Omega = 0°$ or 180° are possible (point like hedgehog and hyperbolic defects [52, 53]). One additional example for a director field with

perpendicular anchoring is shown in Fig. 17c. The director is again perpendicular to the capillary long axis and has two polar defects (planar polar director field [52]).

The director fields inside capillaries are sometimes very complex. For example, precisely tailored defects have recently been created inside cylindrical micro pores with a spatially periodic variation of the pore diameter in the field of photonic crystals [53, 54]. Numerical methods can provide the director fields in such complicated geometries. Generally, a stable configuration of the nematic liquid crystal is observed if the Franck free energy is minimized. Defect free director fields inside of capillaries with homogeneous core diameters have been described by analytical approximations. Appropriate formulas are reported in the literature where cylindrical coordinate systems are used.

The parallel director field, the escaped radial director field, and the circular planar polar director field are used in the current simulations in order to describe the dielectric tensor inside cylindrical liquid crystal inclusions. Moreover, the real case of finite perpendicular anchoring is considered in contrast to the ideal case which is shown in Fig. 16b and Fig. 17b. The simulations are conducted in Cartesian coordinates (*x*, *y*, *z*). The relative dielectric tensor $\varepsilon_{r,i}$ is obtained from the director field [16] (where $\delta_{a\beta}$ is the Kronecker symbol):

$$\varepsilon_{r,i} = \varepsilon_{a\beta} = n_o^{\,2}\delta_{a\beta} + \left(n_e^{\,2} - n_o^{\,2}\right)\nu_a\nu_\beta;\ \ \alpha,\beta = x,y,z. \qquad \text{(Eq. 56)}$$

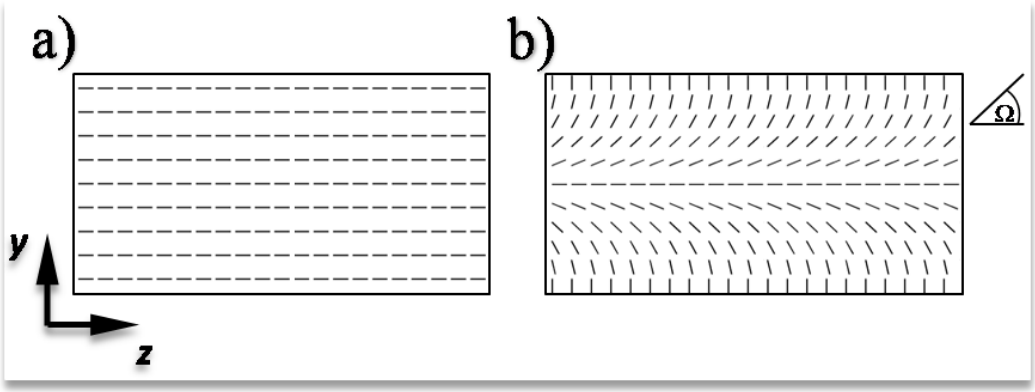

Fig. 16. Two possible director fields of a nematic liquid crystal inside a capillary (long axis in *z*-direction). a) parallel director field, b) escaped radial director field.

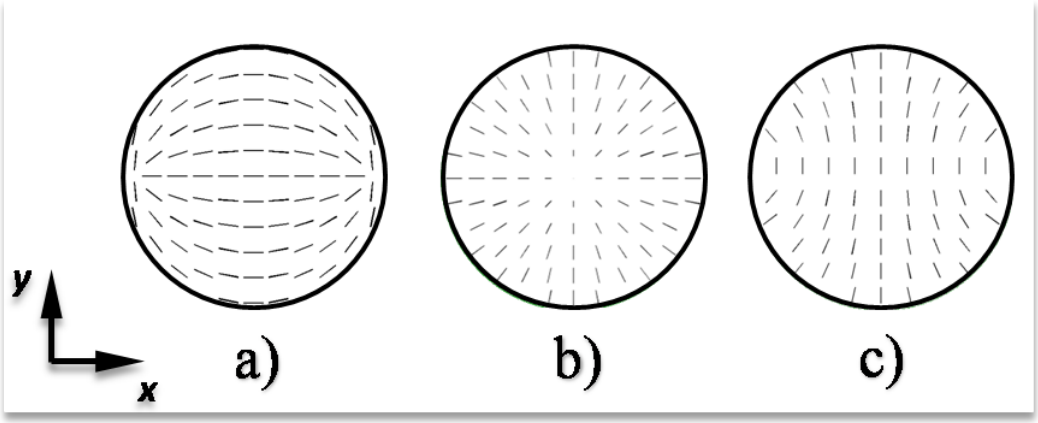

Fig. 17. Profiles of possible director fields of a nematic liquid crystal inside a capillary. a) circular planar polar (CPP), b) escaped radial, c) planar polar (PP) [51].

The following formulae make use of the radial coordinate r and the polar angle θ in terms of a clearer notation. These formulae can be directly used in Cartesian coordinates by inserting the respective expression in Cartesian coordinates. The CPP and PP director field are obtained from one single formula [51] where a factor $C=1$ results the CPP director field and $C=0$ results the PP director field:

$$r=\sqrt{x^2+y^2+z^2} \qquad \text{(Eq. 57)}$$

$$\theta=\operatorname{acos}\left(\frac{x}{r}\right) \qquad \text{(Eq. 58)}$$

$$\psi=\operatorname{atan}\left(\frac{r^2\sin(2\theta)}{r^2\cos(2\theta)}-R_i^{\,2}\right)+\frac{\pi}{2}+C\frac{\pi}{2} \qquad \text{(Eq. 59)}$$

$$\vec{v}=\begin{pmatrix}\cos(\psi)\\ \sin(\psi)\\ 0\end{pmatrix} \qquad \text{(Eq. 60)}$$

In the case of finite anchoring, the escaped radial director field is characterized by two parameters. The parameter η is the ratio of the two Franck elastic constant K_{33} and K_{11} ($\eta=1$ can be used in the one constant approximation):

$$\eta=\frac{K_{33}}{K_{11}} \qquad \text{(Eq. 61)}$$

The second parameter σ describes the influence of the anchoring energy $W_{anchoring}$ and the elastic constant K_{24}. σ scales linear with the inclusion radius R_i :

$$\sigma = \frac{W_{anchoring} R_i}{K_{11}} + \frac{K_{24}}{K_{11}} - 1 \qquad \text{(Eq. 62)}$$

The escaped radial director field is then obtained as function of the radial coordinate r :

$$v_z = \cos\left(\operatorname{atan}\left(\sqrt{\sigma^2 - \frac{1}{\eta}} \cdot \frac{r \cdot R_i}{R_i^{\,2}(\sigma+1)} - r^2(\sigma - 1) \right) \right), \qquad \text{(Eq. 63)}$$

$$\vec{v} = \begin{pmatrix} \frac{x}{r}\cos(\operatorname{asin} v_z) \\ \frac{y}{r}\cos(\operatorname{asin} v_z) \\ v_z \end{pmatrix}. \qquad \text{(Eq. 64)}$$

The influence of η is shown for a constant value $\sigma = 10$ in Fig. 18. Near the walls of the cavity, the escape of the director from the profile is stronger for larger values of η.

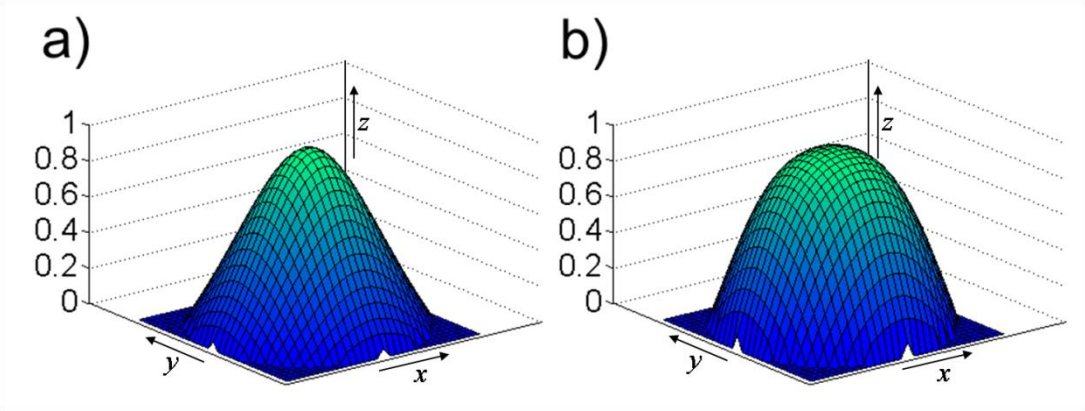

Fig. 18. Influence of the parameter η. Plots of the *z*-component of the escaped radial director field inside a cylindrical liquid crystal inclusion. a) $\eta = 1$, b) $\eta = 3$.

The liquid crystal E7 has the elastic coefficients $K_{11} = 11.2 \cdot 10^{-12}\,\mathrm{N}$, $K_{22} = 6.8 \cdot 10^{-12}\,\mathrm{N}$, $K_{33} = 18.6 \cdot 10^{-12}\,\mathrm{N}$ $(\eta = 1.66)$.

Crawford et al. found a value of $\frac{K_{24}}{K_{11}} = 2.6$ for the liquid crystal E7 [55] due to systematical investigations of lecithin coated capillaries with diameters in the range of several μm. Lecithine is used to induce perpendicular anchoring in the current

experiments, as well. The σ -parameter is calculated according to the results reported in [55] for an inclusion radius of $R_i = 1.2$ μm.

$$\sigma(lecithine, E7) = 5.6 \cdot 10^5 \,\mathrm{m}^{-1} \cdot R_i + 1.6$$
$$R_i = 1.2 \cdot 10^{-6} \,\mathrm{m} \Rightarrow \underline{\underline{\sigma \approx 1.7}} \qquad \text{(Eq. 65)}$$

The influence of σ on the escaped radial director field is shown for in Fig. 19 for $\eta = 1.66$. The anchoring is planar for $\sigma = 1$. Small values of sigma correspond to weak perpendicular anchoring. The anchoring strength and the deformation of the director field increase with increasing σ.

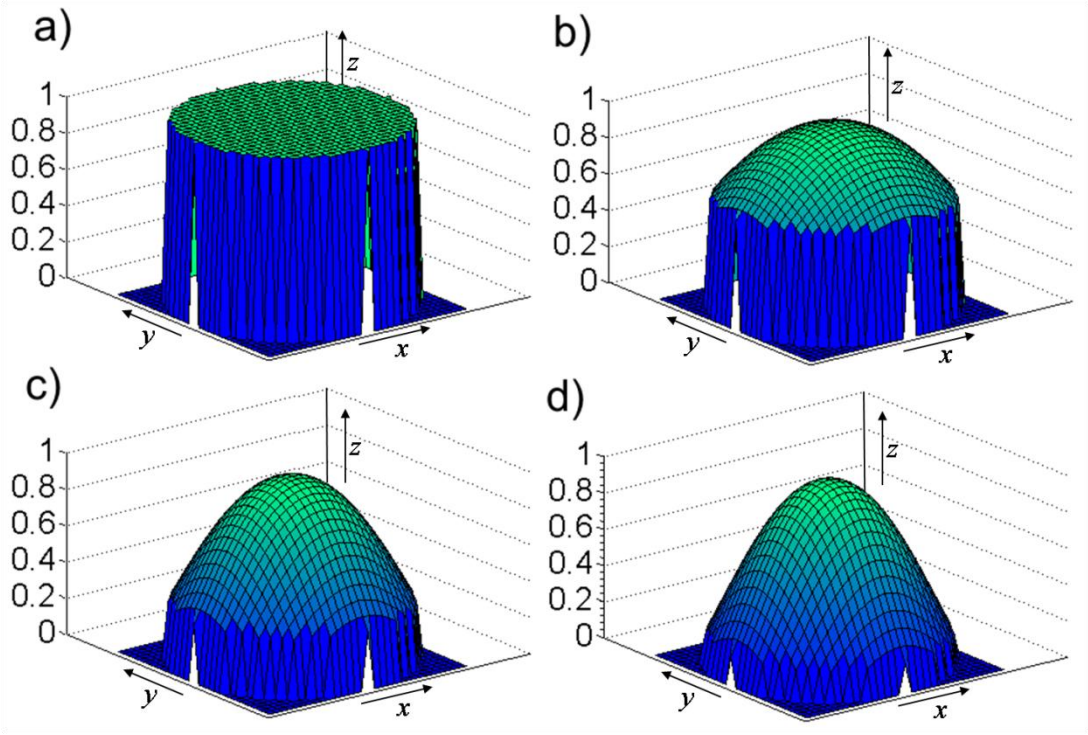

Fig. 19. Influence of the parameter σ on the z-component of the director v_z for an escaped radial configuration inside a cylindrical liquid crystal inclusion. a) $\sigma = 1$, b) $\sigma = 2$, c) $\sigma = 4$, d) $\sigma = 8$.

2.3.4 Dielectric torque

The dielectric anisotropy $\Delta\varepsilon(\omega)$ of nematic liquid crystals (where $\varepsilon_{\parallel}(\omega)$ and $\varepsilon_{\perp}(\omega)$ are the principal dielectric permittivities relative to the director $\vec{\nu}$) is highly frequency dependent:

$$\Delta\varepsilon(\omega) = \varepsilon_{\parallel}(\omega) - \varepsilon_{\perp}(\omega). \qquad \text{(Eq. 66)}$$

However, in the range from static addressing fields to frequencies in the kHz region, several widely used nematic liquid crystals can be described as a medium with no dielectric dispersion and instant dielectric response [56]. Typical nematic liquid crystals show a dielectric anisotropy of $|\Delta\varepsilon| \leq 12$ in this frequency range. A liquid crystal cell can be electrically addressed in order to induce a reorientation of the director field. Such a reorientation can be described by a dielectric torque, which depends on the angle $\gamma_{\nu E}$ between the addressing field vector $\vec{E}$ and the director:

$$\begin{aligned} \Gamma_E &= \varepsilon_0 \Delta\varepsilon \left(\vec{\nu} \cdot \vec{E}\right) \vec{\nu} \times \vec{E} \\ \Leftrightarrow \Gamma_E &= \varepsilon_0 \Delta\varepsilon \left(|\vec{\nu}| \cdot |\vec{E}|\right)^2 \frac{\vec{\nu} \times \vec{E}}{|\vec{\nu} \times \vec{E}|} \cos(\gamma_{\nu E})(\sin \gamma_{\nu E}). \end{aligned} \qquad \text{(Eq. 67)}$$

The direction of this torque is perpendicular to the plane of $\vec{\nu}$ and $\vec{E}$, which is predetermined by the unit vector $\frac{\vec{\nu} \times \vec{E}}{|\vec{\nu} \times \vec{E}|}$. However, the sign of Γ_E depends on the angle $\gamma_{\nu E}$. The product $\cos(\gamma_{\nu E})(\sin \gamma_{\nu E})$ is periodic with the interval 180° where it has two zeros (at 0°=180° and 90°). If the dielectric anisotropy has positive sign, the stable configuration of the director is parallel to the electric addressing field $(\gamma_{\nu E} = 0°)$. In contrast, the stable configuration of the director is perpendicular to the electric addressing field ($\gamma_{\nu E} = 90°$) if the sign of $\Delta\varepsilon$ is negative.

Thus, the optical axis of a nematic liquid crystal can be aligned either parallel or perpendicular to the field direction, if the dielectric anisotropy $\Delta\varepsilon$ has positive or negative sign, respectively.

3. Experiments

3.1 Coating and filling of capillaries and fibers

The investigated capillaries and the holey cladding of the investigated LMA-8 and LMA-10 fibers are coated with substances (anchoring agents) that induce a defined homogeneous alignment of the liquid crystal molecules at the glass surface. Dilute solutions of these anchoring agents are pressed in the capillaries by using a mild pressure gradient (< 1 bar).

DYNASYLAN® GLYMO[2] (glymo) promotes planar anchoring of the liquid crystal. Thus, the nematic director is aligned parallel to the surface. In contrast to anchoring agents which additionally promote an orientation parallel to a rubbing direction, the director can have arbitrary orientation in the plane parallel to a glymo coated surface. Glymo is applied as a 1% solution in a 50% isopropanole water mixture.

Lecithine generates perpendicular anchoring of the liquid crystal director. Lecithine consists of hydrolipides which anchor with the hydrophilic part at the hydrophilic glass surface. The hydrophobic rests stand perpendicular to the glass surface and transfer this alignment to the organic liquid crystal molecules. A solution of lecithine[3] (16 $mg \cdot L^{-1}$) in petroleum ether is used in order to coat the glass surfaces.

After the filling with these solutions, the solvents are allowed to evaporate at 110 °C for two hours. The samples are then filled with the liquid crystals using a mild pressure gradient supporting the capillary forces again. The liquid crystal-filled samples are once more heated to 110 °C and slowly cooled to room temperature. Pieces with a length of several cm can be fabricated by this process. Infiltration times from several hours to several days are required.

The alignment of the liquid crystal is essential for optical applications. By just varying the anchoring, the transmission properties of a liquid crystal-filled photonic crystal fiber device can be changed dramatically.

[2] 3-glycidoxypropyltrimethoxysilane, Evonik Degussa GmbH
[3] lecithine from eggs (CAS-Nummer: 8002-43-5).

3.2 Influence of anchoring conditions

The refractive index in a birefringent medium [57] can be described by a second rank tensor. The wavelength and the speed of light depend strongly on the angle of incidence and the state of polarization. Polarized light can be described by the superposition of two perpendicular linearly polarized waves (Jones-formalism). A birefringent medium creates a relative phase difference between these two waves. The state of polarization can very effectively be varied by birefringent media. A liquid crystal-filled capillary shows interesting stripe textures if the capillary is observed between crossed polarizers with monochromatic light. These textures are well understood and can be calculated by analytical approximations of the director field inside the capillaries [58 ,59].

Single capillaries can be investigated by means of polarizing optical microscopy. The large number of small capillaries in the filled photonic crystal fibers hinders a detailed analysis. Nevertheless, polarizing optical microscopy can be used to inspect the filled photonic crystal fibers and select pieces with apparently good filling and homogeneous textures. Generally, filled fibers with glymo as anchoring agent appear dark if the long axis of the fiber is parallel to one of the polarizers. However, lecithine filled fibers commonly appear bright in this case.

Fused silica cylindrical capillaries with varying diameters are coated with either glymo or lecithine and filled with E7 (as a model for the fused silica photonic crystal fibers). The capillaries are investigated by means of transmitted light polarizing optical microscopy. Calculations of the corresponding intensity textures are compared to the observed textures in order to identify the type of director field inside the capillaries.

Planar anchoring induces a parallel director field where the optical axis is parallel to the long axis of the capillary (uniaxial case). The state of polarization is not modified if the impinging light is linear polarized parallel or perpendicular to the optical axis. The angle between the electric field vector of the impinging linear polarized light and the optical axis is then 0° or 90°. No transmission is observed between crossed polarizers (Fig. 20, left side, long axis of the capillary parallel to one of the crossed polarizers). For a capillary with 10 μm diameter, a two-striped texture occurs if the long axis of the capillary is rotated 45° (Fig. 20, right side).

For a capillary with the same diameter which is filled with the same liquid crystal the stripe texture is modified strongly if the anchoring agent is changed to induce perpendicular anchoring (Fig. 21). The escaped radial director field can be identified by this stripe texture.

The number of stripes in the textures grows with increasing capillary diameter for both types of anchoring. Capillaries with diameters down to 2 μm can be investigated by means of optical microscopy. The coating procedure is apparently suited very well to induce the escaped radial director field by using lecithine and the parallel director field by using glymo.

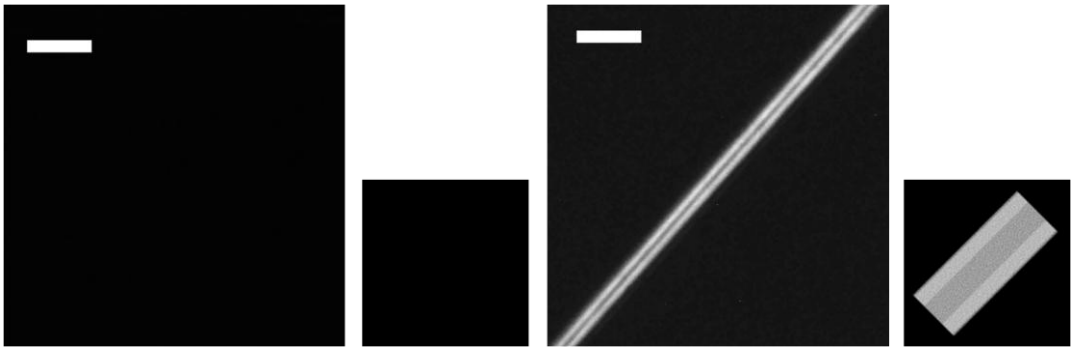

Fig. 20. Transmitted light polarizing optical microscopy of E7-filled 10 μm capillaries with **parallel anchoring** (crossed polarizers, light source: interference filter with 579 nm central wavelength, illuminated with white light). The small pictures show the expected patterns (calculated for 589 nm). The white bar corresponds to a length of 10 μm.

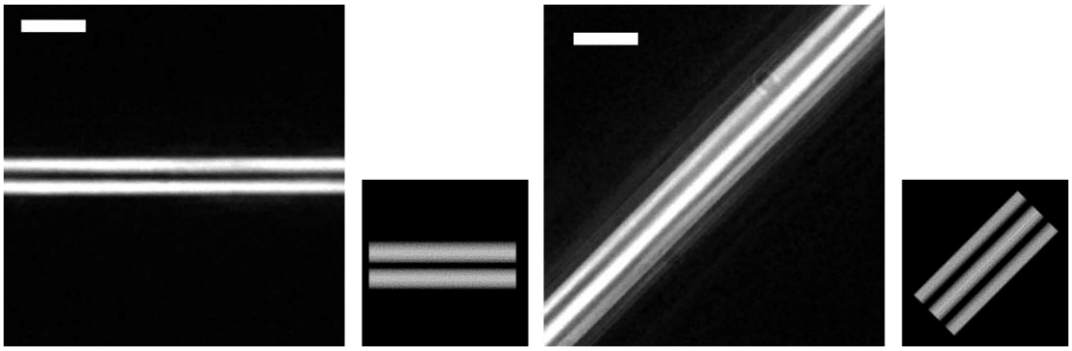

Fig. 21. Transmitted light polarizing optical microscopy of E7-filled 10 μm capillaries with **perpendicular anchoring** (crossed polarizers, light source: interference filter with 579 nm central wavelength, illuminated with white light). The small pictures show the expected patterns (calculated for 589 nm). The white bar corresponds to a length of 10 μm.

3.3 Coupling light into the fibers

Experiments on the waveguiding properties of photonic crystal fibers require precise insertion of light into the core. This coupling of light into the core involves high quality optics and adjusters even for conventional optical fibers. In principle, a fiber can be properly adjusted to the focus of a microscope lens. A parallel light beam (which comes from infinity) is then very well focused on the core region of the fiber and a reasonable part of the intensity is accepted and guided in the core. However, undesired cladding modes are also excited by this technique. In standard single-mode optical fibers, such cladding modes are commonly dampened by a well chosen polymer coating and are eliminated after a certain propagation length. The light which is confined in the core of an optical fiber can have a high power density. High power can accordingly be delivered by such a fiber. But the out coming light is divergent at the fiber end. Nevertheless, the end of an optical fiber is a very good light source for a photonic crystal fiber, provided that the two fibers have a matching core size. Light is inserted into the core of a photonic crystal fiber selectively by splicing it to an appropriate optical fiber. The splicing loss is minimized if the fibers are spliced in an index matching environment. Conventional optical fibers and photonic crystal fibers are commonly directly connected by fusion splicing. However, this technique cannot be applied to liquid crystal-filled fibers because of the high thermal impact.

In the current experiments, the investigated filled photonic crystal fibers were spliced to conventional optical fibers by a glue-technique (Fig. 22). Both fibers are cut precisely with an optical fiber cleaver[4] (equipped with a diamond blade) to create plane end faces. The ends of the two fibers are exactly adjusted[5] face to face so that white light coming from the standard optical fiber is inserted into the core of the photonic crystal fiber with a high coupling efficiency. Simultaneously, the free end of the photonic crystal fiber is observed with a 40x microscope lens and a CCD-camera[6]. This near field analysis helps to make sure that the transmitted light is guided in the fiber core and not in the cladding of the filled photonic crystal fiber. In the coupling step, white light from a halogen source is transmitted through the

[4] Tritec TC-II+ optical fiber cleaver.
[5] Elliot Gold™ series XYZ flexure stage MDE122.
[6] Kappa CF 11/3.

standard optical fiber[7]. With such a white light source, high intensity is transmitted through both fibers independently of the attenuation spectrum of the filled photonic crystal fiber. The coupled end pieces of the fibers are embedded in a droplet of photo curable optical adhesive[8]. The fibers are once more readjusted to cause maximum transmission and the optical adhesive is then photo cured with UV-radiation[9]. A stable splice of the two fibers with high mechanical stability and minimum insertion loss is generated. The glass core of a filled fiber shows a high transmission. Interestingly, scattering losses occur in the liquid crystal-filled sections although the core is selectively excited (Fig. 22).

Fig. 22. Coupling of a 980 HP (optical fiber with an diameter of 125 μm) fiber with a filled photonic crystal fiber (with solid core). The figure shows three digital photographs which were taken with an optical microscope (upper picture: transmitted light). Approximately, a fiber length of 1 mm is shown for both fibers. White light is coupled to the optical fiber and is then transmitted through the photonic crystal fiber. Both fibers are accurately aligned so that near field optical analysis of the free end of the photonic crystal fiber shows exclusively transmission in the core. The splice is stabilized in photo curable optical adhesive. The central picture shows the situation if the microscope light source is turned off (taken with high exposure time). Coupling losses occur at the splicing point. The lowest picture is a copy of the central picture. Contrast and brightness are adjusted in order to show that high scattering losses occur in the photonic crystal fiber.

[7] Thorlabs 980 HP (Nufern 980-HP), mode field diameter 4.2±0.5 μm @ 980 nm, NA = 0.2.
[8] Norland optical adhesive No. 61.
[9] UV-LED (intensity maximum at λ = 365 nm).

3.4 Attenuation spectra of two solid core photonic crystal fibers filled with the liquid crystal E7

In order to record attenuation spectra, an adjustable monochromatic light source is used, which consists of a Xenon-arc-source and a fiber coupled monochromator. This source is special set-up as part of these investigations. The white light from the arc-source is transmitted through the computer controlled grating monochromator[10] with a focal length of 300 mm and is then coupled to the light-delivery fiber of a sample. The transmitted monochromatic light is collected with a microscope lens and analyzed by means of a photomultiplier tube (PMT[11]). The cut-back technique can be applied due to the stable splicing situation of the standard optical fiber and the filled photonic crystal fiber. The monochromator is adjusted with a step width of 2 nm in order to record the first spectrum. Subsequently, the filled photonic crystal fiber is cut back and the second spectrum is recorded. The attenuation characteristic of the filled fibers is usually observed by cutting pieces in the range of a few cm in length. If necessary, the back-cutting process can be repeated until the contrast of the recorded spectra is sufficient to calculate significant attenuation spectra $a(\lambda_0)$.

The two commercial photonic crystal fibers LMA-8 and LMA-10 (NKT photonics, Tab. 3) were filled with the well-known nematic liquid crystal E7[12]. The fibers consist of fused silica and have a very uniform structure (Fig. 11). The inclusions are arranged in a nearly perfect trigonal lattice. In contrast to experimental fibers, the pitch p and the inclusion radii R_i of these commercial fibers are highly uniform over the entire fiber length.

Tab. 3. Fiber parameters of the filled fibers (NKT-photonics).

	p (µm)	R_i (µm)	d_{core} (µm)
LMA-8	**5.5**	**1.24**	**8**
LMA-10	**6.5**	**1.5**	**10**

[10] LOT Oriel Omni-λ 3009
[11] Hamamatsu R928
[12] E7: 51% 5CB, 25% 7CB, 16% 8OCB, 8% 5CT

The core diameters of both fibers are comparable to the core diameters of standard single-mode optical fibers for the infrared spectral range (≈ 9 μm). In sum, these properties make the fibers particularly suitable for cut-back experiments.

The liquid crystal E7 is well-known in the literature. It is a good choice for the filling experiments because it is a quite representative nematic liquid crystal with a refractive index $n_o(589\,nm) = 1.5225$, which is higher than the refractive index of the fused silica. E7 has a typical birefringence of $\Delta n = 0.3$ a melting point of -10 °C, and a clearing temperature of 65 °C, which allows experiments at room temperature. The elastic properties and the dielectric anisotropy of $\Delta\varepsilon =$ 12 in the kHz region are also representative for the cyanobiphenyle type of nematics, so that for example the switching performance demonstrated by addressing with electric fields is exemplary.

The anchoring at the cell boundaries is essential for optical devices with liquid crystals. For nematic liquid crystals, lecithine is used to induce perpendicular anchoring at the glass surfaces and glymo is used to induce planar anchoring. Both types of anchoring can be used in capillaries and also in photonic crystal fibers. The variation of the boundary conditions is essential for the transmission properties.

After filling with the liquid crystal E7, the inclusions of the two LMA fibers exhibit higher refractive indices than the refractive index of fused silica. The average refractive index of the cladding is now higher than the refractive index of the core.

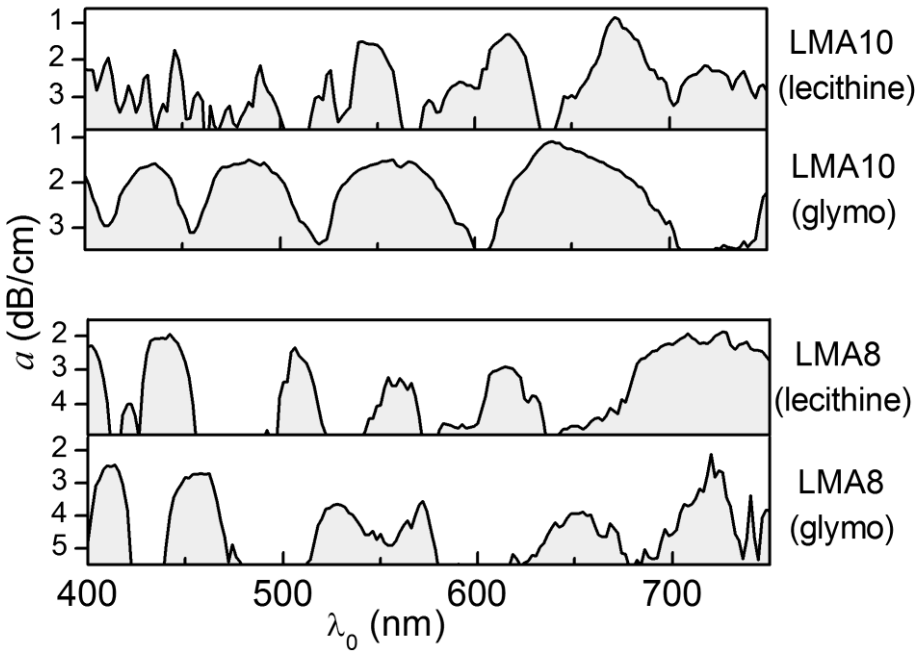

Fig. 23. Attenuation spectra of two filled photonic crystal fibers (LMA-8 and LMA-10).

As expected, the recorded attenuation spectra of the filled fibers LMA-8 and LMA-10 (Fig. 23) clearly show a windowed transmission in all four cases. Interestingly, the spectra of the same fiber are strongly varied by changing the anchoring condition from lecithine to glymo. The observation of transmission windows with low attenuation is in promising contradiction to earlier observations on the wave guiding properties of liquid crystal-filled waveguides with a rectangular shape [14], which indicated a very high attenuation in the entire visible wavelength range due to scattering losses. Obviously, the photonic crystal fibers investigated show a core with very high transmission, while losses are caused by scattering due to the liquid crystal inclusions. In Fig. 23, the loss is plotted in dB/cm. The minimum loss of fiber LMA-8 with planar anchoring is lower than 2 dB/cm. The losses are slightly higher for perpendicular anchoring than for planar anchoring for this fiber. The minimum losses of the filled LMA-10 fibers are even lower than 1 dB/cm for both types of anchoring. For the LMA-10 fiber, the attenuation minima of the individual transmission windows decrease with increasing wavelength as expected from the scattering cross section of liquid crystals, which also decreases with increasing wavelength.

The experiments show the typical windowed transmission of bandgap guiding fibers. The investigations lead to liquid crystal waveguides where the intensity is confined in a core region, which consists of fused silica. Liquid crystal waveguides with low attenuation windows are obtained for all wavelengths in the investigated spectral region by filling of the two fibers with the liquid crystal E7 and varying the anchoring.

3.5 Addressing experiments

3.5.1 Setup for the addressing with a. c. signals

Filled fiber pieces with a length of approximately 15 mm were assembled into two different capacitor setups (Fig. 24). In both cases, the liquid crystal-filled fibers are glued in between two ITO-coated glass plates. Several short, unfilled fiber pieces are also assembled in the gap as spacer. The thickness of the gap is thereby kept constant. The filled photonic crystal fiber is cut with a fiber cleaver and the ends are

inspected by reflected light microscopy. If necessary, the fiber ends are cleaned. The conducting side of an indium tin oxide (ITO) coated glass plate is covered with an appropriate portion of photo curable optical adhesive[13] and the filled fiber is then assembled into the covered section. The free end of the filled fiber must not be covered with optical adhesive at any time; the filled photonic crystal fiber has a 1 mm overhang over the glass plate. In contrast, the end of the photonic crystal fiber which is designated to be spliced to the light-delivery fiber (splicing end) may be covered with optical adhesive. Two enamelled copper wires are now strained parallel to the fiber in case of the four electrode setup (Fig. 24 b). The sample is then covered with a second ITO-coated glass plate. The quality of the alignment is inspected with the microscope. The splicing end of the fiber is covered by a mask and the unmasked optical adhesive is photo cured by exposure to the radiation of a high power UV-LED. Subsequently, the splicing end of the fiber is still accessible because the optical adhesive in this region is still uncured. The filled fiber is spliced to a light-delivery fiber (980 HP fiber) as described before.

Sinusoidal a. c. voltages with a frequency of 1 kHz or several kHz are applied. In case of the two electrode setup, the corresponding electric field is oriented along the *y*-direction (Fig. 24 a). In case of the four electrode setup, the corresponding electric field is oriented along the *x*-direction if the voltage is applied by using the copper wires (Fig. 25 b). Again, the corresponding electric field is oriented along the *y*-direction if a voltage is applied to the ITO-electrodes (Fig. 25 a). Voltages larger than 350 V_{rms} can be applied to the samples without causing damage.

During the addressing experiments, the end face of the fiber is observed by means of a microscope lens with a polarizer and a PMT-detector[14]. A femtowatt IR-detector[15] is used for investigations in the infrared spectral region. Spectra of the transmitted output power are recorded at first. The monochromator is then adjusted to the wavelength of interest in order to investigate the switching times. Thus, the switching experiments are conducted by observing the transmission of monochromatic light with 2 nm bandwidth. The rise and decay times are evaluated for a 90% answer. This corresponds to the time elapsed until 90% of the full response (steady state) are developed ($t_{0\text{-}90}$). The indices '*on*' and '*off*' are assigned

[13]Norland optical adhesive No. 61, ultraviolet curable (320-380 nm)
[14]Hamamatsu R928
[15]FEMTO FWPR-20-IN femtowatt photoreceiver

to the response times when turning on and off the voltage, respectively. The fibers LMA-8 and LMA-10 have an outer diameter of 125 µm. The measured threshold voltages for a complete decay of the transmission are ≈ 75 V_{rms} (E7). Thus, the critical field strength for the reorientation of the director field of the liquid crystal inclusions is $E_c \approx 0.6$ V/µm.

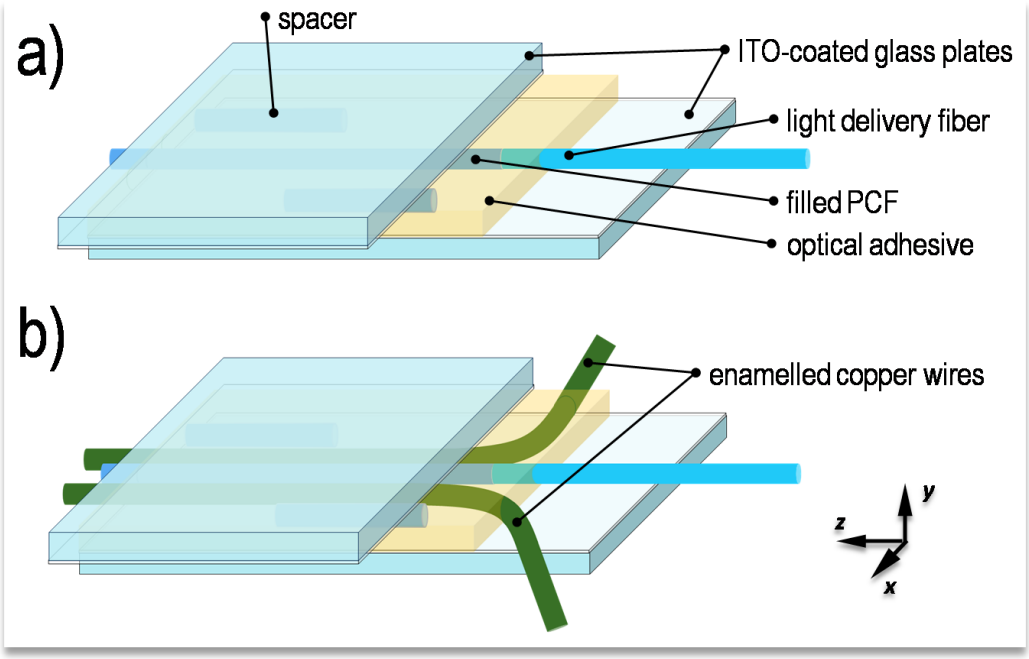

Fig. 24. Addressing setups for filled photonic crystal fibers. a) two electrode setup with two ITO-coated glass plates as electrodes. b) 4 electrode setup with two wire electrodes and two ITO-coated glass plates as electrodes.

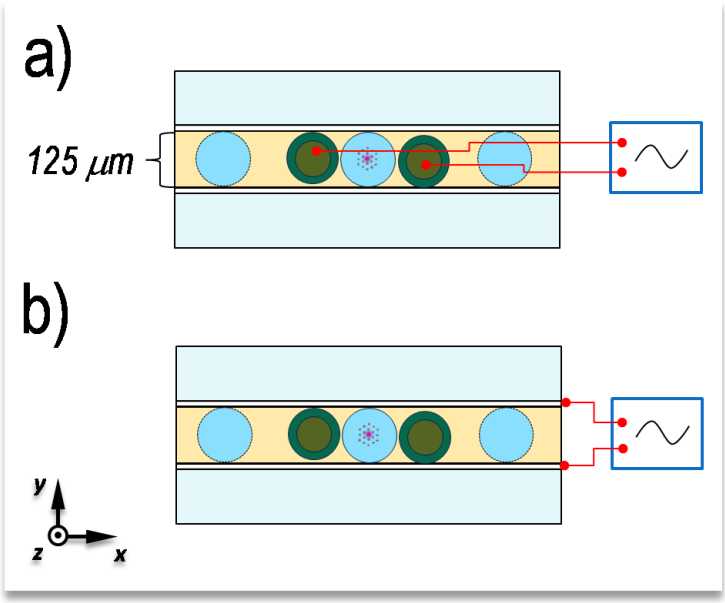

Fig. 25. Bipolar addressing of a photonic crystal fiber with two perpendicular sets of electrodes. a) voltage in *x*-direction, copper wires as electrodes b) voltage in *y*-direction, ITO-coated glass plates as electrodes.

3.5.2 Addressing E7 filled fibers with planar anchoring

These experiments were performed by applying fields in the *y*-direction. It was found for both types of fibers that planar anchoring leads to optical switches with a two stage functionality. The fibers show a polarization independent decay of the transmission as response to voltages in the regime from 50 to ≈ 100 V_{rms}. A polarization dependent effect occurs at higher voltages. Here, the propagation of *x*-polarized light becomes possible again while the *y*-polarized part of the transmitted intensity is strongly attenuated in selected spectral regions. For fiber LMA-10, this is shown in Fig. 26. The spectral distribution of the reappearing *x*-polarized light in the high-voltage state is for both fibers with planar anchoring enveloped by the spectra which are recorded in the zero-voltage state. The fiber LMA-10 shows at high voltages reasonable transmission of *x*-polarized light in the transmission windows around λ_0 = 480 nm, 540 nm and 640 nm.

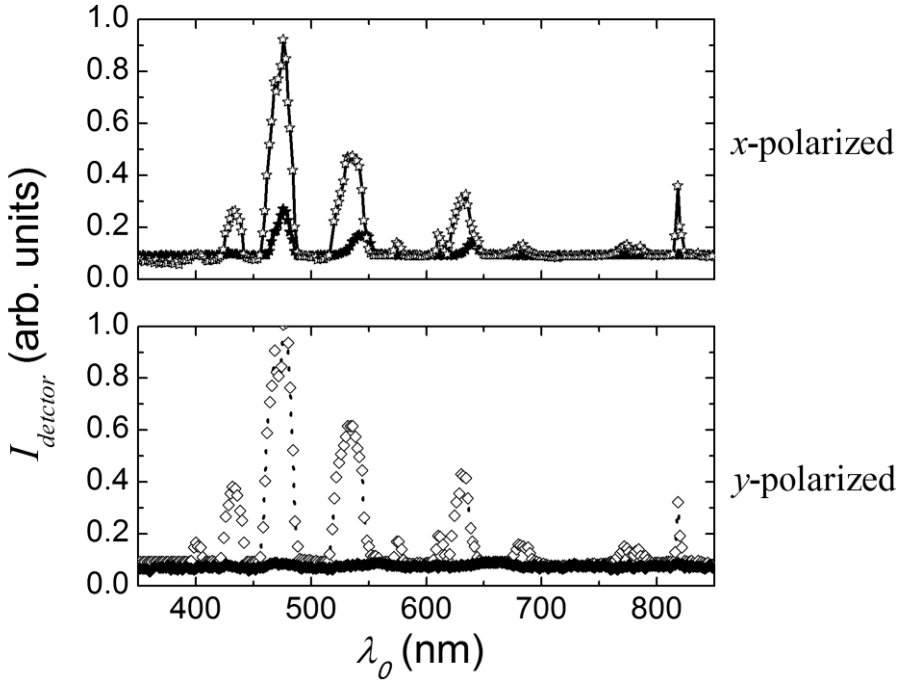

Fig. 26. Fiber LMA-10 treated with glymo and filled with E7. Optical output power vs. wavelength. Spectra without applied voltage (open symbols) and for a high addressing voltage (250 V_{rms} 1 kHz sine, closed symbols) are shown.

The time dependent behavior of fiber LMA-10 is shown in Fig. 27. In this experiment, the transmitted light has a wavelength of $\lambda_0 = 540$ nm. Turning on a voltage causes a decay of the detected intensity for *x*- and *y*-polarized light with a time constant t_{on}. The initial intensity is restored by turning off the addressing signal with a time constant t_{off}. When using voltages up to 100 V_{rms}, switching can be performed with degenerate response of *x*- and *y*-polarized light (polarization independent response). It should be noticed that a complete decay occurs; the intensity measured in the voltage-on state at $t > t_{on}$ corresponds to the dark current of the PMT. As seen from the plots at 200 V_{rms}, exclusively the transmission of *x*-polarized light is partially restored when high voltages are applied. This process is characterized by additional response times $t_{on,2}$ and $t_{off,2}$ ($t_{on,2}$ = 14 ms, $t_{off,2}$ = 3 ms at 200 V_{rms}) and a threshold voltage of ≈ 150 V_{rms}. The switching contrast decreases for higher addressing voltages (Fig. 27). A reason for this may be a rather strong deformation of the director field of the liquid crystal inclusions, which may cause defects. Maybe these defects, which increase the scattering, cannot be completely healed on the timescale of the experiment (1 Hz repetition rate of the switching cycle). Presumably, there is a discontinuous change of the topology of the director field through a transient scattering state. Another reason for the decrease of the switching contrast could be dielectric heating. Enhanced thermal fluctuations can also alter the scattering properties of the liquid crystal-filled inclusions strongly. The response times t_{on} and t_{off} are plotted over the values of the addressing voltage in Fig. 28. It should be noticed that the response time t_{off} increases with increasing voltage. This could be related to the already discussed decrease of the switching contrast (slow healing of the director field, dielectric heating). The response time t_{on} decreases with increasing voltage as expected in analogy to the Fredericks transition [16,44,45]. It is demonstrated that t_{on} can be pushed below 4 ms.

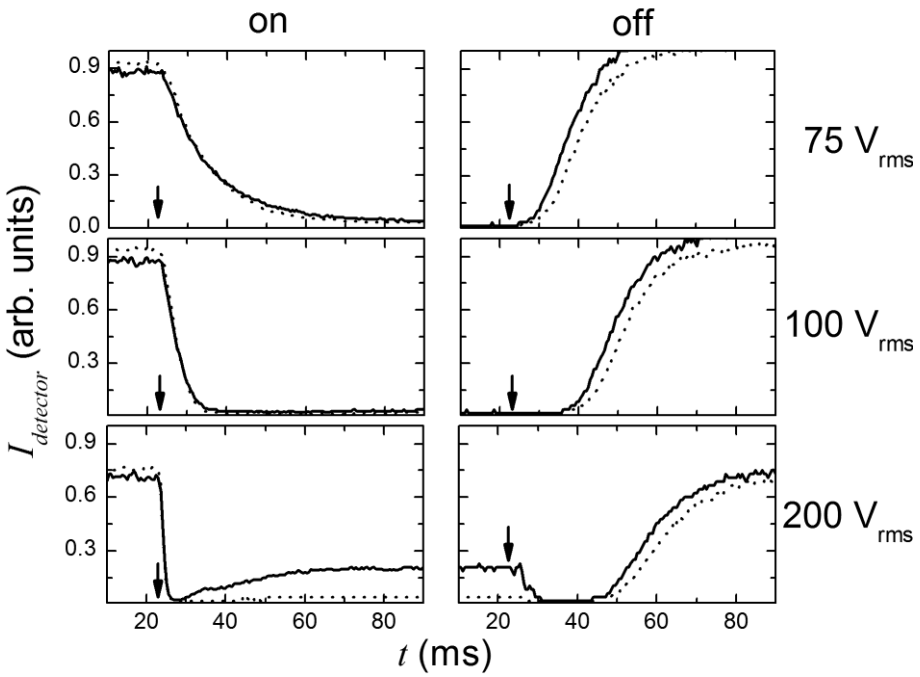

Fig. 27. Fiber LMA-10 treated with glymo and filled with E7. Detected optical output power vs. applied a. c. signal (1 kHz sine) at different voltages. The output power was recorded by transmitting monochromatic radiation at λ_0 = 540 nm through the fiber and observing the end face by using a microscope lens, a polarizer, and a PMT-detector. The switching event occurs at t = 23 ms. The indices 'on' and 'off' correspond to the response times when turning on and off the voltage, respectively. Turning on a voltage causes a decay of the detected intensity for x- and y-polarized light (solid and dotted line, respectively) with a time constant t_{on} (200 V_{rms}: t_{on} - = 3 ms). The initial intensity is restored with a time constant t_{off} (200 V_{rms}: t_{off} = 40 ms) by turning off the addressing signal. Exclusively, the transmission of x-polarized light is partially restored with response times $t_{on,2}$ and $t_{off,2}$ (225 V_{rms}: $t_{on,2}$ = 14 ms, $t_{off,2}$ = 3 ms) by using strong signals > 150 V_{rms}.

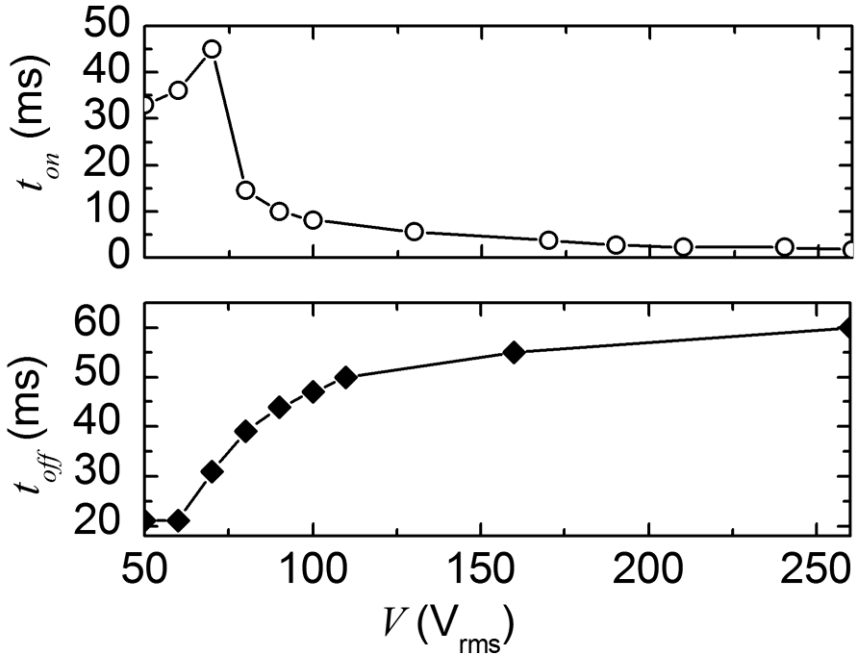

Fig. 28. Fiber LMA-10 treated with glymo and filled with E7. Response times t_{on} and t_{off} vs. applied voltages a. c. (1 kHz, sine). The figure shows the switching times in spectral regions with polarization independent response.

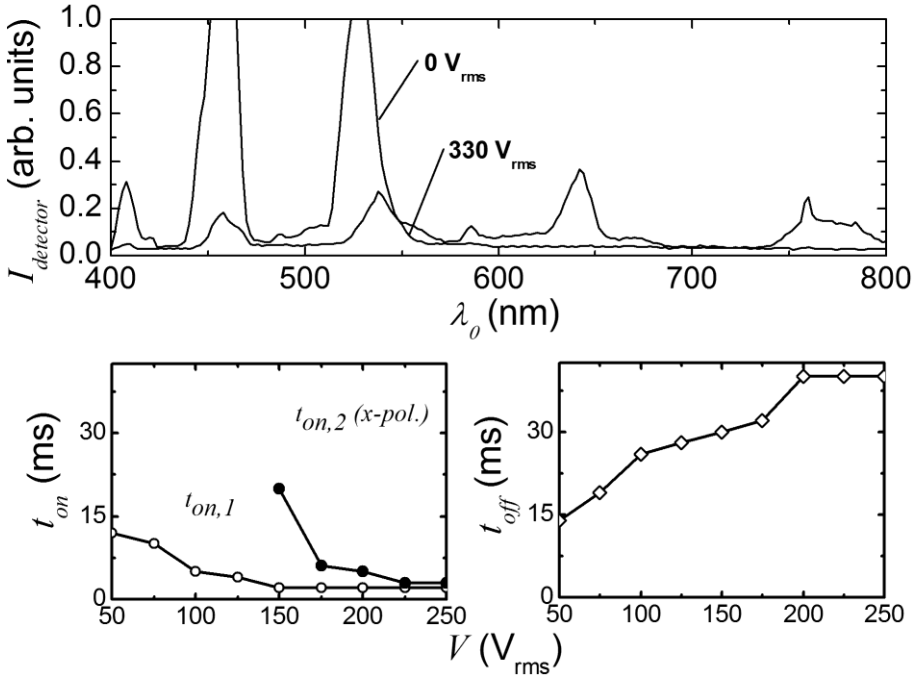

Fig. 29. Fiber LMA-8 treated with glymo and filled with E7. Optical output power of *x*-polarized light vs. wavelength and switching times vs. applied voltage. Like fiber LMA-10 under the same conditions, *x*- and *y*-polarized light is strongly attenuated in the investigated spectral region with a decay time t_{on}. For high addressing voltages, the transmission of *x*-polarized light is partially restored in selected transmission windows with a response time $t_{on,2}$.

The switching behavior of fiber LMA-8 (Fig. 29) is closely related to fiber LMA-10. For addressing voltages lower than 100 V_{rms}, a polarization independent effect occurs; *x*- and *y*-polarized light are completely attenuated. The transmission of *x*-polarized light is partially restored for voltages larger than 150 V_{rms}. Reasonable transmission of *x*-polarized light is detected in the transmission windows around λ_0 = 410 nm, 455 nm and 550 nm. The response times are in the same order of magnitude as for fiber LMA-10 and the switching time t_{on} can once more be pushed below 4 ms.

3.5.3 Addressing E7 filled fibers with perpendicular anchoring

These experiments were again performed by applying fields in the *y*-direction. The experimental results for the fibers with perpendicular anchoring show additional effects compared to the fibers with planar anchoring. Although a complete attenuation of *x*- and *y*-polarized light in fiber LMA-8 is detected for voltages between 75 and 150 V_{rms}, a new transmission window for *x*-polarized light opens up at higher voltages around λ_0 = 460 nm. At this wavelength, the detected intensity exceeds the envelope of the intensity spectrum of the zero-voltage state (Fig. 30).

This fiber exhibits two different addressing possibilities. In the transmission windows of the zero-voltage state, the transmission can be suppressed. This is shown in Fig. 31 for λ_0 = 407 nm. Here, the detected intensity decays once the voltage is present and increases again once the voltage is turned off. The second possibility is also shown in Fig. 31 (to the right). Without applied voltage, there is no intensity detected for a wavelength of λ_0 = 462 nm. But the intensity increases once a high voltage is applied. The switching contrast increases with the applied voltage. The response times are plotted together in Fig. 32. The response times measured at λ_0 = 407 nm resemble the response times of the fibers with planar anchoring. The response time $t_{on}(\lambda_0 = 462\text{ nm})$ is reduced to $t_{on} \approx 10$ ms by using a voltage of 350 V_{rms}. In analogy to the Fredericks transition [16,44,45] t_{on} can possibly be reduced further by applying higher voltages. But noteworthy, the response time $t_{off}(\lambda_0 = 462\text{ nm}) = 3$ ms is apparently independent of the applied voltages (Fig. 31).

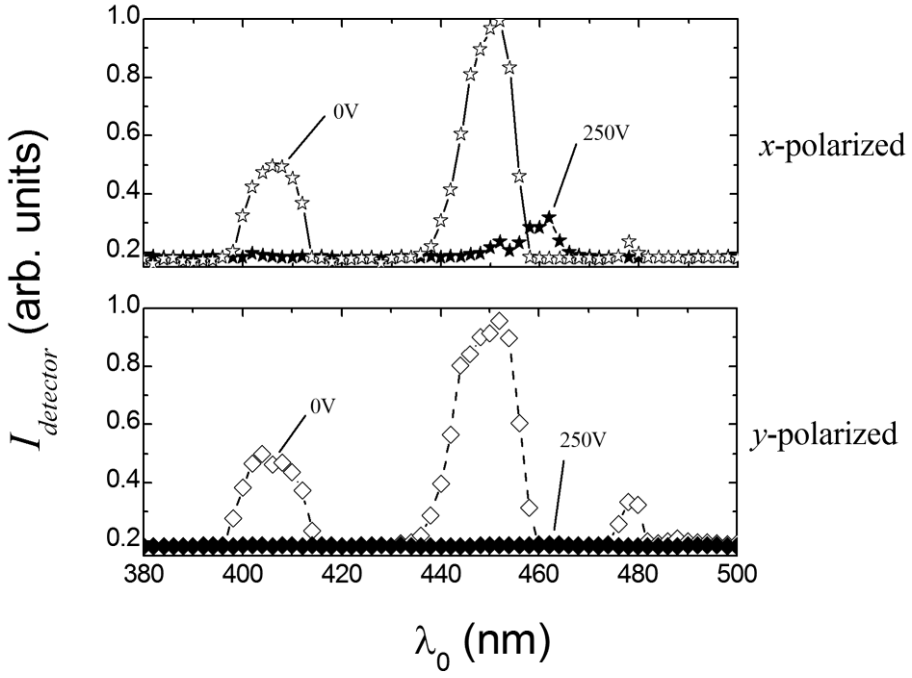

Fig. 30. Fiber LMA-8 treated with lecithine and filled with E7. Optical output power vs. wavelength.

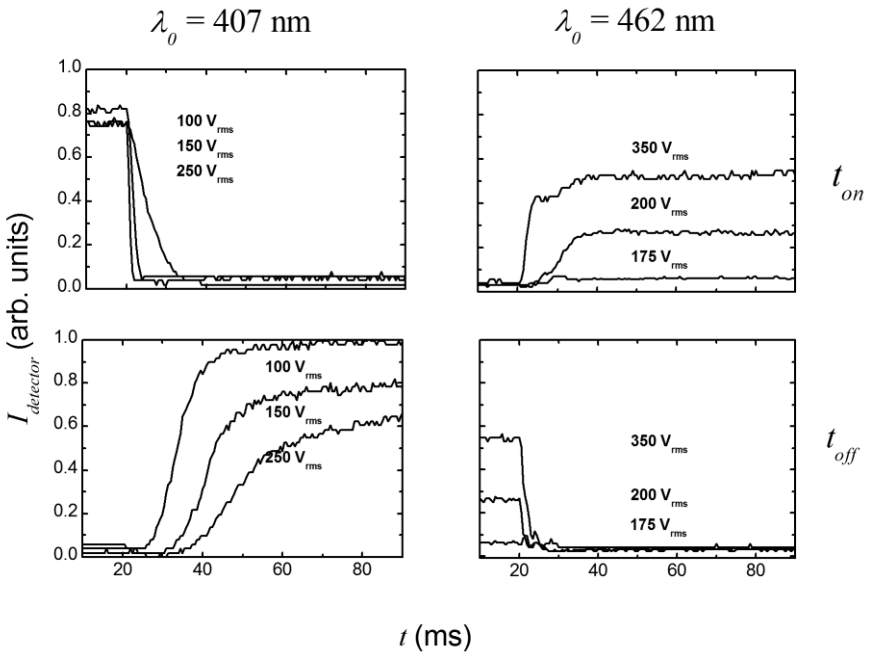

Fig. 31. Fiber LMA-8 treated with lecithine and filled with E7. Detected optical output power vs. applied a. c. signal (1 kHz sine) at different votages. The switching event occurs at t = 20 ms. Turning on a voltage causes a decay of the detected intensity at λ_0 = 407 nm and a rise at λ_0 = 462 nm. When the voltage is turned off, the detected intensity increases at λ_0 = 407 nm and decays at λ_0 = 462 nm.

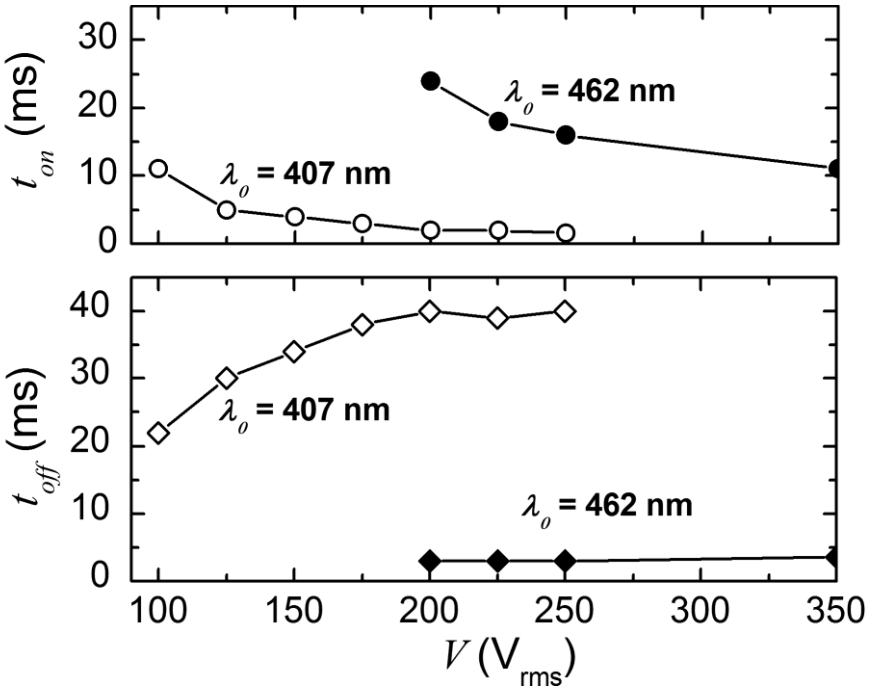

Fig. 32. Fiber LMA-8 treated with lecithine and filled with E7. Response times vs. applied a. c. signal (1 kHz). The transmission decays when turning on a voltage at λ_0 = 407 nm and increases at λ_0 = 462 nm. When the voltage is turned off, the transmission increases at λ_0 = 407 nm and decays at λ_0 = 462 nm.

The experimental results for the LMA-10 fiber with perpendicular anchoring are only weakly polarization dependent when applying voltages up to 350 V_{rms}. The change of the detected optical output power for *x*- and *y*-polarized light is not as pronounced as for the glymo coated fibers. Possibly, the state of polarization of the transmitted light may be influenced in a way that is not detected by simply using a linear polarizer.

However, interesting polarization independent effects are detected (Fig. 33). A voltage of 100 V_{rms} already reduces the detected intensity considerably and the switching contrast increases with the applied voltage. Interestingly, the response seems to be two staged for higher voltages. The response time $t_{on,1}$ = 3 ms is apparently voltage independent. The reorientation process of the director field is also very fast. The initial intensity is restored with a response time t_{off} = 3 ms which is apparently voltage independent, too. As shown in the spectra (Fig. 33), high switching contrasts can be achieved by using a voltage of 350 V_{rms}.

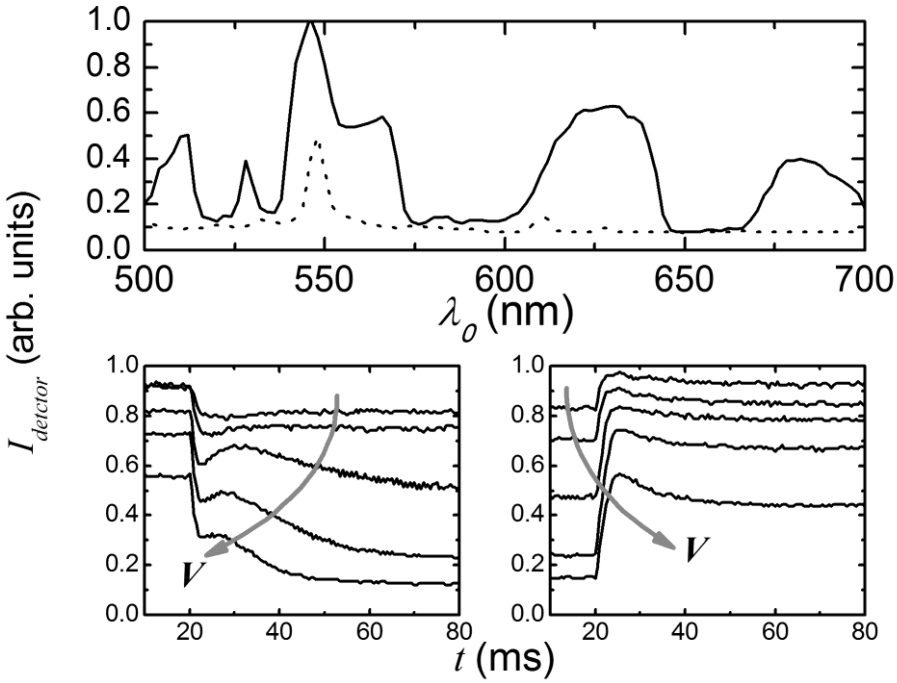

Fig. 33. Fiber LMA-10 treated with lecithine and filled with E7. Optical output power vs. wavelength and vs. time. The switching experiment is conducted at λ_0 = 546 nm. Thereby, the applied voltages are varied from 100 to 200 V_{rms} in steps of 25 V_{rms}. Two spectra are shown in the lower diagram; one at the zero-voltage state (solid line) and one recorded when applying 350 V_{rms} (1 kHz).

3.5.4 Fibers with the dual frequency addressable liquid crystal ZLI 2461

By applying electric fields to nematic liquid crystals, their optical axis can be aligned either parallel or perpendicular to the field direction, if the dielectric anisotropy $\Delta\varepsilon$ is positive or negative, respectively. For dual frequency (DFA) liquid crystals, the sign of $\Delta\varepsilon$ depends on the frequency of the a. c. fields. This peculiar behavior is due to the anisotropy of orientational polarization. For frequencies smaller than the relaxation frequency f_c , the polarization origins from both permanent and induced dipole moments. Above $f_{c,1}$, the orientational polarization is no longer present. For liquid crystals consisting of rod-like molecules, the relaxation frequency $f_{c,1}$ for rotation around the short axes of the molecules is smaller than the relaxation frequency $f_{c,2}$ for rotation around the long molecular axis. If the liquid crystal exhibits sufficiently large components of the permanent dipole moment both parallel and perpendicular to the molecular axes, the dielectric anisotropy $\Delta\varepsilon$ as a

function of frequency f may change the sign at $f \approx f_{c,1}$ (Fig. 34, [60]). If so, the orientation can be actively realigned in either direction by choosing the frequency, appropriately.

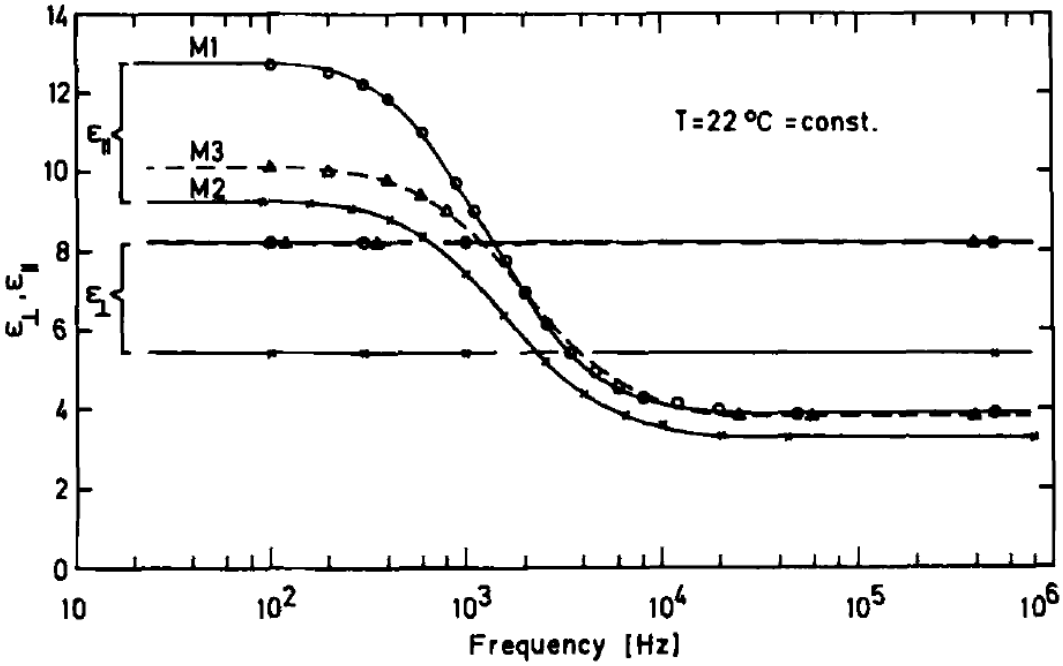

Fig. 34. Frequency dependence $\varepsilon_{\parallel}(f)$ of three different nematic liquid crystal mixtures M1, M2, and M3 with varying composition. The mixtures consist of two classes of compounds; strongly negative dielectric anisotropic compounds and compounds with very low crossover frequencies $f_{c,1}$ and large longitudinal permanent dipole moments. As expected from the high relaxation frequency for the rotation around the long molecular axis, $\varepsilon_{\perp}$ exhibits no dispersion in the shown frequency range. Figure copied from [60].

In the no-voltage state, polarization optical microscopy of capillaries with planar anchoring of the liquid crystal reveals a uniform director field with the optical axis parallel to the long axes of the capillaries. This type of director field is also expected inside the inclusions of the filled photonic crystal fibers with the same type of anchoring. The addressing experiments with E7 filled fibers lead to very interesting polarization dependent and independent switching effects. However, the sign of the dielectric anisotropy of E7 is positive, independent of the frequency. Thus, the total time for an on/off switching cycle is limited by the response time for the relaxation of the director field t_{off} in the case of planar anchoring. Unfortunately, t_{on} decreases, while t_{off} increases with the applied voltage under these conditions. In a comparable system, the uniaxial director field in the no-

voltage state could possibly be stabilized by using a dual frequency addressable liquid crystal.

The attenuation spectra of the E7 filled fibers indicate lower losses for fiber LMA-10. This fiber is used for the current experiments with a DFA liquid crystal due to this observation. The DFA liquid crystal mixture ZLI 2461 from Merck is applied. This mixture exhibits positive dielectric anisotropy below the critical frequency f_c (≈ 6 kHz) and negative dielectric anisotropy for $f > f_c$.

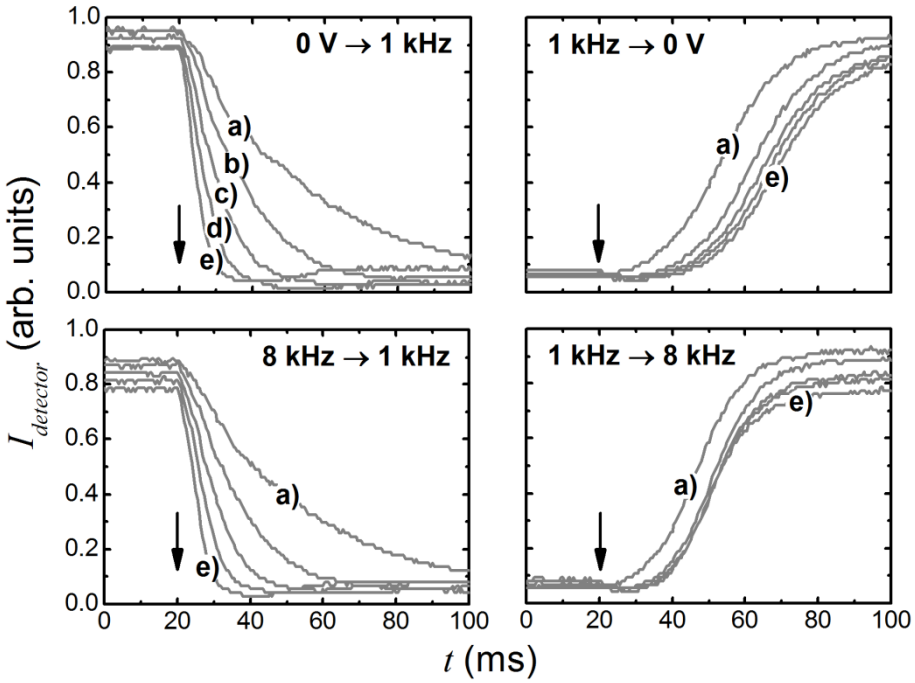

Fig. 35. Fiber LMA-10, filled with ZLI 2461, planar anchoring. Light with a wavelength of 484 nm is transmitted. The arrows indicate the switching event on the time axis. The fiber is addressed with voltages of a) 350 V_{rms} b) 380 V_{rms}, c) 450 V_{rms}, d) 540 V_{rms}, and e) 600 V_{rms} for f = 1 kHz. The 8 kHz voltages are 80 % of these values, due to the amplifier. The upper two graphs show the response when the 1 kHz voltage is turned on and off. The lower two graphs show the response when switching from 8 kHz to 1 kHz and vice versa.

As in the preceding sections, the experiments were performed by applying fields in the *y*-direction. The fiber shows a windowed transmission and a particularly high switching contrast at λ_0 = 484 nm. Two different switching experiments are conducted at this wavelength. In analogy to the E7 filled fibers, the first switching experiment is performed by switching on and off a 1 kHz a. c. signal. The voltage is varied from 350 V_{rms} to 600 V_{rms} ($t_{on,350V}$ > 40 ms, $t_{on,380V}$ = 39 ms, $t_{on,450V}$ = 21 ms, $t_{on,540V}$ = 21 ms, $t_{on,600V}$ = 10 ms, Fig. 35). The response time t_{off} = 60 ms is apparently independent of the voltage. The response times are higher compared to

the E7 filled fibers and the applied voltages are also higher than the voltages used for the E7 filled fibers. This is expected, because E7 has a dielectric anisotropy of 12 whereas ZLI 2461 has at lower frequencies only a dielectric anisotropy of 2.4 [16].

The second experiment is performed by switching from an 8 kHz a. c. signal to an 1 kHz a. c. signal and back. The amplifier used in this experiment has at 8 kHz 80 % of the gain which it generates for 1 kHz signals. The amplitudes of the addressing fields are thus asymmetric. The response times t_{on} are not considerably influenced in the experiment (Fig. 35, lower graphs). The switching contrast is reduced by ≈ 5 % compared to the first switching experiment. This observation may contradict the initial idea of stabilizing the uniaxial director field. Nevertheless, the response time t_{off} = 60 ms is replaced by a shorter response time $t_{1kHz \rightarrow 8kHz}$ = 40 ms. Probably, the response time t_{off} could be reduced further by using an amplifier which can generate higher amplitudes in the frequency domain f > 6 kHz. Nevertheless, the response time for the reappearance of a high transmission is reduced by one third, due to the use of a dual frequency addressing scheme with two successively applied frequencies even in the current experiments.

The attenuation spectra of the fiber are recorded by cutting back (Fig. 36). The fiber has relatively broad transmission windows. This causes problems during the measurements. The contrast ratio of the spectra is only in the 2 dB/cm range for cutting lengths of several cm. The spectra in the visible spectral region are simulated and a more detailed discussion is given in the section 'Liquid crystal-filled photonic crystal fibers with uniform director field'. A cut-back analysis in the infrared spectral region shows a broad transmission window from 900 to 1200 nm. The measurement indicates attenuations below 1 dB/cm. The main interest of the experiments in the current work is in the visible spectral region. This very promising finding of low attenuations in the infrared spectral region needs to be veryfied by further experiments with coherent radiation or alternatively with an optical chopper system. On/off switching effects and polarizing features were also observed by the current (rather simple) infrared spectral analysis.

[16] LiqCryst 4.7, reported for f = 100 Hz

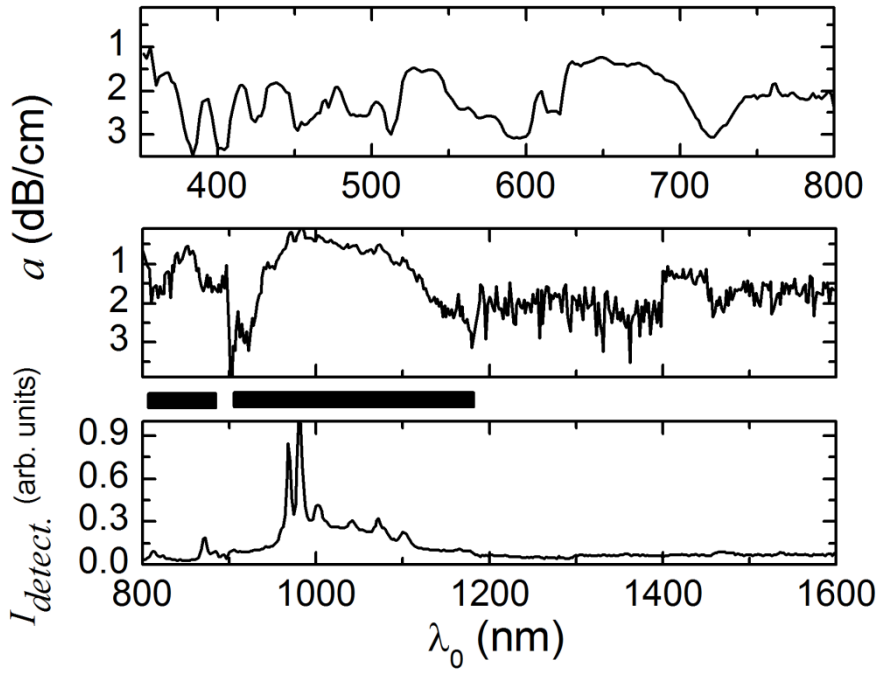

Fig. 36. Fiber LMA-10, planar anchoring, filled with ZLI 2461.Preliminary attenuation spectrum in the visible spectral region (upper spectrum) and preliminary attenuation spectrum in the infrared spectral region (middle spectrum). The lower spectrum is one of the infrared spectra recorded during the cut-back experiment. The black bars show regions with possibly lower damping in the infrared spectral region. The sharp peaks in the lower spectrum origin from the fiber coupled light source rather than from the attenuation properties of the filled fiber.

In another dual frequency addressing experiment, an experimental photonic crystal fiber[17] is filled with ZLI 2461. The fiber is shown in Fig. 37. Similar to the fibers LMA-8 and LMA-10, the experimental fiber is drawn from fused silica and exhibits a solid core surrounded by a two dimensional hexagonal lattice of air holes (core diameter 11.3 μm, hole diameter d = 5.4 μm, spacing Λ = 6.7 μm). The bare fiber shows (like conventional optical fibers) a continuous transmission in the spectral region, where fused silica is transparent. Light coupled into the core-region can be expected to be guided, because the average effective refractive index of the holey cladding is lower than the refractive index of the core. In contrast to the homogeneous LMA fibers, only the inclusions of the first ring which is nearest to the core have constant inclusion radii. The second ring of inclusions has slightly varying inclusion radii and in the third and forth ring, the radii of the inclusions are varied systematically. The fiber is treated with glymo and filled with ZLI 2461.

[17] provided by the fiber optics devision of the IPHT Jena

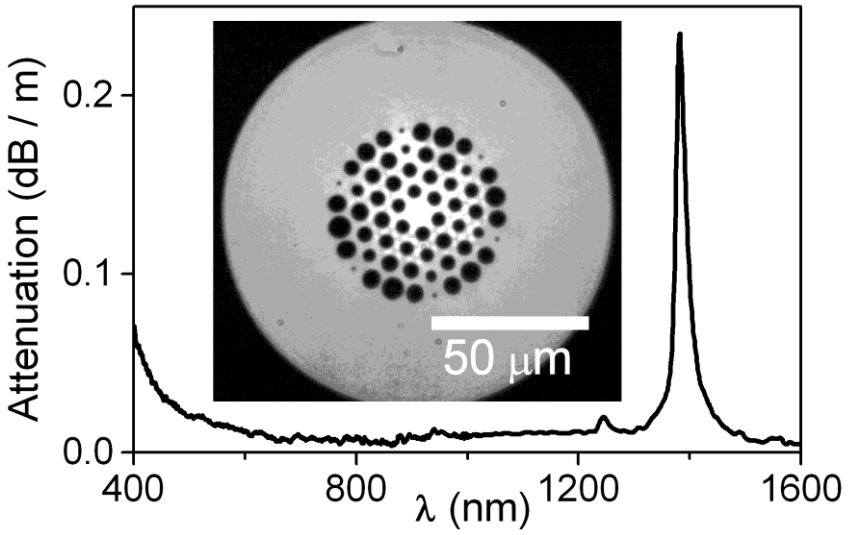

Fig. 37. Profile of an experimental photonic crystal fiber (microscope picture, 100x lens) and attenuation spectrum of the fiber in the unfilled state (spectrum by courtesy of the IPHT-Jena).

A 20 mm long piece of the fiber is investigated in the addressing experiments. White light is coupled into the fiber core. The end of the fiber is observed. In the field-off state, the sample shows reasonable transmission. Very interestingly, the transmission is enhanced by external fields with $f > f_c$. Some selected switching possibilities are discussed corresponding to voltages of 380 V_{rms} (Fig. 38a). i) the transmission is actively enhanced by switching from the no-voltage state to a 10 kHz a. c. signal. The response time is $t_{enh,1}$ = 20 ms. ii) When switching off this signal, the transmission passively decreases again with a time constant $t_{dec,1} \approx 80$ ms. iii) Switching on a 1 kHz a. c. signal reduces the transmission relatively fast, t_{on} = 15 ms. IV) When switching off the 1 kHz field, the transmission is initially reduced and grows again, slowly ($t_{off} > 160$ ms). This reappearance of the transmission can be fastened using an a. c. field of high frequency, which obviously enforces the director field to realign to a state of enhanced transmission. This switching behavior is demonstrated by a classical dual frequency [61] addressing scheme (Fig. 38b). A 10 kHz a. c. signal (380 V_{rms}) is permanently applied and eventually a 1 kHz a. c. signal is added. A smaller time constant ($t_{dual,rise} \approx 70$ ms) is achieved for the rise of the detected intensity. The switching speed of the (low frequency field-induced) decay of the detected intensity is reduced. This classical DFA driving scheme, where the high frequency is permanently applied to stabilize

one particular state of the liquid crystal cell, demonstrates the typical switching behavior of DFA liquid crystals. In the presented fiber optical switch, the switching contrast is enhanced and response times for the decay and rise of the detected intensity are matched. The sum $(t_{on} + t_{off})$ is reduced at the same time.

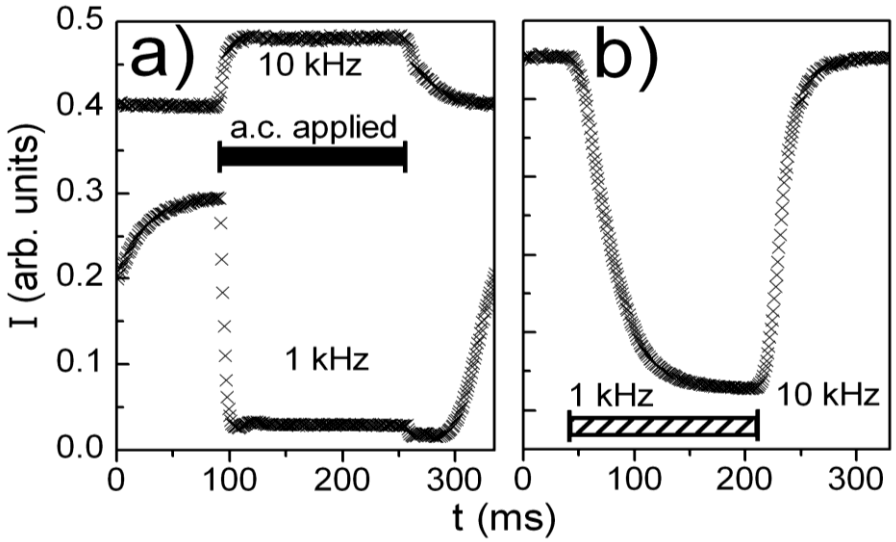

Fig. 38. Experimental fiber with planar anchoring and filled with ZLI 2461. White light is coupled to the fiber and the output intensity is detected.

In addition to changes of the total intensity, these fiber optical switches exhibit also polarizing capabilities comparable to those of the homogeneous fibers. When coupling white light to a fiber sample, optical near field analysis at the fiber end-face reveals a sudden decay of the detected *y*-polarized light when 1 kHz a. c. fields above a threshold voltage (≈ 140 V) are applied. The x-polarized part of the intensity gradually decreases with increasing voltage in these fibers (Fig. 39). The color of the output light changes from white (field-off state) to red (240 V_{rms}) and then to green (290 V_{rms}) because the fibers have a windowed transmission. At 240 V_{rms}, the contrast of *x*- and *y*-polarized light is ≈ 8 dB. It should be noticed that the response is apparently polarization independent if a signal above the critical frequency is applied.

Summarizing, this device could be applied as an electrical addressable fiber-optical polarizer with well adjustable wavelengths, as an intensity modulator or as a color filter.

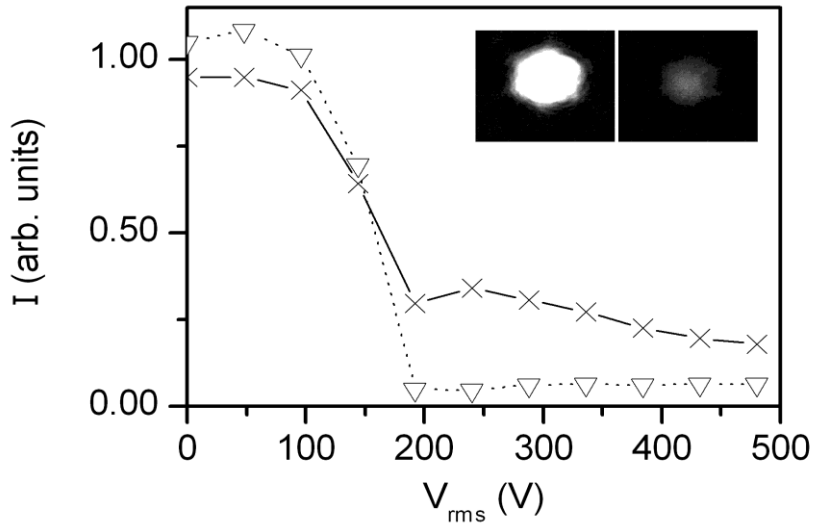

Fig. 39. Experimental fiber with planar anchoring, filled with ZLI 2461: detected white light intensity versus voltage, recorded by using a linear polarizer in *x*-direction: × and *y*-direction: ∇). The insets show near field pictures at 240 V_{rms} also recorded by using a linear polarizer in *x*- and *y*-direction.

3.5.5 Applying fields with a four electrode setup

A four electrode setup for a photonic crystal fiber filled with E7 was reported in the literature [25]. This setup was fabricated by using silicon based technology. Unpolarized infrared light from a broadband light source was coupled to the device in these reported experiments. In the field-on state, the transmission of linear polarized light could be switched between three different angles of the polarization direction.

The four electrode setup used in this work utilizes two plane ITO-electrodes and two wire electrodes (Fig. 24b Fig. 25b). Fiber LMA-8 shows a remarkable polarized response for the transmission of red light if filled with the liquid crystal MLC 6815. The fiber is treated with glymo in order to induce planar anchoring of the liquid crystal. The nematic mixture MLC 6815 form Merck is a liquid crystal with a low birefringence [18] . However, the average refractive index $\bar{n} = \sqrt{\frac{n_e^{\,2} + 2n_o^{\,2}}{3}}$ of MLC 6815 at room temperature is higher than the refractive index of fused silica. The attenuation spectrum Fig. 40 of the sample reveals broad transmission windows with attenuations even lower than 1 dB/cm.

[18] MLC 6815 Δn_d=0.088, $T_{CR\text{-}N} < 20$ °C, $T_{N\text{-}I}$ = 67 °C [LiqCryst 4.7], $n_{e,d}$ = 1.5191 and $n_{o,d}$ = 1.4674 [index d: 589 nm (sodium d-line), Merck data sheet].

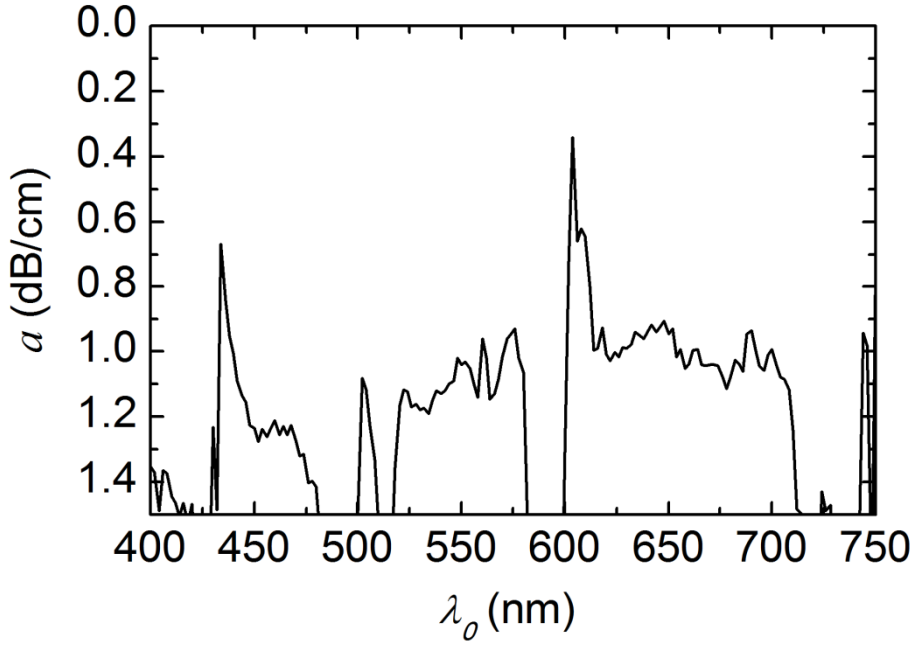

Fig. 40. Attenuation spectrum of fiber LMA-8 with planar anchoring, and filled with MLC 6815.

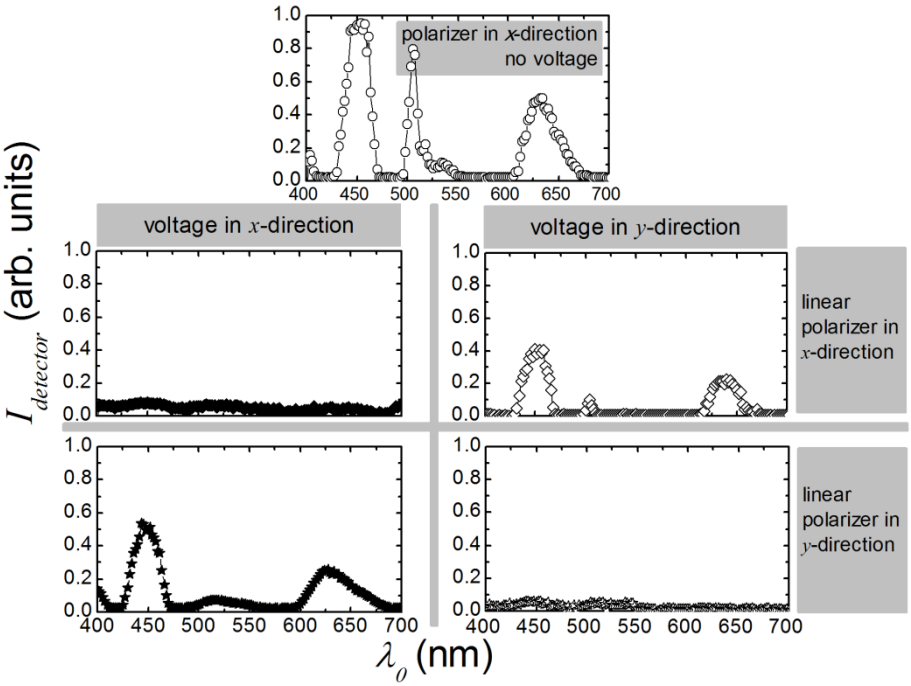

Fig. 41. Polarized response of fiber LMA-8 with planar anchoring, and filled with MLC 6815. Intensity spectra recorded by observing the fiber end with a microscope lens with linear polarizer and a PMT as detector. The upper spectrum shows the detected intensity in the no-voltage state. The four lower spectra show the intensity recorded when applying a 500 V_{rms} a. c. signal.

A strong polarizing effect occurs in the transmission windows form $\lambda_0 = 430$ to 480 nm and from $\lambda_0 =$ 600 to 710 nm when high electric fields are applied. In these two spectral regions, 25 % of the initial intensity are detected when applying a 500 V_{rms} a. c. signal. At the same time, the transmission decays strongly independent of the state of polarization in the spectral region from $\lambda_0 = 500$ to 550 nm. The four electrode setup (Fig. 24, Fig. 25) is used to demonstrate the selective transmission of linear polarized light in this fiber for two perpendicular states of polarization (Fig. 41). In this experiment, the monochromatic light source is adjusted to a wavelength of 632 nm (2 nm bandwidth). Electric fields are applied in the *x*-direction by using the wire electrodes. If so, the detector signal for *x*-polarized light disappears. At the same time, a high transmission for *y*-polarized light is observed by turning the polarizer 90°. By using the ITO-electrodes, electric fields are applied in the *y*-direction. In this case, the detector signal for *y*-polarized light disappears and high transmission occurs selectively for *x*-polarized light. In the transmission windows with polarized response, the light which is polarized parallel to the electric field lines of the addressing field is strongly dampened. The transmission of *x*- and *y*-polarized light can be chosen by using either the ITO-electrodes or the wire electrodes.

The two perpendicular sets of electrodes were used for bipolar addressing in the current experiments. In the ideal case, the direction of the (in first approximation) linear electric fields could be rotated arbitrarily in the plane of the fiber profile. Some approaches for such a tilted angle addressing were conducted in the current experiments. The electric field can be expected to point in the 45°-direction for example by connecting one wire electrode and one ITO-electrode together to the same pole of the amplifier and by then connecting the other two electrodes together to the second pole of the amplifier. In this experiment almost no intensity is detected if a 500 V_{rms} signal is applied. This is an interesting polarization independent effect which is surely caused by some imperfections of the setup. These imperfections can be utilized here quite pleasantly to generate a polarization independent effect. The ITO-electrodes provide a constant addressing field over the whole section of the fiber which is covered by the upper electrode (Fig. 24) because both electrodes touch the surface of the fiber. The addressing field which is caused by the wire electrodes varies at least slightly over the fiber length. The exact position of the

wires can be already controlled very precisely in the current manufacturing process at the fiber ends. Currently, it cannot be guaranteed that the wires are perfectly aligned parallel to the fiber over the whole length. The deviations are in the order of 10 μm. In tilted angle driving, the direction of the resulting electric field varies over the fiber length. Accordingly, a complete decay of the transmission occurs if using the wire electrodes and the ITO-electrodes simultaneously. If using solely the wire electrodes, the imperfections of the wire alignment are not troublesome at all.

The response times of the addressing experiments are measured by using the ITO-electrodes. If the a. c. signal (1 kHz) is switched on, the detected intensity decays (Fig. 42). The time constant t_{on} of this decay decreases with increasing voltage down to values < 10 ms. As for the E7 filled fibers with planar anchoring, the response for *x*-polarized light is two stepped. Once the initial decay is complete, the transmission of *x*-polarized light increases again. This rise of the detected optical power of *x*-polarized light has a time constant $t_{on,1}$ comparable to the decay time constant t_{on}. $t_{on,1}$ decreases with increasing voltage, too. However, the time constant $t_{on,1}$ seems to be heightened again at very high voltages. In contrast, the response time $t_{off} = (10.3 \pm 1.2)$ ms is apparently independent of the addressing voltage and the state of polarization. Altogether, the optical switch has an optimum driving voltage of ≈ 550 V_{rms}. The on/off-switching cycle for *y*-polarized light can be faster than 20 ms. Probably, this is also valid for the polarization independent effect observed for addressing with all four electrodes. However, the polarizing effect at this voltage also develops within 20 ms. The polarization extinction ratio $(PER = \lg\left(\frac{I_{x-polarized}}{I_{y-polarized}}\right))$ of this effect is for a 15 mm long fiber already very well above 10 [which is the figure of merit (FOM) for technical applications, Fig. 43].

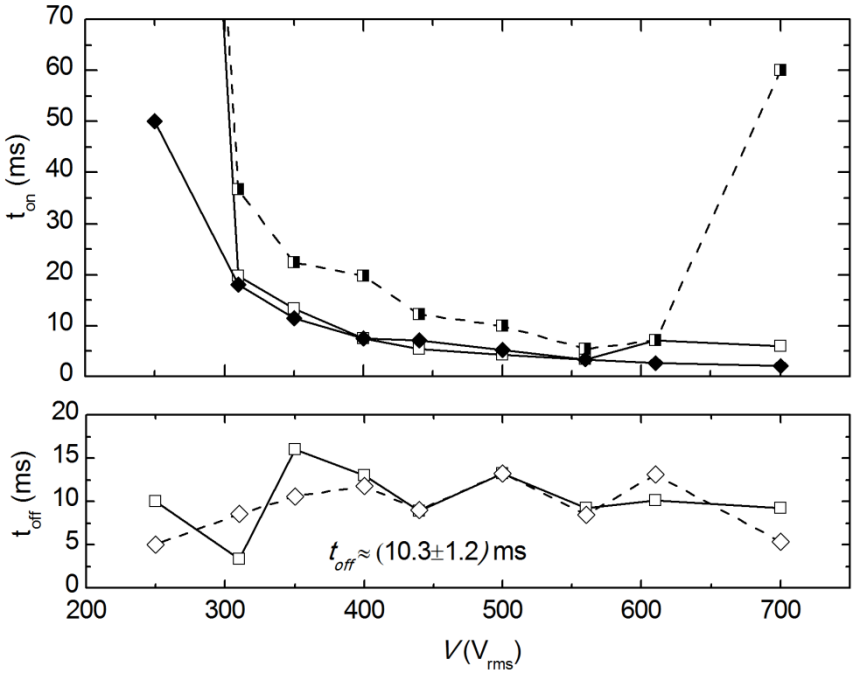

Fig. 42. Fiber LMA-8 filled with MLC 6815, planar anchoring. Response times of *x*-polarized light (squares) and *y*-polarized light (diamonds). Upper diagram: If the a. c. signal (1 kHz) is switched on, the transmission decays (open squares, filled diamonds). The response for *x*-polarized light is two stepped. Once the decay is complete, the transmission of *x*-polarized light increases again (half filled squares). Lower diagram: the response time t_{off} =(10.3±1.2) ms is apparently independent of the addressing voltage.

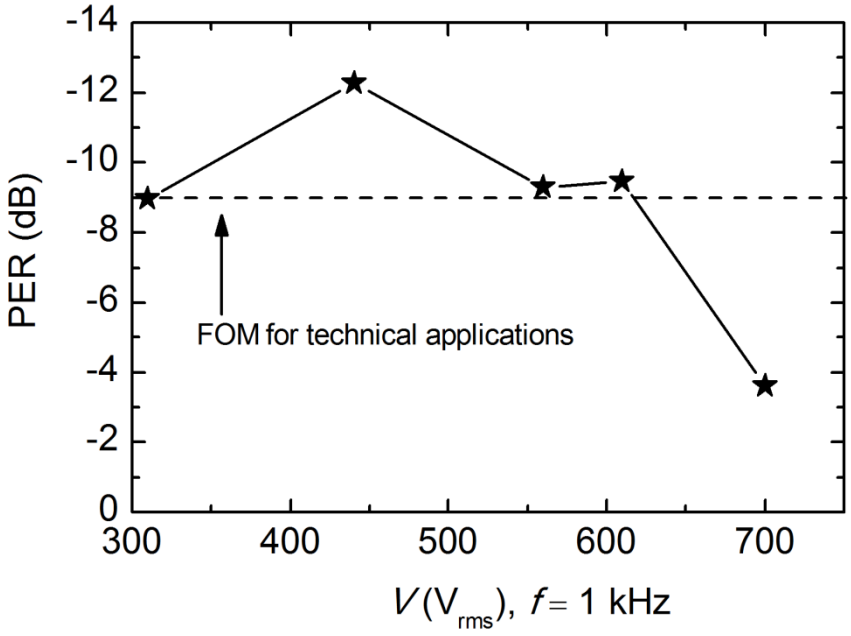

Fig. 43. Fiber LMA-8 filled with MLC 6815 (planar anchoring). Polarization extinction ratio vs. applied voltage.

4. Theoretical Analysis (Simulation)

4.1 Motivation and short introduction

The experiments show that the combination of fibers with varying fiber parameters and different liquid crystals and anchoring conditions leads to very useful variations of the transmission properties. As shown in the introduction, the birefringence of filled capillaries cannot be described by trivial terms in numerous cases. Electromagnetic field simulations are performed to gain a deeper understanding of the waveguiding properties. The commercially available finite element method simulation suite COMSOL Multiphysics® [62] (in the following COMSOL) is applied to develop a model considering the fiber geometry, the birefringence of the liquid crystal, the extraordinary high dispersion of liquid crystals and the damping that occurs in liquid crystals typically to a large extent.

In this part, a theoretical approach for the calculation of attenuation spectra is presented in accordance to the experimental observation of the attenuation properties of these fibers. The attenuation properties of photonic crystal fibers with high index isotropic [10,11,12,13] and anisotropic inclusions [26,36] in a background material with lower refractive index have been extensively studied in the literature. In these numerical studies, it was shown that the main source of loss can very well be the leaky confinement due to resonances of the inclusions (confinement loss). The confinement loss is commonly evaluated by considering some kind of attenuating boundary conditions at the outer boundaries of the area of calculation in simulations. Modes where the fields reach the outer boundary at least partially are in this case burdened with an imaginary part of the modal effective refractive index. Essentially, the electric and magnetic fields are directly dampened in this type of simulation. In spite of these established studies, systematic variations of the fiber parameters and precise comparison between theoretical and experimental results are necessary, especially for liquid crystal-filled fibers.

The scattering cross section of liquid crystals is extraordinary high compared to isotropic liquids. This has maybe prevented liquid crystals from the application in elongated waveguides before the invention of photonic crystal fibers. Nevertheless, there have been extensive studies in this field in the 1970s [14]. In liquid crystal

fibers with modes which are highly confined in a core surrounded by liquid crystal-filled inclusions, high losses might be caused mainly by scattering due to the liquid crystal. The question arises, whether complicated boundary conditions beyond the liquid crystal-filled inclusions are necessary at all. I.e. the scattering coefficient of the liquid crystals could be considered in the simulations directly as imaginary part of the epsilon tensor. The solutions would yield the effective refractive index as imaginary number that describes the loss (Eq. 21). Unfortunately, the corresponding formulation of the partial differential equations is even more complicated than in the lossless case with a real epsilon tensor. Thus, the computation time would be higher. But the losses can as well be calculated from the fields in the ideal lossless case by calculating perturbations ([63], power loss approach). The field pictures for an ideal lossless structure are searched and the loss is then calculated by the absorption properties of the materials. This two stepped simulation technique is preferable because short simulation times and eventually high spatial resolutions are enabled.

COMSOL allows a field simulation with a three dimensional epsilon tensor in a two dimensional geometry:

$$\varepsilon_r = \begin{pmatrix} \varepsilon_{xx}(x,y,z) & \varepsilon_{xy}(x,y,z) & 0 \\ \varepsilon_{yx}(x,y,z) & \varepsilon_{yy}(x,y,z) & 0 \\ 0 & 0 & \varepsilon_{zz}(x,y,z) \end{pmatrix}. \qquad \text{(Eq. 68)}$$

These components of the epsilon tensor ε_r can be programmed dependent on the spatial coordinates. The director fields expected to appear in the liquid crystal-filled inclusions can thus be integrated in the simulations. No complicated boundary conditions like perfectly matched layers or related boundary conditions are applied. Instead, the high scattering caused by the liquid crystal inclusion is used to analyze the attenuation properties of the core modes. The field pictures are simulated for the ideal lossless structure and exclusively modes with more than 75% of the time average power flow residing in the core section are expected to contribute to the propagation in the waveguide. The attenuation spectra are then calculated with the power loss method.

4.2 Test of the Model; Analysis of a real fiber filled with the well-known liquid crystal mixture E7

The simulations for fiber LMA-8 with planar anchoring, filled with E7 are compared to experimental results in order to show the high accuracy of the current simulations.

The epsilon tensor inside the inclusions is approximated as uniaxial with the optical axis in propagation direction:

$$\varepsilon_r = \begin{pmatrix} n_o^2 & 0 & 0 \\ 0 & n_o^2 & 0 \\ 0 & 0 & n_e^2 \end{pmatrix}. \qquad \text{(Eq. 69)}$$

Compared to glasses, liquid crystals have a very high dispersion. Accurate spectra are obtained by considering the dispersion $n(\lambda_0)$ of all the materials. The dispersion is empirically described by a three parameter Cauchy equation:

$$n(\lambda_0) = A + B\lambda_0^{-2} + C\lambda_0^{-4}. \qquad \text{(Eq. 70)}$$

For the silica glass, Cauchy parameters are used which were obtained by a fit to data for Heraeus suprasil glas[19,20]. Nematic liquid crystals are birefringent. The dispersion of the two refractive indices $n_o(\lambda_0), n_e(\lambda_0)$ has to be considered in the liquid crystal-filled inclusions. The Cauchy parameters for the liquid crystal mixture E7 are well-known in the literature at least in the visible and NIR spectral range. The dispersion of nematic liquid crystals can be measured using an advanced Jelly microrefractometer, for example (see Apendix). Cauchy parameters reported in the literature [64] were used for this simulation. By including the dispersion, the current simulations are suited to describe real fibers which are filled with existing liquid crystals.

The attenuation spectrum is simulated (Fig. 44) with the geometry parameters $R_i = 1.2\ \mu$m and $p = 5.5\ \mu$m of the fiber LMA-8. As expected, the simulated spectra show the distinct transmission windows seen in the experiments. Although the shape of the attenuation spectra observed in the simulations and the experiments are in good agreement, the calculated attenuation is lower than the measured values. For

[19] The dispersion of glasses is usually understood by the Sellmeier model. The empirical Cauchy model is used in this simulation according to the accuracy of the data for the liquid crystals, where experimental results are fitted with the Cauchy formula.

[20] n_C = 1.45637 at 656.3 nm; n_d = 1.45846 at 587.6 nm; n_F = 1,46313 at 486,1 nm; n_g = 1.46669 at 435.8 nm; n_{248} = 1.50855 at 248 nm; $A_{suprasil}$ = 1.44855; $B_{suprasil}$ = 0.00334 μm^2; $C_{suprasil}$ = 2.14528·10^{-5} μm^4.

example, the minimum experimental attenuation $a_{\exp}(\min) \approx$ 2.5 dB/cm at $\lambda_0 \approx$ 450 nm and $\lambda_0 \approx$ 415 nm is higher than the simulated value of $a_{sim}(\min) \approx$ 0.4 dB/cm. Nevertheless, the simulated spectra fit the experimental data (Fig. 44). The *y*-axes of the two spectra in Fig. 44 are scaled to an equal dynamic range of 4 dB/cm. The experimental attenuation is higher than the theoretically expected values, maybe because of a partially inhomogeneous orientation of the liquid crystal in the capillaries. Nevertheless, the attenuation maxima and the position of the spectral regions with low attenuation are reproduced by the simulation. In both spectra, there are two broad transmission windows at $\lambda_0 \approx$ 450 nm and 415 nm, which have the lowest attenuation. In the simulations, these two transmission windows are followed by a small and narrow peak at $\lambda_0 \approx$ 480 nm. This peak may very well accord the shoulder seen in the experimental spectrum. From $\lambda_0 \approx$ 510 nm to $\lambda_0 \approx$ 590 nm there is a region with low attenuation seen in the experimental spectrum and the simulated spectrum. In the simulation, 4 peaks occur in this spectral region. Only 2 peaks are seen in the experiment. These two peaks are clearly divided by an attenuation maximum at $\lambda_0 \approx$ 550 nm which is also seen in the simulated spectra. At $\lambda_0 \approx$ 600 nm, an attenuation maximum occurs in the experimental and the simulated spectra. The experimental data is noisy in the spectral region $\lambda_0 >$ 700 nm[21]. However, a decay of the attenuation is seen at $\lambda_0 \approx$ 670 nm which may very well be the edge of the transmission window seen in the simulation at $\lambda_0 \approx$ 670 to 750 nm.

[21] Especially for the long pieces of the waveguide, the transmitted intensity is reduced to values at the experimental detection limit. The quantum efficiency of the PMT-tube is significantly lower here than at lower wavelength.

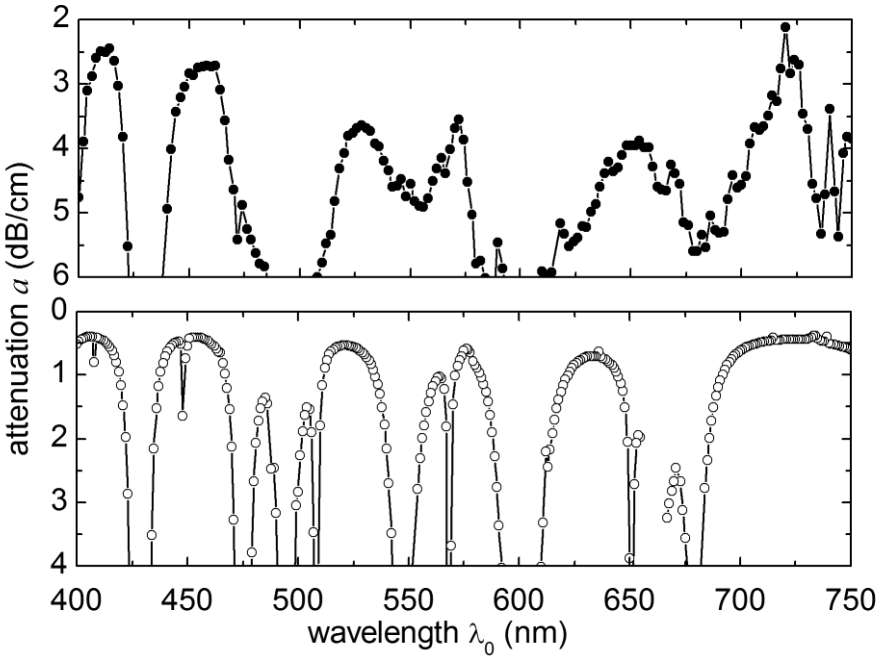

Fig. 44. Attenuation spectra of the fiber LMA8 filled with E7, planar anchoring (closed symbols: measured attenuation, open symbols: simulated attenuation).

4.2.1 Comparing the results to the ARROW model

Sun et al. [33] simulated one theoretical fiber with isotropic and anisotropic liquid crystal inclusions, respectively. They showed that the transmission spectrum of the isotropic fiber is modified and additional transmission minima occur for cylindrical uniaxial liquid crystal inclusions with the optical axis in propagation direction. They applied the ARROW-model of Litchinitser et al. to describe fibers with such uniaxial high index inclusions. Sun et al. calculated the attenuation minima for their theoretical fiber by using two formulas (Eq. 71, Eq. 72) for the resonances of all modes of interest.

$$\lambda_{\min,o} = \frac{4R_i\sqrt{n_o^2 - n_{glass}^2}}{m + 1/2},\ m \in \boldsymbol{N}. \qquad \text{(Eq. 71)}$$

$$\lambda_{\min,e} = \frac{n_e}{n_o}\frac{4R_i\sqrt{n_o^2 - n_{glass}^2}}{m + 1/2},\ m \in \boldsymbol{N}. \qquad \text{(Eq. 72)}$$

The simulations of Sun et al. were repeated by using the current simulation technique. In Fig. 45 these transmission minima $\lambda_{\min,o}$ and $\lambda_{\min,e}$ are indicated as diamonds and stars, respectively. The upper spectrum corresponds to the theoretical fiber and the theoretical liquid crystal simulated by Sun et al. In this case, every resonance attends one transmission minimum and all the transmission minima are found. The lower attenuation spectrum corresponds to the current simulation of the LMA-8 fiber filled with E7. This simulated spectrum fits the experimental data very well. The extended ARROW-model of Sun et al. is again applied to find the transmission minima $\lambda_{\min,o}$ and $\lambda_{\min,e}$ but this time considering the dispersion $n_{o,E7}(\lambda_0), n_{e,E7}(\lambda_0)$, and $n_{silica}(\lambda_0)$. The dispersion is again described with the Chauchy model. In the lower spectrum, not every transmission minimum is attended with a star or a diamond. Attenuation minima are found by the current simulation which are not described by the analytical approximations (Eq. 71, Eq. 72).

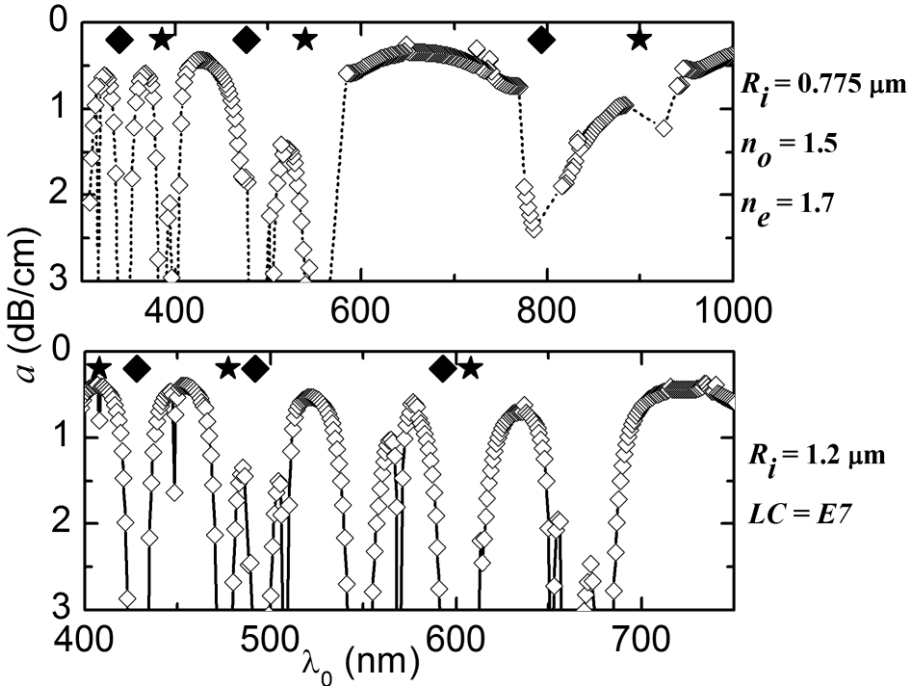

Fig. 45. Comparison of analytical results (filled symbols) and simulation results (open symbols) for two different fibers with planar anchoring. The filled diamonds indicate the attenuation maxima calculated using n_o. The filled stars correspond to the attenuation maxima calculated also using n_e. Upper spectrum: Simulated attenuation spectrum of a fiber proposed by Sun et al. [33] with constant refractive indices. Lower spectrum (x-axis scaled differently): Simulated attenuation spectrum of fiber LMA-8 with the liquid crystal E7 under planar anchoring. Now the simulation includes the dispersion of the refractive indices.

The question arises, weather the analytical model should be extended maybe by an even more detailed analysis of the rod modes. Although such an analysis would be very interesting, the simulation shows that not every resonance necessarily causes an extraordinary high loss of the core mode of the photonic crystal fiber. For example, at $\lambda_0 = 410$ nm there is a resonance seen in the analytical model and in the simulation which causes only a small rise of the attenuation in the simulation. Moreover, this particular decay of the transmission is not seen in the experimental spectra at all. In the simulated spectra, a sharp decay of the transmission is seen at $\lambda_0 \approx 568$ nm which is not attended by a star or a diamond. The simulated modal intensity distribution in this spectral region (calculated from the undisturbed fields) is shown in Fig. 46. An inclusion mode which crosses $n_{silica}(\lambda_0)$ at $\lambda_0 \approx 565$ nm (where $n_{incl.} = n_{silica} = 1.4592$) is in strong interaction with the core mode ($n_{eff,core} = 1.4585$) and causes a strong decrease of the transmission. The simulation describes the interaction of the core mode and the inclusion modes very well.

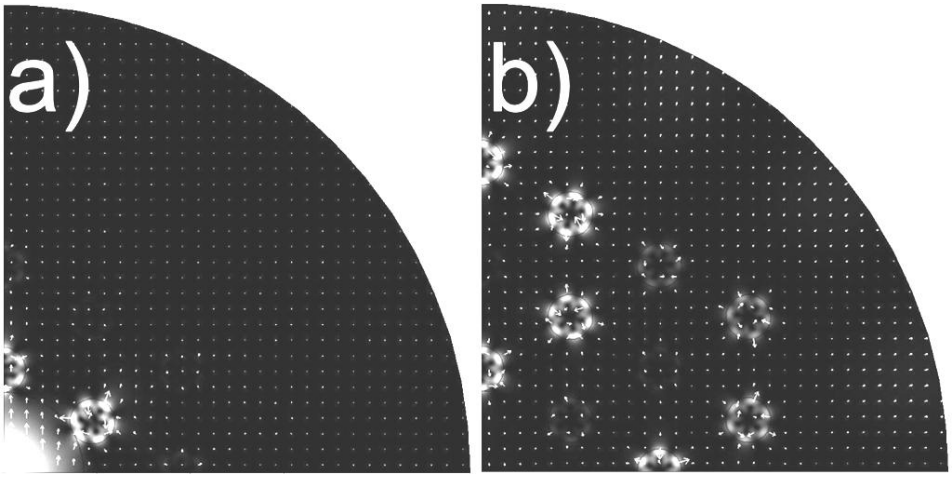

Fig. 46. Simulated core a) and cladding modes b) (fiber LMA8 filled with E7, planar anchoring). a) $\lambda_0 = 568$ nm, $n_{eff,core} = 1.4585$, $a \approx 8$ dB/cm. b) $\lambda_0 = 565$ nm, $n_{eff,incl} = 1.4593$, $a \approx 17$ dB/cm.

Although a one dimensional Bragg stack is not an adequate model for a complete photonic bandgap at small angles of incidence, the characteristic dispersion curve $D(\lambda_0)$ (Eq. 49) of bandgap guiding fibers can be understood by a straight forward analytical analysis of light which is reflected by a one dimensional

Bragg stack at glancing angles [65]. D is negative at the short wavelength edge and increases with increasing wavelength. $D(\lambda_0)$ has an inflexion point near $D = 0$ roughly at the center of a bandgap. A typical curve without numerical deviations is shown in the region $\lambda_0 = 550$ nm to 590 nm (Fig. 47). The dispersion curves can help to identify the single bandgaps. Apparently, the individual transmission windows seem to consist of one photonic bandgap respectively from this point of view. The chromatic dispersion curves show a satisfactory progression whereas there are still some individual points appearing which is due to the simple algorithm used to estimate $D(\lambda_0)$ from $n_{eff}(\lambda_0)$ where the slope of $n_{eff}(\lambda_0)$ is estimated using only the first neighbors of a point. The chromatic dispersion curves are rather smooth in all of the bandgaps but in the one from $\lambda_0 = 550$ nm to 590 nm. The indicated deviations around $\lambda_0 \approx 630$ nm and in the bandgap at $\lambda_0 = 720$ nm are due to parasitic simulation modes. Neglecting these deviations, the zero dispersion wavelengths provided in the respective transmission windows could be potentially accessed experimentally.

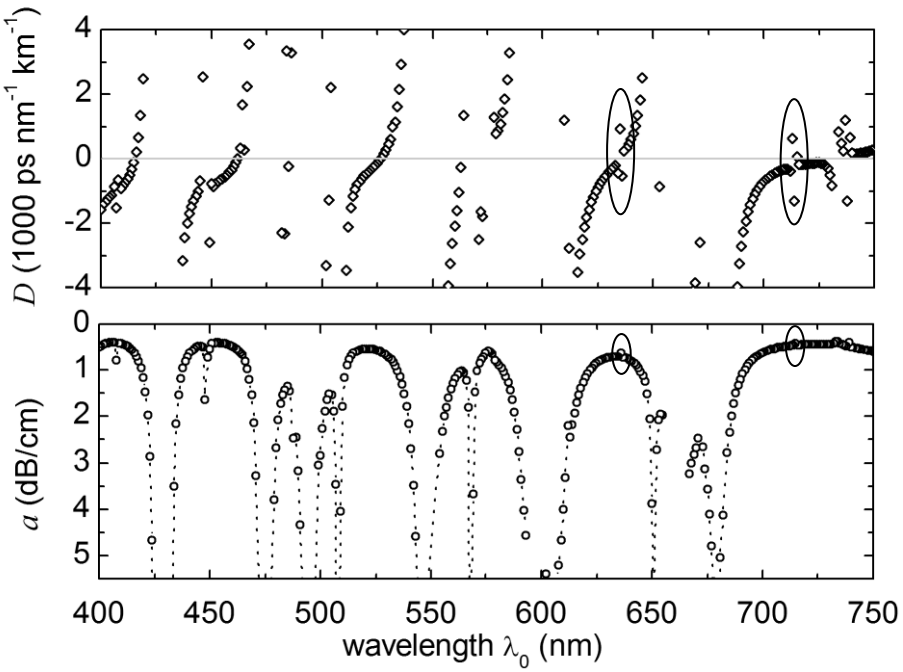

Fig. 47. Simulated chromatic dispersion D (diamonds) and simulated attenuation (rings) of fiber LMA8 filled with E7, planar anchoring. Selected artifacts are indicated by ellipses.

4.3 Details of the Model

The theoretical model is intended to give additional insight into the experimentally observed attenuation characteristics of liquid crystal-filled photonic crystal fibers. The fibers have a two-dimensional micro-structure which is invariant in the propagation direction. According to the experimental results, the modes with low attenuation are expected to be highly confined in the fiber core. Existing theoretical investigations on photonic crystal fibers with high index inclusions describe the guiding mechanism as band gap guiding caused by anti resonant scattering at the inclusions. The liquid crystal-filled sections of the current fibers may be characterized as cylindrical birefringent high index liquid crystal inclusions. Detailed theoretical investigations on low-loss waveguides with liquid crystal inclusions are still necessary. Especially the influences of the high dispersion and of the high scattering cross section of liquid crystals need to be investigated. Accordingly, a model is created with the FEM-simulation suite 'COMSOL Multiphysics®' (in the following COMSOL). The COMSOL-RF-module which consists of tools tailored for simulations in the field of optics and photonics is chosen to conduct electromagnetic field simulations. COMSOL is very well suited to describe numerous of the required influence parameters. The geometry of the fiber can be modeled with the favorable resolution of the finite element method (triangular mesh). The details of the COMSOL finite element formulation, solvers and required user-adjustments are explained in the user guide of COMSOL and the COMSOL-RF module [66].

The current simulations are carried out in the application mode "Perpendicular Hybrid-Mode Waves". An application mode in COMSOL is the specification of the equations and the set of dependent variables (which the equations are solved for). Moreover, the simulation attributes are specially adapted according to the application mode setting in terms of the graphical user interface and the COMSOL programming language at the MATLAB® command line. The simulated waveguides shall have a two-dimensional symmetry invariant in the direction of the propagation (*z*-direction). Thus, the propagating modes have a propagation constant in z-direction. This situation is treated in the perpendicular application mode. Here, the waves propagate perpendicular to a two-dimensional cross section of a waveguide. Additionally, inhomogeneous materials need to be considered due to the

birefringence of the liquid crystal. The "Perpendicular Hybrid-Mode Waves"-application mode fulfils these two preconditions. It treats the case of transversal fields and inhomogeneous materials. Two possible formulations of the partial differential equations are available in this application mode. Either, two equations for the two transversal field components are solved, or a set of three equations for all three field components. Birefringence can be included into the simulations by a 3-by-3 epsilon-tensor ε_{PHM} occupied by 5 elements. This is a very instructive way to decouple the *z*-dependences of the problem form the *x*- and *y*-dependences.:

$$\varepsilon_{PHM} = \begin{pmatrix} \varepsilon_{xx} & \varepsilon_{xy} & 0 \\ \varepsilon_{yx} & \varepsilon_{xx} & 0 \\ 0 & 0 & \varepsilon_{zz} \end{pmatrix}. \qquad \text{(Eq. 73)}$$

Ansatz functions where the *z*-dependence of the fields is expressed by an exponential can be used in analogy to the analytical model of a cylindrical fiber where the *z*-dependence is separated from the *r*- and φ-dependences (Eq. 40):

$$\vec{H}_{PHM} = \vec{H}(x,y)e^{\lambda z} = \begin{pmatrix} H_x(x,y)e^{j\beta z} \\ H_y(x,y)e^{j\beta z} \\ H_z(x,y)e^{j\beta z} \end{pmatrix} = \begin{pmatrix} \breve{H}_x \\ \breve{H}_y \\ \breve{H}_z \end{pmatrix}. \qquad \text{(Eq. 74)}$$

Consider the two dimensional tensors ε_t:

$$\varepsilon_t = \begin{pmatrix} \varepsilon_{xx} & \varepsilon_{xy} \\ \varepsilon_{yx} & \varepsilon_{xx} \end{pmatrix}, \qquad \text{(Eq. 75)}$$

The determinant of ε_t is then:

$$\det \varepsilon_t = \varepsilon_{xx}\varepsilon_{yy} - \varepsilon_{xy}\varepsilon_{yx}. \qquad \text{(Eq. 76)}$$

The inverse of ε_{PHM} can be written as:

$$\varepsilon_{PHM}^{-1} = \frac{1}{\det(\varepsilon_t)} \begin{pmatrix} \varepsilon_{yy} & -\varepsilon_{xy} & 0 \\ -\varepsilon_{yx} & \varepsilon_{xx} & 0 \\ 0 & 0 & \dfrac{\det(\varepsilon_t)}{\varepsilon_{zz}} \end{pmatrix} \qquad \text{(Eq. 77)}$$

The second curl term in the wave equation for the magnetic field (Eq. 14 is replaced by using ∇_{t3D} and a vector $\vec{Z}$. The left side splits up in two summands:

$$\begin{aligned}
&\nabla\times\left(\varepsilon_{PHM}^{-1}\nabla\times\vec{H}\right)=k_0{}^2\vec{H}_{PHM}\\
&\Leftrightarrow\nabla\times\left(\varepsilon_{PHM}^{-1}\left(\nabla_{t3D}\times\vec{H}_{PHM}+\vec{Z}\right)\right)=k_0{}^2\vec{H}_{PHM}\\
&\Leftrightarrow\nabla\times\left(\varepsilon_{PHM}^{-1}\nabla_{t3D}\times\vec{H}_{PHM}+\varepsilon_{PHM}^{-1}\vec{Z}\right)=k_0{}^2\vec{H}_{PHM}\\
&\Leftrightarrow\nabla\times\varepsilon_{PHM}^{-1}\nabla_{t3D}\times\vec{H}_{PHM}+\nabla\times\varepsilon_{PHM}^{-1}\vec{Z}=k_0{}^2\vec{H}_{PHM},
\end{aligned}\qquad\text{(Eq. 78)}$$

$$\nabla\times\vec{H}_{PHM}=\begin{pmatrix}\frac{\partial}{\partial y}\breve{H}_z-\frac{\partial}{\partial z}\breve{H}_y\\ \frac{\partial}{\partial z}\breve{H}_x-\frac{\partial}{\partial x}\breve{H}_z\\ \frac{\partial}{\partial x}\breve{H}_y-\frac{\partial}{\partial y}\breve{H}_x\end{pmatrix}=\nabla_{t3D}\times\vec{H}_{PHM}+\vec{Z},\qquad\text{(Eq. 79)}$$

$$\nabla_{t3D}\times\vec{H}_{PHM}=\begin{pmatrix}\frac{\partial}{\partial y}\\ \frac{\partial}{\partial z}\\ 0\end{pmatrix}\times\begin{pmatrix}\breve{H}_x\\ \breve{H}_y\\ \breve{H}_z\end{pmatrix}=\begin{pmatrix}0\\ 0\\ \frac{\partial}{\partial x}\breve{H}_y-\frac{\partial}{\partial y}\breve{H}_x\end{pmatrix},\qquad\text{(Eq. 80)}$$

$$\vec{Z}=\begin{pmatrix}\frac{\partial}{\partial y}\breve{H}_z-\frac{\partial}{\partial z}\breve{H}_y\\ \frac{\partial}{\partial z}\breve{H}_x-\frac{\partial}{\partial x}\breve{H}_z\\ 0\end{pmatrix}=\begin{pmatrix}\frac{\partial}{\partial y}\breve{H}_z-j\beta\breve{H}_y\\ j\beta\breve{H}_x-\frac{\partial}{\partial x}\breve{H}_z\\ 0\end{pmatrix}.\qquad\text{(Eq. 81)}$$

With the above definitions, the matrix products of the inverse dielectric tensor ε_{PHM}^{-1} with $\nabla_{t3D}\times\vec{H}_{PHM}$ and $\vec{Z}$ yield:

$$\varepsilon_{PHM}^{-1}\nabla_{t3D}\times\vec{H}_{PHM}=\frac{1}{\det(\varepsilon_t)}\begin{pmatrix}0\\ 0\\ \frac{\partial}{\partial x}\breve{H}_y-\frac{\partial}{\partial y}\breve{H}_x\end{pmatrix}\frac{\det(\varepsilon_t)}{\varepsilon_{zz}}\qquad\text{(Eq. 82)}$$

$$\varepsilon_{PHM}^{-1}\vec{Z}=\frac{1}{\det(\varepsilon_t)}\begin{pmatrix}\varepsilon_{yy} & -\varepsilon_{xy} & 0\\ -\varepsilon_{yx} & \varepsilon_{xx} & 0\\ 0 & 0 & \dfrac{\det(\varepsilon_t)}{\varepsilon_{zz}}\end{pmatrix}\begin{pmatrix}\dfrac{\partial}{\partial y}\breve{H}_z - j\beta\breve{H}_y\\ j\beta\breve{H}_x - \dfrac{\partial}{\partial x}\breve{H}_z\\ 0\end{pmatrix}$$
$$=\frac{1}{\det(\varepsilon_t)}\begin{pmatrix}\varepsilon_{yy}\dfrac{\partial}{\partial y}\breve{H}_z - \varepsilon_{yy}j\beta\breve{H}_y - \varepsilon_{xy}j\beta\breve{H}_x + \varepsilon_{xy}\dfrac{\partial}{\partial x}\breve{H}_z\\ -\varepsilon_{yx}\dfrac{\partial}{\partial y}\breve{H}_z + \varepsilon_{yx}j\beta\breve{H}_y + \varepsilon_{xx}j\beta\breve{H}_x - \varepsilon_{xx}\dfrac{\partial}{\partial x}\breve{H}_z\\ 0\end{pmatrix} \quad \text{(Eq. 83)}$$

Taking the curl of Eq. 82 and 83 results:

$$\nabla\times\left(\varepsilon_{PHM}^{-1}\nabla_{t3D}\times\vec{H}_{PHM}\right)=\frac{1}{\varepsilon_{zz}}\begin{pmatrix}\dfrac{\partial}{\partial y}\left(\dfrac{\partial}{\partial x}\breve{H}_y-\dfrac{\partial}{\partial y}\breve{H}_x\right)\\ -\dfrac{\partial}{\partial x}\left(\dfrac{\partial}{\partial x}\breve{H}_y-\dfrac{\partial}{\partial y}\breve{H}_x\right)\\ 0\end{pmatrix}, \quad \text{(Eq. 84)}$$

$$\nabla\times\varepsilon_{PHM}^{-1}\vec{Z}=$$
$$\frac{1}{\det(\varepsilon_t)}\begin{pmatrix}\varepsilon_{xx}j\beta\dfrac{\partial}{\partial x}\breve{H}_z + j\beta\varepsilon_{yx}\dfrac{\partial}{\partial y}\breve{H}_z + \varepsilon_{xx}\beta^2\breve{H}_x + \varepsilon_{yx}\beta^2\breve{H}_y\\ \varepsilon_{yy}j\beta\dfrac{\partial}{\partial y}\breve{H}_z + \varepsilon_{yy}\beta^2\breve{H}_y + \varepsilon_{xy}\beta^2\breve{H}_x + \varepsilon_{xy}j\beta\dfrac{\partial}{\partial x}\breve{H}_z\\ Z_z'\end{pmatrix}. \quad \text{(Eq. 85)}$$

The z-component of this vector Z_z' is given separately in terms of a better readability:

$$Z_z' = j\beta\left(\frac{\partial}{\partial x}\left(\varepsilon_{yx}\breve{H}_y+\varepsilon_{xx}\breve{H}_x\right)+\frac{\partial}{\partial y}\left(\varepsilon_{yy}\breve{H}_y+\varepsilon_{xy}\breve{H}_x\right)\right)$$
$$-\left(\varepsilon_{yx}\frac{\partial^2}{\partial x\partial y}\breve{H}_z+\varepsilon_{xx}\frac{\partial^2}{\partial x^2}\breve{H}_z+\varepsilon_{yy}\frac{\partial^2}{\partial y^2}\breve{H}_z+\varepsilon_{xy}\frac{\partial^2}{\partial y\partial x}\breve{H}_z\right). \quad \text{(Eq. 86)}$$

The starting point of this formulation was the partial differential equation Eq. 78, an equation system of three equations (*x*-, *y*-, and *z*-component). The *z*-component of the left side of Eq. 78 is given by Z_z' (Eq. 86). Gauss's law of magnetism can be solved for $\breve{H}_z$ by conducting the *z*-derivative. Thus, the appearances of $\breve{H}_z$ can be replaced:

$$\nabla \cdot B = 0 \Rightarrow \breve{H}_z = \frac{-\left(\frac{\partial}{\partial x}\left(\breve{H}_x + \breve{H}_y\right) + \frac{\partial}{\partial y}\left(\breve{H}_x + \breve{H}_y\right)\right)}{j\omega}. \qquad \text{(Eq. 87)}$$

The formulation is now completely described by using $\breve{H}_x$ and $\breve{H}_y$ and the equation system is over-determined. The problem can be reformulated with two-dimensional vectors (where $\left(* \left(\begin{pmatrix} \frac{\partial}{\partial x} \\ \frac{\partial}{\partial y} \end{pmatrix} \wedge \begin{pmatrix} \breve{H}_x \\ \breve{H}_y \end{pmatrix} \right) = \frac{\partial}{\partial x}\breve{H}_y - \frac{\partial}{\partial y}\breve{H}_x \right)$ is the hodge dual of the wedge product):

$$\begin{pmatrix} \frac{\partial}{\partial y} \\ -\frac{\partial}{\partial x} \end{pmatrix} \frac{1}{\varepsilon_{zz}} \left(* \left(\begin{pmatrix} \frac{\partial}{\partial x} \\ \frac{\partial}{\partial y} \end{pmatrix} \wedge \begin{pmatrix} \breve{H}_x \\ \breve{H}_y \end{pmatrix} \right) \right) + j\beta \frac{\varepsilon^T}{\det(\varepsilon_t)} \begin{pmatrix} \frac{\partial}{\partial x} \\ \frac{\partial}{\partial y} \end{pmatrix} \breve{H}_z + \left(\beta^2 \frac{\varepsilon^T}{\det(\varepsilon_t)} - k_0^2 \right) \begin{pmatrix} \breve{H}_x \\ \breve{H}_y \end{pmatrix} = \begin{pmatrix} 0 \\ 0 \end{pmatrix}. \qquad \text{(Eq. 88)}$$

COMSOL can solve this equation as an eigenvalue problem both for eigenvalues $\lambda_\beta = j\beta$ (eigenmode analysis) or $\lambda_\omega = j\omega$ (eigenfrequency analysis) [66].

An alternative approach is given by a three component formulation. Here, a set of three equations for all three field components is considered and the problem can be solved for eigenvalues $\lambda_{\beta,\delta} = -i\beta - \delta_z$ or $\lambda_{\omega,\delta} = -i\omega - \delta_z$ including a loss angle δ_z .

The three component formulation is used in the current model. Linear, lossless materials are considered in the simulation. Analytical approximations of the director fields inside filled capillaries are applied to describe the epsilon-tensor ε_{PHM} inside the liquid crystal inclusions (Eq. 56). The calculation of losses is postponed from the simulation step to a succeeding power loss calculation. The power loss calculation is based on the fields of the ideal, lossless case and the damping of the guided modes is estimated by the scattering loss of the liquid crystal due to orientation fluctuations of the liquid crystal director.

The formulation requires also boundary conditions. Three lossless boundary conditions are used in the current simulations [66]. The boundary conditions are formulated with a vector $\vec{s}$ which is perpendicular to the boundary.

A material with a high electric conductivity, a perfect electric conductor (PEC), is used to model a boundary where the tangential component of the electric field is zero:

$$\vec{s} \times \vec{E} = \vec{0}. \qquad \text{(Eq. 89)}$$

A material with high permeability, a perfect magnetic conductor (PMC), is used to model a boundary where the tangential component of the magnetic field is zero:

$$\vec{s} \times \vec{H} = \vec{0}. \qquad \text{(Eq. 90)}$$

These two boundary conditions are used to terminate the area of calculation. The internal interfaces are modeled with the continuity boundary condition. This represents the natural boundary condition where the continuity of the field components for both $\vec{E}$ and $\vec{H}$ are required:

$$\begin{aligned} \vec{s} \times \left(\vec{H}_1 - \vec{H}_2\right) &= \vec{0}, \\ \vec{s} \times \left(\vec{E}_1 - \vec{E}_2\right) &= \vec{0}. \end{aligned} \qquad \text{(Eq. 91)}$$

This boundary condition is analogue to the natural boundary condition from which Snells and Fresnel laws can be obtained in wave optics [4].

The core of a fiber is surrounded by a trigonal array of air holes which form a hexagon (Fig. 12). The geometry of the fibers is reduced. Only three rings of inclusions are considered. Further, the area of calculation is reduced to a quarter of the fiber by using the PEC and PMC boundary condition at the two cutting edges shown as gray lines in Fig. 12 (by exploiting the mirror planes parallel to the *x*- and *y*-axis). Four runs of the simulation are necessary to find all supported modes. One run for each permutation of the PEC and PMC boundary conditions is required. The PEC boundary condition is used at the curved boundary (the outer boundary of the cladding region). The higher order core modes of the simulated filled photonic crystal fibers show higher attenuations than the fundamental mode (at most 3 modes are found for fibers of the LMA-10 type). The attenuation of the fundamental core mode is shown in the attenuation spectra. Mechanisms like inter modal conversions of core modes are not considered in the current model. The analysis is dedicated to find the spectral windows with low attenuation and the regions with high losses in order to compare these spectra to experimental results. The higher order modes show the same spectral characteristics because the windowed transmission is due to the guiding mechanism and the regions with high losses are determined by the resonances of the inclusions.

4.3.1 Analyzing the effective refractive index of the fundamental mode in a single-mode optical fiber

A single-mode step-index fiber for the IR-spectral region is simulated as example for an isotropic waveguide with simple geometry. The transmission behavior of weakly guiding step-index fibers is well understood [2,3]. The simulated step-index fiber consists of two different isotropic glasses which have slightly differing refractive indices $n_{core} > n_{cladding}$. A perfectly circular core and cladding region are modeled. The core consists of fused silica and the cladding consists of F-doped silica glass. The two glasses were chosen from the glasses reported by Butov et al. [67] for fiber optic applications. The dispersion $n(\lambda_0)$ of the selected glasses is shown in Fig. 48. Butov et al. [67] measured the refractive indices of several glasses and described their results by means of the three parameter Sellmeier formula:

$$n^2(\lambda) = 1 + \sum_{i=1}^{3} \frac{a_i \lambda^2}{\lambda^2 - b_i^2}. \qquad \text{(Eq. 92)}$$

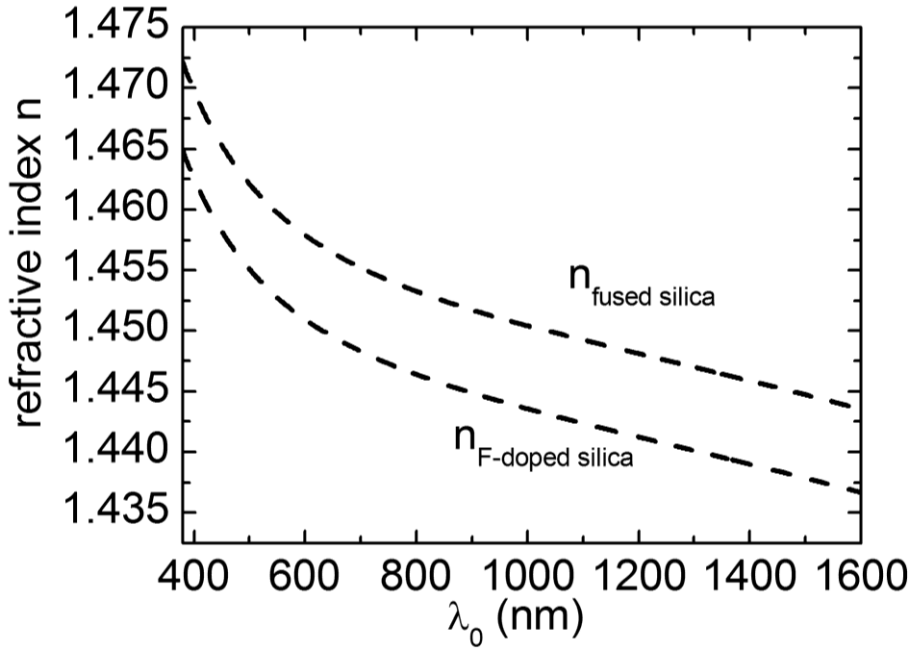

Fig. 48. Refractive indices of fused silica and F-doped silica glass obtained with the Sellmeier coefficient reported in the literature [67].

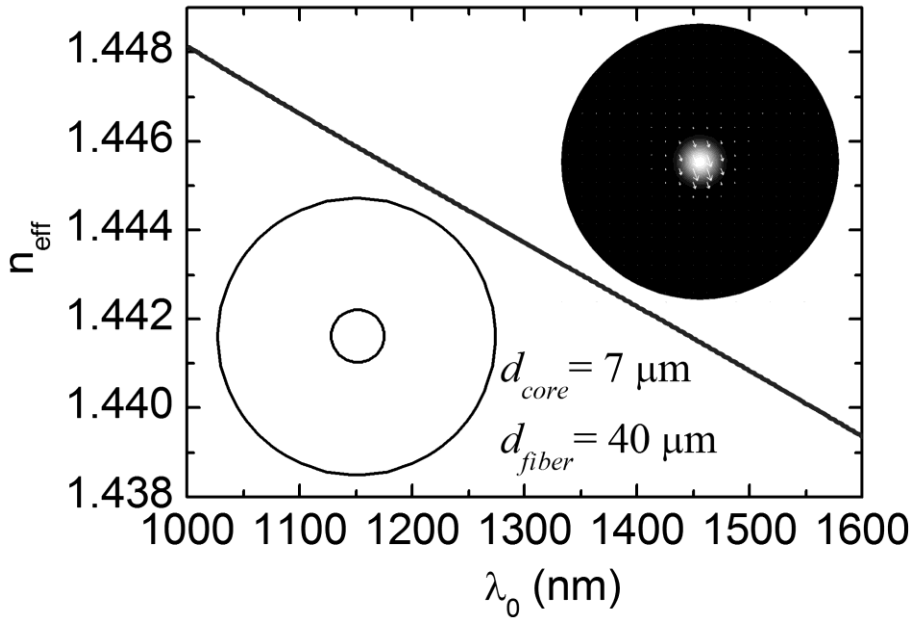

Fig. 49. Simulated effective refractive index of a step-index fiber consisting of fused silica as core material and F-doped silica as Cladding material (core diameter: 7 μm and cladding diameter: 40 μm). The geometry and the simulated fundamental mode (intensity) are shown as inset.

The lower inset of Fig. 49 shows the fiber geometry. The core has a diameter of $7\ \mu m$. The cladding diameter is set to $40\ \mu m$ and the PEC-boundary condition is used at the outer surface of the cladding. The complete fiber is simulated because of the relatively small dimensions. The simulation yields the fields and the eigenvalues and thus $n_{eff}(\lambda_0)$. Some results are plotted together in Fig. 49. The upper inset shows the intensity of the fundamental mode. High brightness corresponds to intensity. This type of plot is very useful to analyze were a mode is located and how it is polarized. As expected, the fundamental mode is located in the core, linear polarized and two fold degenerate (only one degenerate mode is shown). The diagram shows the effective refractive index $n_{eff}(\lambda_0)$ of the fundamental mode. Further, the chromatic dispersion $D(\lambda_0)$ (Eq. 49) of the core mode is calculated from $n_{eff}(\lambda_0)$ (Fig. 50). The dispersion characteristics of step-index fibers were discussed in the chapter 'total internal reflecting waveguides' (Fig. 9). The values of $D(\lambda_0)$, which are obtained in the current simulation, have the expected order of magnitude and the curve shows the typical behavior of a weakly guiding step-index fiber of comparable core diameter. Further, the simulated fiber has a zero-dispersion wavelength of roughly 1300 nm. Summarizing, the simulation of this well-known waveguide leads to the expected results.

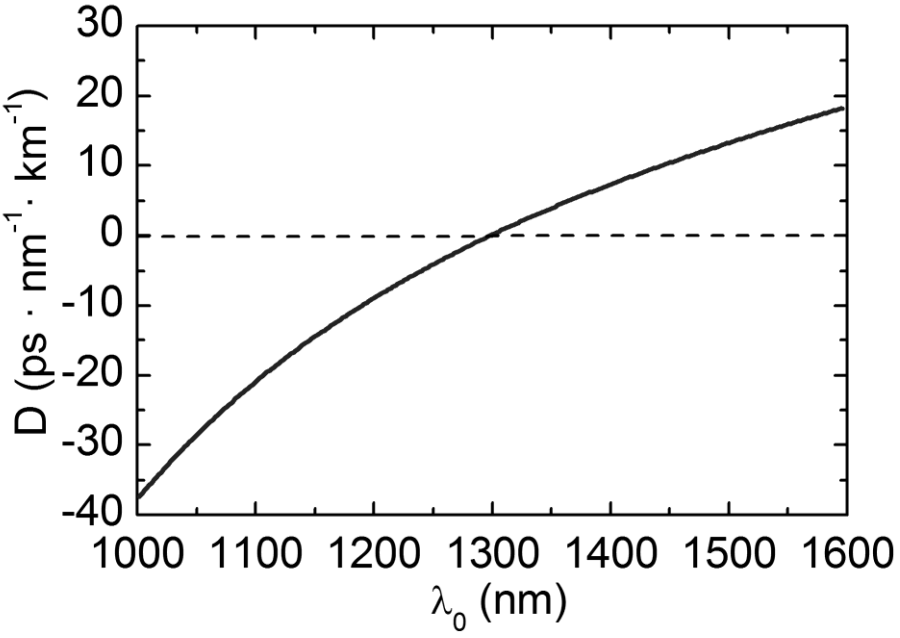

Fig. 50. Chromatic dispersion *D* of a step-index fiber consisting of fused silica as core material and F-doped silica as cladding material (core diameter: 7 μm and cladding diameter: 40 μm).

4.4 Anisotropic scattering (liquid crystal waveguide with rectangular shape)

Experiments on waveguides with a rectangular shape reported in the literature [14] were reconstructed by simulations in the current work in order to develop and test the liquid crystal scattering model which is very useful in the simulation of liquid crystal-filled photonic crystal fibers. Importantly, the current simulations are intended to depict the anisotropic loss in the three different geometries which were analyzed in the reported experiments [14]. In contrast, the exact dimensions of the waveguide reported in the literature are not transferred into the current simulations. However, a rectangular MBBA [22] waveguide (100·20 μm) in an isotropic background material (n_{iso} = 1.46) is simulated. In the first step, the waveguide geometry is defined (Fig. 12). The vacuum wavelength is set to 630 nm and the first few lowest order modes are analyzed. The fields and the effective refractive indices of the lossless case are simulated. The losses are subsequently calculated by using the power loss approach.

[22] n_e(MBBA) = 1.806, n_o(MBBA) = 1.561 (Liq Cryst. 4.7)

The power flow $N(z)$ (Eq. 31) in the waveguide is evaluated by using the fields of the lossless case. The power loss per length $P'(z)$ (Eq. 34) is evaluated in the individual sections of the waveguide. In the current example, the waveguide has two sections; a lossless cladding and a liquid crystal-filled section. The power loss density $p_{V,k}$ is calculated by using the scattering coefficient and the electric fields residing in the liquid crystal-filled section. In the current example, only the loss in the liquid crystal-filled section is of interest. Generally, the power loss density $p_{V,k}$ which occurs in a section k depends on the electric fields in this section, on the frequency of the radiation, and on the imaginary part of the dielectric constant of the material (Eq. 33). The latter two influence parameters can be assumed constant in a given section of a waveguide. Thus, the product $\frac{1}{2}\omega\varepsilon_0\varepsilon_{r,k}''$ is abstracted from the integral in Eq. 34 in order to calculate the power loss per length:

$$p_{V,k} = \frac{1}{2}\omega\varepsilon_0\varepsilon_{r,k}''\left|\vec{E}_{\boldsymbol{k}}{}^2\right|. \qquad \text{(Eq. 33)}$$

$$P'(z) = \sum_k \int_{A_k} p_{V,k}\,dA = \sum_k \int_{A_k} \frac{1}{2}\omega\varepsilon_0\varepsilon_{r,k}''\left|\vec{E}_{\boldsymbol{k}}{}^2\right|dA = \sum_k \frac{1}{2}\omega\varepsilon_0\varepsilon_{r,k}'' \int_{A_k}\left|\vec{E}_{\boldsymbol{k}}{}^2\right| \qquad \text{(Eq. 93)}$$

A view on Beer-Lambert's law of absorption led to Eq. 25. The absorption coefficient α describes the conversion of electromagnetic energy to heat. The absorption coefficient α may very well be replaced with the scattering coefficient α_{sc} to describe the scattering loss:

$$\alpha = 2k_0 n'' = \frac{4\pi}{\lambda_0} n'' = \alpha_{sc} \Rightarrow n'' = \frac{\alpha_{sc}\lambda_0}{4\pi}. \qquad \text{(Eq. 94)}$$

This results the imaginary part ε_{k_r}'' of the dielectric constant (Eq. 32c, with n_k', the real part of the refractive index of the appropriate section):

$$\varepsilon_{k\,r}'' = -2n_k'\frac{\alpha_{sc}\lambda_0}{4\pi}. \qquad \text{(Eq. 95)}$$

$p_{VC,k}$ is then finally calculated with the relation $\omega = \frac{c}{\lambda_0}2\pi$:

$$p_{VC,k} = \frac{1}{2}\omega\varepsilon_0\varepsilon_{r,k}'' = \frac{1}{2}\frac{c}{\lambda_0}2\pi\varepsilon_0(-2)\frac{\alpha_{sc}\lambda_0}{4\pi}n_k' = -\alpha_{sc}\frac{c\varepsilon_0}{2}n_k' \qquad \text{(Eq. 96)}$$

The sign of $p_{VC,k}$ may be considered to distinguish between amplification (positive sign) and loss (negative sign). No amplification processes are of interest concerning the propagation inside the waveguides in the current work. Consequently, the negative sing of Eq. 96 is neglected and the attenuation of the waveguide is evaluated by using Eq. 35:

$$a_{waveguide} = \frac{P'(z)}{N(z)}. \qquad \text{(Eq. 35)}$$

In the current example, either $\alpha_{sc,1}$, $\alpha_{sc,2}$, or $\alpha_{sc,3}$ need to be considered according to the respective geometry of the waveguide because the scattering is not independent of the orientation of the electric field vector relative to the liquid crystal director. Furthermore, the anisotropy of the refractive index of the liquid crystal has to be considered.

The polarization (electric field) of the *TE* - and *TM*-modes is shown in the upper section of Fig. 51. Two different director orientations are simulated in order to reproduce the experiments which were summarized in the introduction. The two modes with the lowest order are shown in Fig. 51.

In the first case *i*), the director is parallel to the propagation direction $\left(\vec{v} \parallel \vec{k}\right)$ and all shown modes have an effective refractive index of $(n_{eff} \approx n_o)$. $\alpha_{lc,1}$ = 490 m^{-1} and the ordinary refractive index of MBBA $(n_k' = n_o)$ are used in the power loss calculation. The estimated loss of 21 dB/cm is degenerate for *TE* and *TM*-waves in this geometry.

In the two further cases, the director is aligned parallel to the *x*-direction and thus perpendicular to the propagation direction $\left(\vec{v} \perp \vec{k}\right)$. Firstly, *TM*-waves are evaluated where the electric field is perpendicular to the director orientation (case *ii*). In Fig. 51 *ii*, the shown *TM*-modes have an effective refractive index of $(n_{eff} \approx n_o)$. $\alpha_{lc,2}$ = 1210 m^{-1} and the ordinary refractive index $(n_k' = n_o)$ are used in the power loss calculation. A loss of 45 dB/cm is found.

In the third case *iii*), *TE*-waves are considered. Now the effective refractive indices are higher $(n_{eff} \approx n_e)$. A loss of 64 dB/cm is found by considering $\alpha_{lc,3}$ = 1470 m^{-1} and $(n_k' = n_e)$.

The current simulations are compared to the literature results which are summarized in the introduction (filled stars, Fig. 52). The simulated losses fit the

expected losses. The losses for the second case (*ii*) are little lower in the current simulations than expected by the literature. The literature reveals the tendency that the losses are lower in a waveguide than in the bulk (filled diamonds). This tendency is also revealed by the current simulations, although the dimensions of the reported experimental waveguide and the current simulation are not in exact agreement. As in the literature, the simulated losses are highest in the geometry *iii*) and lowest in the geometry *i*). The degeneration of the losses of *TE*- and *TM*-waves cancels in the case where $\vec{\nu} \perp \vec{k}$ as expected by the anisotropy of the scattering cross section. In conclusion, the simulated loss-behavior is in reasonable agreement with the experiments from the literature.

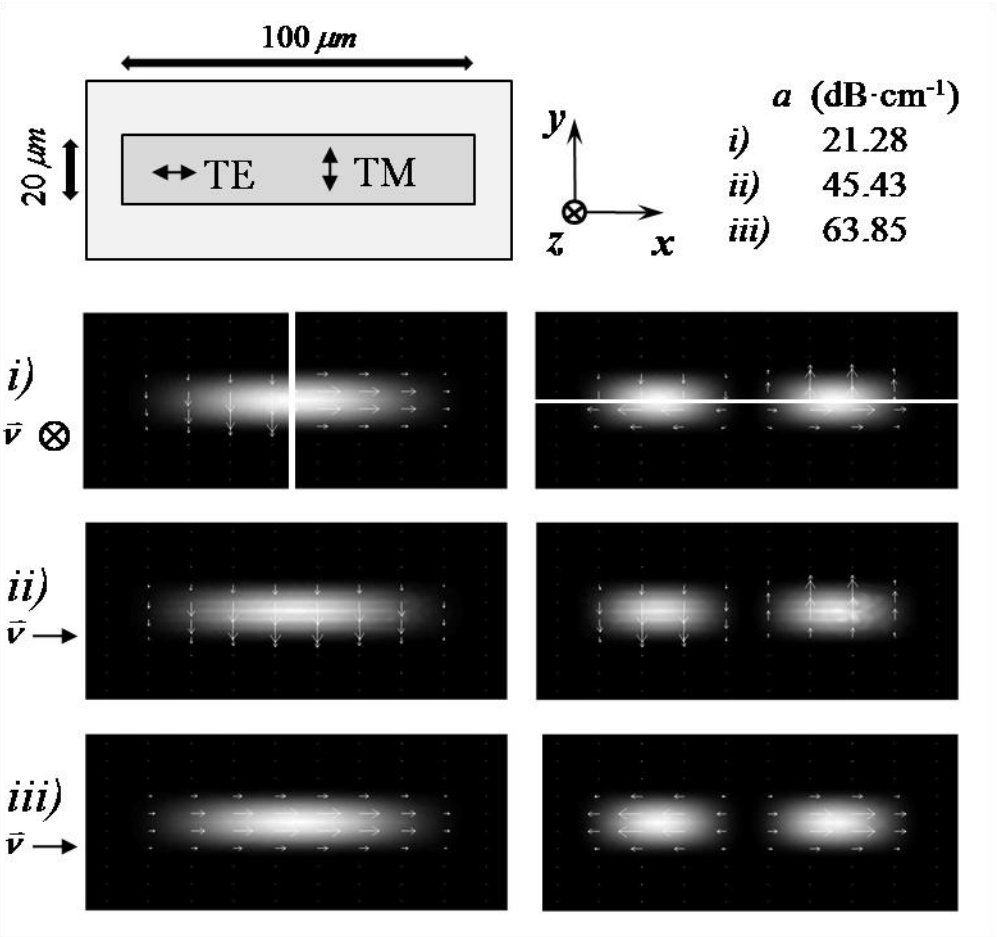

Fig. 51. Simulated liquid crystal waveguide with rectangular shape. The top profile shows the geometry of the simulation; a glass region (light gray) and a liquid crystal-filled section (darker gray) with rectangular shape are considered. The simulation corresponds to a wavelength of 630 nm. The two lowest order modes are shown for two different director fields. *i*) uniform director field where the director $\vec{\nu}$ is perpendicular to the profile. The shown TE and TM modes are twofold degenerate. (attenuation: 21.28 dB·cm^{-1}) *ii and iii*) uniform director field where $\vec{\nu}$ is parallel to the *x*-direction. The attenuation for the shown TM-modes is 45.43 dB·cm^{-1}(*ii*). The attenuation for the shown TE-modes is 63.85 dB·cm^{-1} (*iii*).

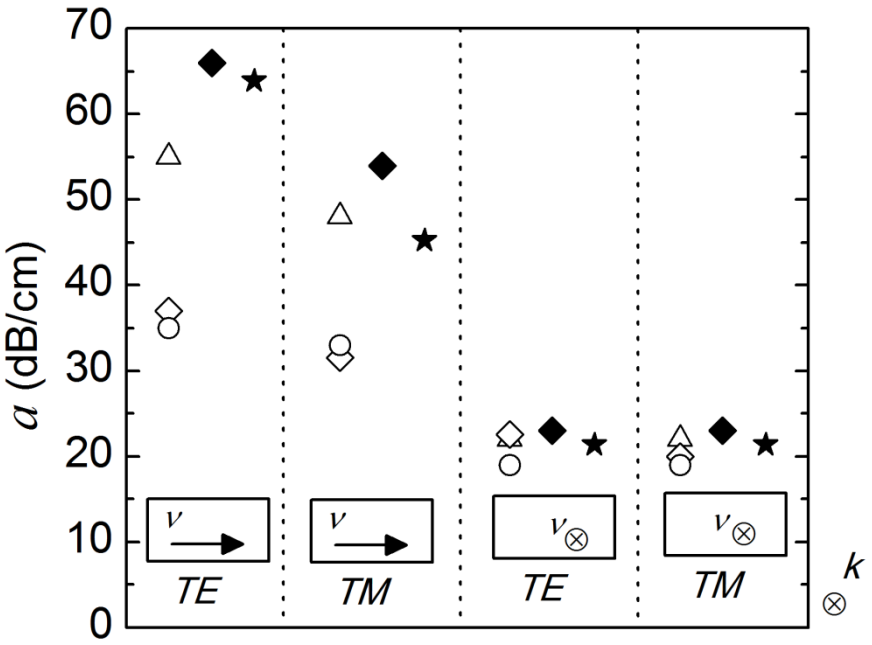

Fig. 52. Losses of a MBBA waveguide with a rectangular shape. The arrows indicate the orientation of the director and the propagation direction in the waveguide. The figure summarizes the currently simulated data (filled stars) with data from [14, open symbols]. Different glasses were used as background material: fused silica (open diamonds, open rings, filled stars), acryl glass (rings), pyrex glass (filled diamonds). All data shown is experimental data except the current simulation results and the open triangles (which correspond to a theoretical prediction). The losses of a 1.3 mm thick PMMA layer are shown additionally [49, filled diamonds]. In the original work, it is not distinguished between the *TE*- and the *TM*-case for $\vec{\nu} \parallel \vec{k}$ (*a*(TE) = *a*(TM) is assumed in this figure).

4.4.1 Scattering model for filled photonic crystal fibers

The scattering due to thermal fluctuations of the director is of high importance in the liquid crystal inclusions of filled photonic crystal fibers with a glass core. The liquid crystal inclusions act as wavelength selective damping units in the spectral regions with high loss. These losses can be described by an average scattering coefficient in the liquid crystal-filled inclusions. And this approximation is especially suited in the case of director fields with a high complexity, like for instance the escaped radial director field. In the high loss regions, the fields may escape the core and interpenetrate the inclusions. Thereby, the fields are scattered on average due to all three components of the scattering cross section. Thus, the average scattering coefficient $\alpha_{lc,0}$ (Eq. 55), the average refractive index of the liquid crystal $\left(n_k' = \sqrt{\frac{2n_o^{\,2} + n_e^{\,2}}{3}} \right)$, and $\left(\Delta\varepsilon = n_e^{\,2} - n_o^{\,2} \right)$ are inserted into Eq. 96:

$$\left|p_{VC,k}\right| = \frac{1}{2}\omega\varepsilon_0\varepsilon_{r,k}'' = \alpha_{lc,0}\frac{c\varepsilon_0}{2}n_k' = \frac{\pi}{2}\frac{c\varepsilon_0 k_B T}{\lambda_0^{\,2}K_{33}}\frac{\left(n_e - n_o\right)}{n_o'^2}\sqrt{\frac{2n_o^{\,2}+n_e^{\,2}}{3}} \quad \text{(Eq. 97)}$$

The average scattering coefficient leads to rather high losses. In the example of the lab waveguide, the losses are 59 dB/cm in the first geometry (*i*) and 52 dB/cm in the second and third geometry (*ii* and *iii*). A scattering coefficient $\alpha_{Si} = 9\cdot10^{-8}m^{-1}$ is considered in the silica regions [68].

4.5 Comparing the simulations to a model presented in the literature

Sun et al. [33] simulated an all-theoretical fiber filled with a theoretical liquid crystal. They simulated the transmission through a 1 mm long piece of a liquid crystal-filled photonic crystal fiber with parallel orientation of the liquid crystal director (Fig. 53). They apply a full vectorial beam propagation method [33] evaluating the leakage loss by using the transparent boundary condition [69]. In the beam propagation method, this problem independent boundary condition is an alternative to perfectly matched layers and has been established even before the invention of perfectly matched layers [70]. Sun et al. simulated a fiber with three rings of holes, a pitch of $p = 5\ \mu m$ and a capillary diameter of $2\cdot R_i = 1.55\ \mu m$. They conducted a modal analysis of an all-theoretical fiber consisting of a backbone material with the constant refractive index $n_{silica} = 1.45$. Further, the birefringent inclusions were treated as being uniaxial having the optical axis in *z*-direction (Eq. 98) and considering the refractive indices of an arbitrary liquid crystal using the representative constant refractive indices $n_o = 1.5$ and $n_e = 1.7$.

$$\tilde{\varepsilon} = \begin{pmatrix} n_o^2 & 0 & 0 \\ 0 & n_o^2 & 0 \\ 0 & 0 & n_e^2 \end{pmatrix} \quad \text{(Eq. 98)}$$

Although Sun et al. abandoned comparing their results to experimental data they compared their simulated results to data calculated by the analytical ARROW [71] model of Litchinitser [12].

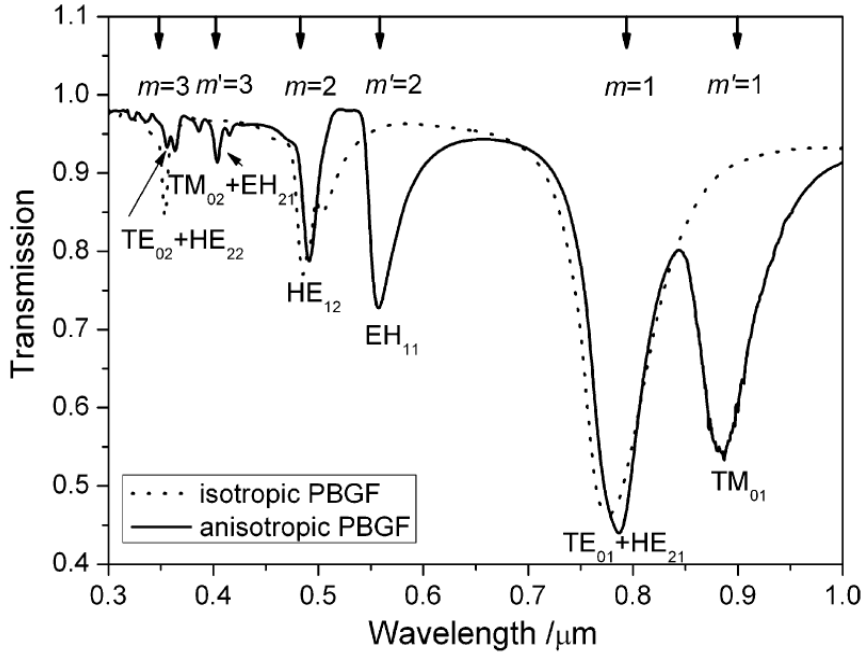

Fig. 53. Transmission spectrum of an isotropic and an anisotropic photonic bandgap fiber (PBGF, solid line). The transmission through a 1 mm long piece of a fiber was simulated. The position of the transmission minima calculated by the ARROW model are indicated by arrows. Figure copied from [33].

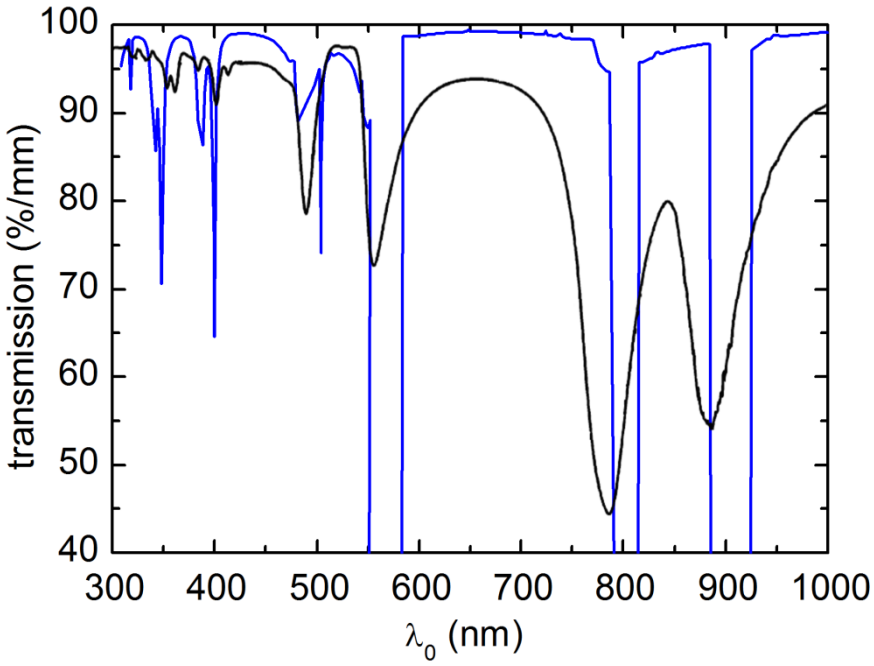

Fig. 54. Transmission spectrum simulated by Sun et al. (black line) [33] a transmission spectrum generated in the current simulations (blue line) by using the same refractive indices n_o, n_e, and geometry parameters p and R_i.

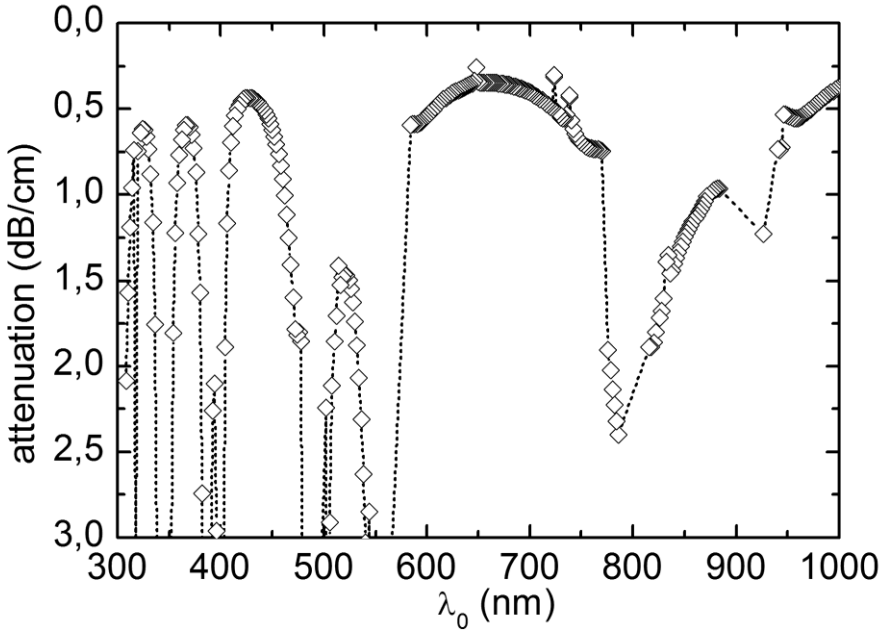

Fig. 55. Attenuation spectrum generated in the current simulations by using the same refractive indices n_o, n_e, and geometric parameters p and R_i as Sun et al. [33].

The transmission spectrum calculated by Sun et al. and the respective attenuation spectrum generated by the current simulation and are plotted together in Fig. 54. Sun et al. simulated the transmission for a sample length of 1 mm. The curves show almost the same characteristics, although there are some deviations. Two mayor difference should be emphasized. i) In Fig. 54, the transmission window at $\lambda_0 = 515\,\text{nm}$ clearly exhibits lower transmission than its two neigboring transmission windows. ii) In contrast to the result of Sun et al. the transmission maxima are decreasing at $\lambda_0 > 500$ with decreasing wavelength. Nevertheless, the minor deviations bear interesting information about the current simulation technique and how the results should be interpreted. Three types of deviations are indicated in Fig. 56 and will be discussed in the following.

The first effect is indicated by rings. Randomly appearing modes of the outer cladding couple artificially to the guided core modes. These parasitic simulation modes are identified by the corresponding minima of the filling factor (Fig. 57). To understand the devations of the simulation in detail firstly an example without systematical errors shall be discussed. To prevent misunderstandings it should once more be noticed, that the attenuation is calculated using the undisturbed fields in a calculation of perturbation. The undisturbed fields are used to calculate and plot the undisturbed modal intensity showing where the undisturbed fields concentrate.

These modal intensity plots should not be mistaken with a near field image at the end face of a longer piece of fiber. Modal intensity plots at characteristic spectral regions of a selected transmission window are shown in Fig. 58. The modal intensity profiles a) and b) correspond to the band edge at $\lambda_0 \approx 500$. In a) a resonant inclusion mode is shown which has $n_{eff,inclusion} \approx n_{silica}$. The effective refractive index of this cladding mode crosses the silica line at $\lambda_0 \approx 500\,nm$ with negative slope. The effective refractive index of the fundamental core mode shown in b) remains smaller than the effective refractive index of silica $n_{eff,core} < n_{silica}$ over the whole bandgap. This is as well shown by the effective refractive indices indicated for c) and d). Nevertheless, there is an energetic crosstalk between the fundamental core mode and the resonant cladding mode at the bandedges, as seen in b) and for another resonant cladding mode at higher wavelength shown in d). At the attenuation minimum at $\lambda_0 = 520\,nm$, the fundamental core mode penetratess the incluisions only weakly, as shown in c). Compared to the attenuation minimum at $\lambda_0 = 670\,nm$ (Fig. 58 c), the penetration of the core mode into the inclusions is a little higher at $\lambda_0 = 520\,nm$. Thus, the attenuation minimum at $\lambda_0 = 520\,nm$ has a higher attenuation. The deviations in the transmssion window between $\lambda_0 = 584\,nm$ and $\lambda_0 = 786\,nm$ can be well understood with the help of such modal intensity profiles.

The origin of parasitic modes indicated by cycles is shown in Fig. 58 b); there is intensity between the outer boundary and the third ring of inclusions. Obviously, this intensity is not related to the fundamental core mode. Instead, this is a mode of the inclusion free outer cladding region. This mode contains no information for the real fiber because the outer diameter of the area of calculation is not the diameter of the real fiber. On the contrary, this diameter is downscaled in order to minimize the area of calculation. An artificial upbending of the attenuation curve to lower values at the band edges is indicated by ellipses. As seen in Fig. 59 a) and c) this is due to the abandonment of an attenuating boundary condition at the outer boundary of the area of calculation. The core mode penetrates through all three rings of inclusions and disturbing back reflections are caused. In these sections, the electromagnetic fields found by the simulation are not a very good approximation to the real system. However, the deviation caused by this effect is small and can be easily identified in

the simulated spectra. Accordingly, such artificial upbendings can be identified and neglected during the interpretation.

The actual fiber geometry is especially vulnerable for these deviations. The deviations are minimized for an increasing product $R_i \cdot n_{inclusion}$. The simulations of the E7 filled LMA-8 or LMA-10 fibers are nearly free of these deviations.

The last point to be discussed are the deviations indicated in Fig. 56 by bars. Here, gaps are appearing. In these regions, the simulated data was simlpy excluded form analysis because the core mode can only hardly be identified; to many modes are found by the simulation, which are not corresponding to the real system. Only modes are considered in the analysis, where a fraction of 75 % of the intensity is residing in the core region. No such modes are found in these gaps.

In conclusion, the simulation results fit the data of Sun et al. very well. Three types of systematic deviations are easily identified so that a very detailed analysis of the simulated spectra is possible. However, the quality of the simulation needs to be veryfied by comparison with experimental results.

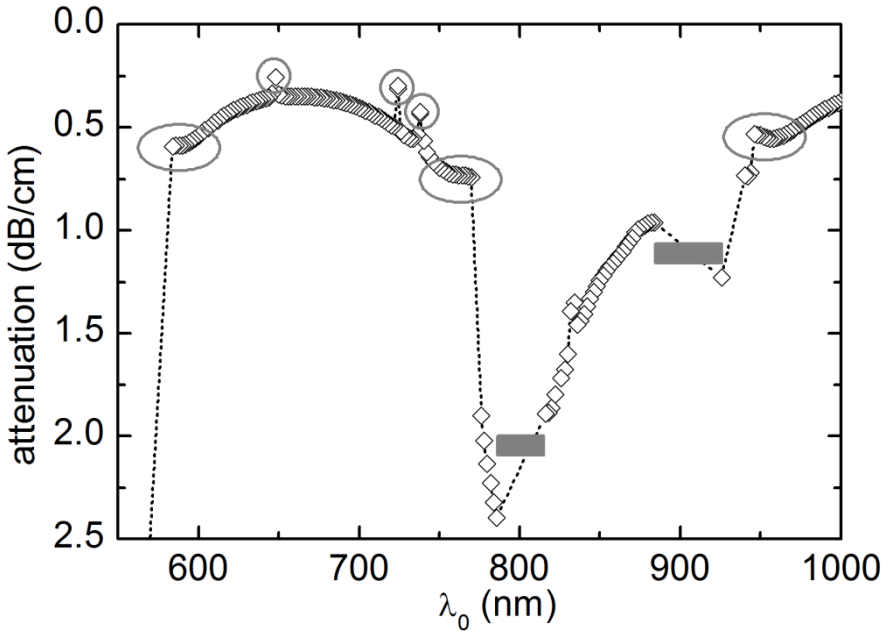

Fig. 56. Smaller deviations of the simulation technique easily to be identified. The deviations are indicated by cycles, ellipses and bars.

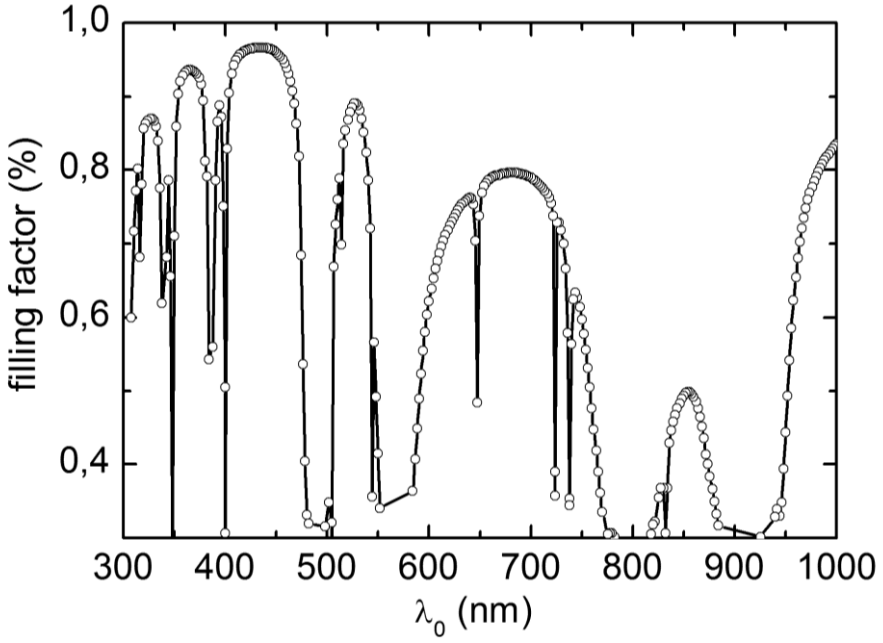

Fig. 57. Filling factor of the core region (simulation result).

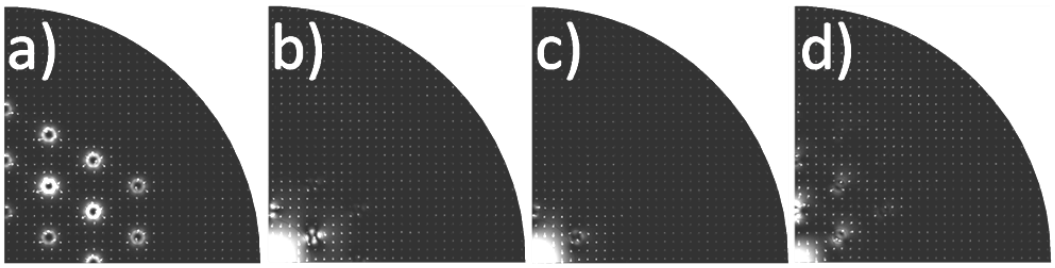

Fig. 58. Simulated intensity (shade, calculated from the undisturbed fields) and electric field vector in the xy-plane (arrows). a) inclusion modes at λ_0 = 498 nm, n_{eff} = 1.4503, a = 19 dB/cm b) core mode at λ_0 = 506 nm, n_{eff} = 1.4496, a = 2.9 dB/cm. c) core mode at λ_0 = 520 nm , n_{eff} =1.4495, a = 1.5 dB/cm. d) core mode at λ_0 = 550 nm, n_{eff} =1.4498, a = 5.3 dB/cm.

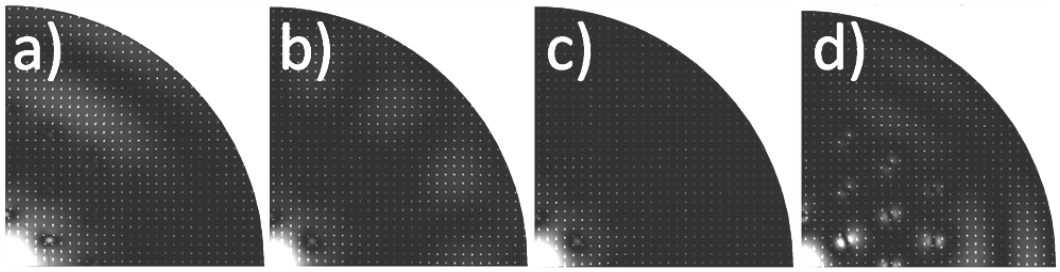

Fig. 59. Intensity in the cladding. a) core mode at λ_0 =584 nm, n_{eff} =1.4495, a = 0.6 dB/cm. b) core mode at λ_0 = 648 nm, n_{eff} = 1.4492, a = 0.25 dB/cm. c) core mode at λ_0 =670 nm, n_{eff} =1.4491, a = 0.35 dB/cm. d) core mode at λ_0 =768 nm, n_{eff} = 1.4484 , a = 0.74 dB/cm.

4.6 Fibers with planar anchoring – uniaxial inclusions

4.6.1 The influence of the inclusion diameter; two photonic crystal fibers with planar anchoring

This chapter shows how simulations can be used as a design tool to understand how the fiber parameters and the anchoring agents influence the attenuation properties of the fibers.

Two fibers with equal director fields are generated by treating the two fibers LMA-8 and LMA-10 with glymo and filling them with E7. Fibers with equal director fields are generated by this procedure. In both cases, the inclusions can be treated as being optically uniaxial, with the optical axis in *z*-direction. The inclusion radius is varied from $R_i = 1.2$ μm to $R_i = 1.5$ μm by exchanging fiber LMA-8 with fiber LMA-10. The pitch p is altered from 5.5 μm to 6.5 μm. The two fiber parameters are varied in the current simulations, accordingly.

Litchinitser et al. reported that for all-solid photonic bandgap fibers with isotropic high index inclusions ($n_{inclusion} > n_{glass}$), the scattering properties of the single high index inclusions determine the spectral transmission characteristics rather than their position and number [12]. From their formula for the transmission minima (Eq. 71) it can be seen, that the minima shift to higher wavelength with increasing inclusion radius.

Sun et al. [33] simulated a theoretical fiber with isotropic and anisotropic liquid crystal inclusions, respectively. They showed that by considering birefringent liquid crystal inclusions having the optical axis in *z*-direction, the transmission spectrum of the isotropic fiber is modified and additional transmission minima occur. From this it can be concluded, that the transmission windows should shift to higher wavelength with increasing R_i in the case of high index uniaxial inclusions with the optical axis in *z*-direction. The same spectral shift is found in the current simulations (Fig. 60). The respective attenuation spectra of four simulations using different inclusion radii are plotted together in this figure. A black square is used to mark one particular transmission window in order to show the spectral shift.

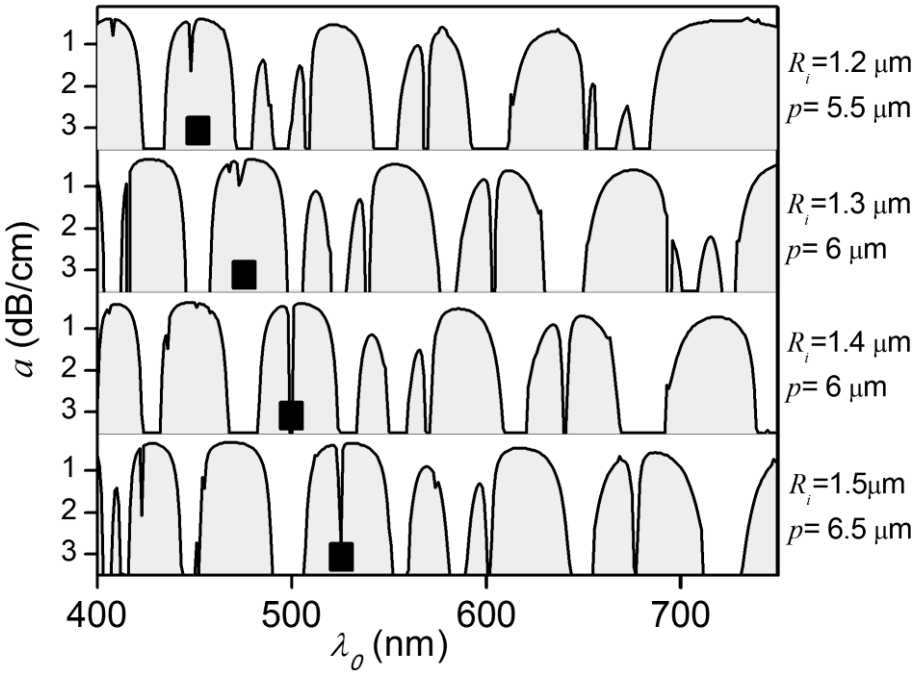

Fig. 60. Simulated attenuation spectra systematically varying the pitch p and the inclusion radius R_i.

The inclusion radii R_i of the fibers were measured by scanning electron microscopy. Surprisingly, the best fit for the LMA-10 fiber is achieved by using a slightly larger inclusion radius R_i = 1.55 μm in the simulation than the measured value of 1.5 μm. The simulated attenuation spectra are plotted together with the measured attenuation spectra in Fig. 61. The simulated data fit the experiments very well. Although, the simulated attenuations are systematically lower. The symbols in Fig. 61 represent one respective transmission window, each. The symbols are shown in order to help identifying the individual transmission windows in the experimental and simulated attenuation spectra. By this allocation, the spectral shift is seen again clearly: two new transmission windows enter the selected spectral region as the inclusion radii increase from 1.2 μm to ≈ 1.5 μm. The resolution of the measured spectra is high enough to compare them qualitatively to the simulated spectra. The allocation of most of the transmission windows is straight forward. However, the transmission windows which are marked with the cycle ● and the up-pointing triangle ▲ are merged both for the LMA-8 fiber and for the LMA-10 fiber. The transmission windows which are marked with the down-pointing triangle ▼ and the rectangle ▮ are separated for the LMA-8 fiber but have merged in the experimentally observed spectra of the LMA-10 fiber.

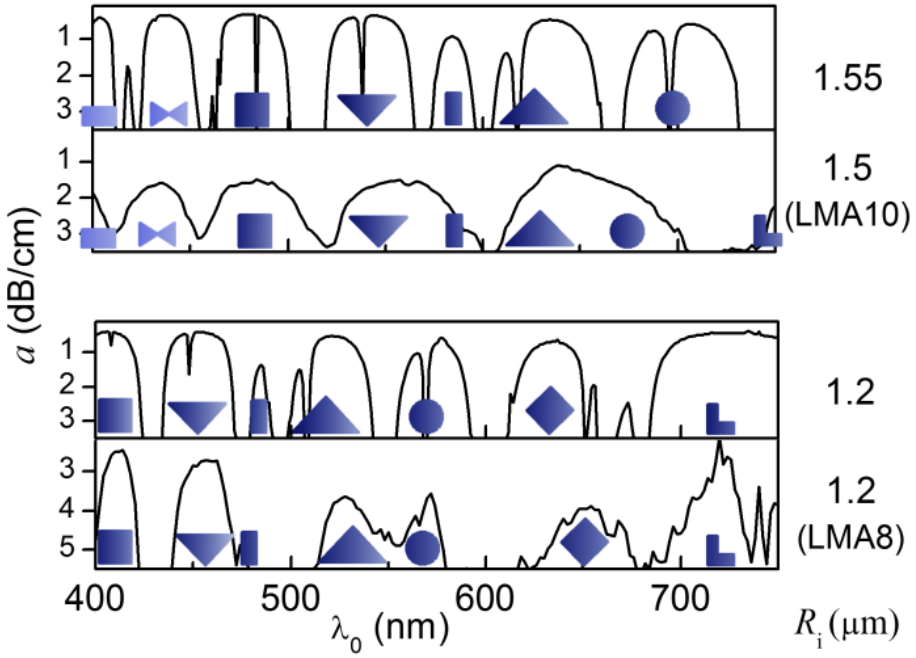

Fig. 61. Simulated and measured attenuation spectra of the LMA-8 and LMA-10 fiber treated with glymo and filled with E7 (simulated spectra at the top, respectively).

4.6.2 Towards the polarizing properties

The cut-back technique is not applied to addressable fibers in the current experiments. Thus, no attenuation spectra for fibers with applied addressing fields were measured. Highly interesting polarizing properties were observed for fibers with parallel anchoring in the switching experiments. These fibers attenuate the *y*-polarized part of the initial intensity and allow selective transmission of *x*-polarized light with high polarization extinction ratios.

The director fields inside single capillaries can be investigated by polarizing optical microscopy with applied fields. Some experimental approaches towards such investigations have been tested. Sometimes, just brightness differences were observed due to the application of external fields instead of a clear modification of the characteristic stripe textures.

Summarizing, neither the exact director fields inside the inclusions of the fibers nor the attenuation spectra of the fibers are exactly known in the field-on state. But the experimental results of the switching experiments show high transmission in several spectral regions selectively for *x*-polarized light. The simulated spectrum of the field-off state is shown (first spectrum, Fig. 62). Only a quarter of the fiber is simulated and the PEC and PMC boundary condition are used at the cutting edges in

x- and *y*-direction (Fig. 12). The linear polarized fundamental core mode is twofold degenerate. The *y*-polarized mode is found if the PEC-boundary condition is used at the *x*-boundary and the PMC-boundary condition is used at the *y*-boundary. The *x*-polarized mode is found if the PEC-boundary condition is used at the *y*-boundary and the PMC-boundary condition is used at the *x*-boundary. The attenuation spectra of both cases are degenerate if the director field in the inclusions exhibits a rotational symmetry.

The liquid crystal E7 has positive dielectric anisotropy and realigns parallel to the field lines of an external addressing electric field. Thus, the director fields of the inclusions have probably no rotational symmetry if external addressing fields are applied in the *y*-direction. If so, the attenuation characteristics for the *x*- and *y*-polarized fundamental core mode are no longer degenerate.

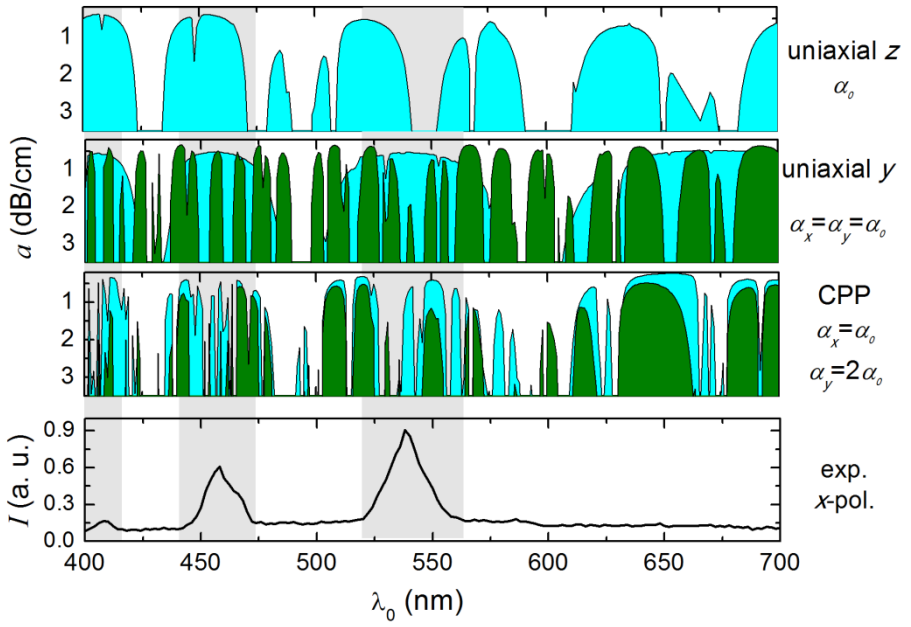

Fig. 62. Simulated attenuation spectra of a fiber with planar anchoring, E7. One experimental spectrum is also shown (lower spectrum). The experimental spectrum shows the output power of a 1.5 cm long piece of the fiber with strong electric fields applied in *y*-direction (320V/130 μm, 1 kHz). The output power is recorded with a polarizer in *x*-direction and a PMT-detector. The first simulated spectrum (at the top) corresponds to the no-field state. The second spectrum shows the attenuation of a fiber with uniaxial inclusions having the optical axis in *y*-direction. The third spectrum shows the attenuation of a fiber with a CPP-director field where the director is parallel to the *y*-direction in the center of the inclusions and parallel to the glass surface at the boundaries of the liquid crystal inclusions. The spectra of *x*-polarized light are shown in cyan and the spectra of *y*-polarized light are shown in olive.

The surface interaction of the liquid crystal with the glass boundaries can be completely ignored as theoretical starting point. This corresponds to the case where

the optical axis is uniformly oriented parallel to the *y*-direction in the field-on state (Fig. 62, second spectrum). The attenuation spectra of the *x*-polarized mode are shown in cyan and the spectra of the *y*-polarized mode are shown in olive. These simulations show an interesting tendency. The inclusions support a larger number of *y*-polarized modes and show a larger number of resonances in the simulated spectral region for *y*-polarized light than for *x*-polarized light. Accordingly, a large number of green peaks and only four cyan peaks are seen in the second spectrum. These spectra are simulated with the isotropic scattering coefficient $\alpha_{lc,0}$. It could be stated that the experimentally observed strong attenuation of *y*-polarized light is due to the filigree structure of the spectrum with a large number of narrow peaks. The *x*-polarized light exhibits possibly a low attenuation due to the broad windows. This fits the experimental observations well in the spectral region from 400 to 600 nm. This is indicated by the gray shaded regions. At higher wavelength, there is also a broad window with low attenuation in the cyan-colored spectrum. But no transmission is observed here experimentally.

In the third spectrum, a CPP-type director field is used where the director is parallel to the field lines of the addressing field near the center of the inclusions and parallel to the glass walls at the boundaries of the inclusions. A higher scattering coefficient of the liquid crystal inclusions $\alpha_y = 2\alpha_x$ is used in the power loss calculation for the *y*-polarized core mode. Accordingly, the height of the olive peaks is smaller than the height of the cyan peaks. In some regions solely cyan peaks appear. Interestingly, the peaks of the experimental spectrum (lower spectrum) fit very well into these regions although there are single cyan peaks without a matching peak of the experimental spectrum.

The experimental spectra show a tendency. The attenuation in the spectral regions where a polarized transmission is observed in the field-on state is higher than the minimal attenuation observed in the field-off state. At high voltages the peaks have approximately half the height as in the field-off state. This is maybe understood by means of the anisotropy of the scattering cross section. In the field-off state, the scattering of the fields inside the inclusions is maybe due to the scattering coefficient $\alpha_{lc,1}$. The liquid crystal realigns and the scattering of the fields is then maybe due to $\alpha_{lc,2}$ or $\alpha_{lc,3}$ $\left(\alpha_{lc,2} \approx 3\alpha_{lc,1}\right)$.

The high polarization extinction ratio of *x*- and *y*-polarized light in the field-on state cannot be solely attributed to the contrast of $\alpha_{lc,2}$ and $\alpha_{lc,3}$ because it is too small $\left(\alpha_{lc,3} \approx 1.5\,\alpha_{lc,2}\right)$. Nevertheless, the *y*-polarized light is probably not lost because of weaker confinement in the core. Rather, there may be some kind of scattering in the inclusions which is not only due to orientation fluctuations of the director. For example, there could be a stronger anisotropy of the scattering coefficient due to defects of the director field. If so, the third spectrum (Fig. 62) maybe provides a partial explanation of the observed experimental spectrum. It is possible that the light exhibits a strong attenuation independent of the polarization in the regions where green and cyan peaks overlap and low attenuation of x-polarized light is selectively possible in regions where cyan peaks appear solely.

4.6.2.2 Simulation of fiber LMA-10 with ZLI-2461, planar anchoring

The Cauchy coefficients for ZLI 2461 are recorded with a wavelength dependent Jelly micro refractometer (see Appendix 'Dispersion of nematic liquid crystals'). The recorded coefficients and an inclusion radius of $R_i = 1.505$ µm are used in the simulations.

The simulated attenuation spectrum shows three rather broad transmission windows in the visible spectral region (Fig. 63). The cut-back spectrum of the filled fiber has a contrast ratio of only 2 dB/cm. The structure of the experimental spectrum could be interpreted to have numerous transmission windows. But it is also possible to divide the attenuation spectrum into three regions as indicated by the black bars in Fig. 63. These three bars correspond to the three simulated transmission windows. The bar in the red spectral region is clearly drawn over a section with high loss in the experimental spectrum. But the corresponding simulated transmission window has a lossy region as well. The assignment of the center bar assumes that the weak contrast of the experimental spectrum is not sufficient to give a proper resolution of the band edges.

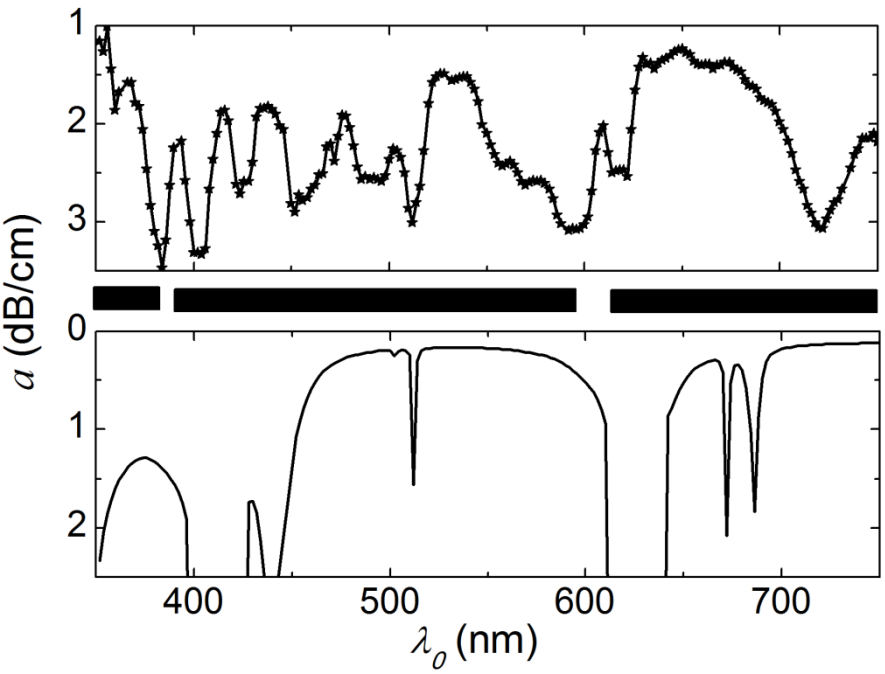

Fig. 63. Attenuation spectra of fiber LMA-10 filled with ZLI 2461. Experimental attenuation spectrum (upper graph) and simulated spectrum (lower graph). The black bars indicate three transmission windows.

4.7 Fibers with perpendicular anchoring

The escaped radial director field is assumed in the liquid crystal inclusions. Two different approaches are used to simulate the fibers.

The dielectric tensor is approximated quite roughly in the first approach. The one constant approximation is used and a high value for σ is considered. Moreover, only the contributions of the dielectric anisotropy to the *x*- and *y*-components of the dielectric tensor are examined. Thus, the *z*-component $(\varepsilon_{zz} = n_o)$ of the dielectric tensor is too low near the center of the capillary. This is maybe compensated by a high σ. However, the implementation of the director field is a very simplified assumption. However, using this approximation the experimental data is resembled well. The measured and simulated spectra are plotted together in Fig. 64. The main transmission characteristics are found by the simulation. The spectra of the real system are noisier and the simulated attenuations of the fundamental core mode are lower than the observed attenuations. The six transmission bands in the experimentally investigated spectral region are reproduced by the simulation. In Fig.

64, these transmission windows are indicated by bars. The attenuation maxima at 508, 568, 638 and 836 nm are accurately reproduced by the simulation. Unfortunately, the measured spectrum is quite noisy at lower wavelengths. At wavelengths smaller than 638 nm, the simulation reveals the tendency that the transmission windows are getting narrower with decreasing wavelength. This tendency can also be seen in the measured spectra. The transmission window around 730 nm, which is unusually small, is seen in the measurement as well as in the simulation. However, the shape of the simulation spectrum does not resemble the experimental one exactly. The position of the attenuation maxima in the simulations is in good agreement with the experimental maxima for most of the transmission windows. On the one hand this can be due to the fact, that leakage loss was not included in the simulations. On the other hand, this problem occurs also for simulations evaluating the leakage loss [13]. The rough implementation of the escaped radial director field might be the reason that some of the attenuation maxima match very well the experimental results, while some do not.

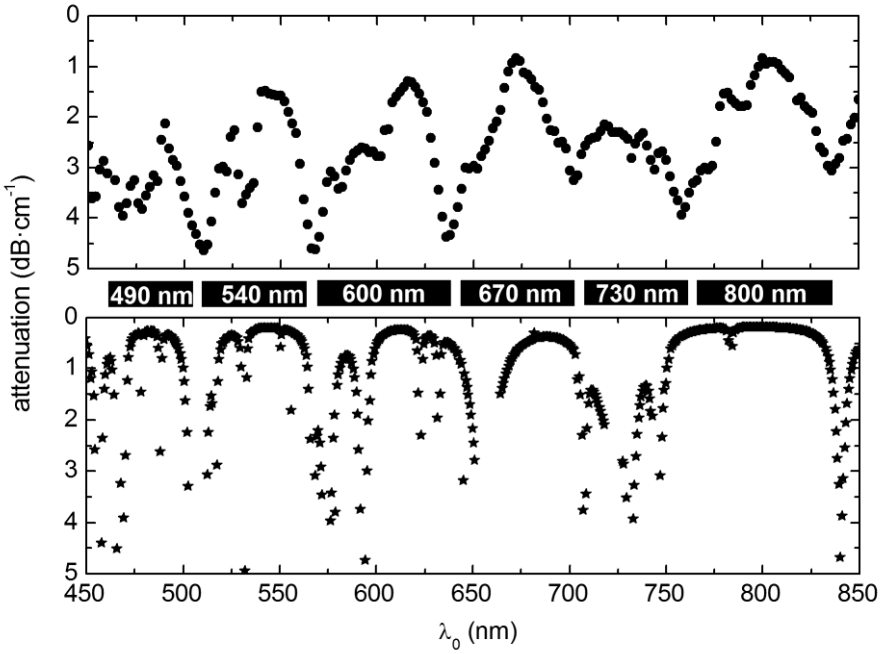

Fig. 64. Fiber LMA-10, perpendicular anchoring, E7. Measured attenuation (dots) and simulated attenuation (stars) of the filled fiber versus wavelength.

The dielectric tensor is approximated by using the full director field including the interaction with ε_{zz} . The parameter $\eta(E7)=1.66$ is used and σ is systematically varied. Investigations of E7-filled capillaries were reported in the literature. These results are discussed in the introduction and value of $\sigma \approx 1.7$ is

expected for an inclusion radius of 1.2 μm (Eq. 65). Numerous spectra are simulated and compared to the experimental spectrum (Fig. 65). Correlations of the experimental and simulated spectra are hardly seen if a single simulated spectrum is regarded. The simulated spectra have a larger number of peaks than the experimental spectrum. But the spectra vary systematically with σ and this helps to identify at least some interesting tendencies. The experimental spectrum shows a relatively broad transmission window from 650 to 750 nm. The simulations with high σ show no transmission windows in this spectral region. A broad transmission window shifts smoothly to this position with decreasing σ from the larger wavelength side. Thus, the region between $\sigma = 1$ and 2 is analyzed separately (Fig. 66).

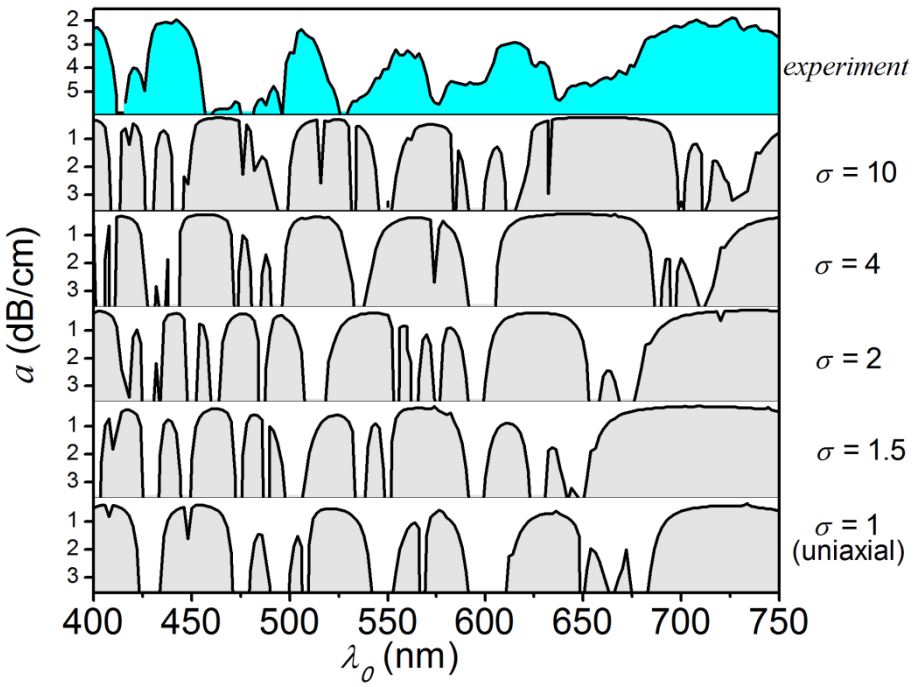

Fig. 65. Simulated attenuation spectra of fiber LMA-8 with perpendicular anchoring. The parameter σ (which describes the anchoring strength) is varied from 10 to 1. The experimental spectrum is shown as reference (top spectrum).

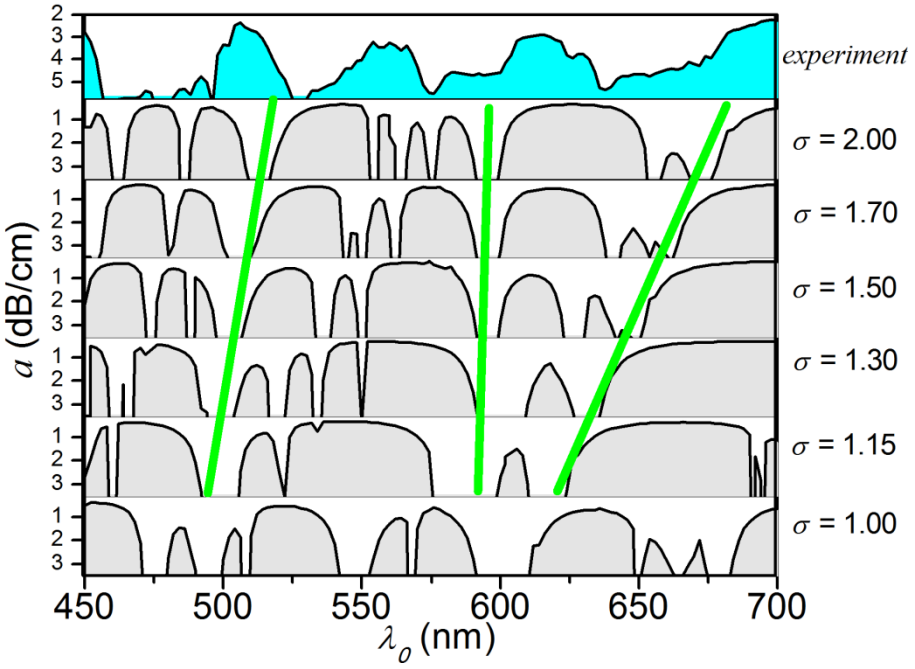

Fig. 66. The parameter σ is systematically varied from 2.00 to 1.00. The experimental spectrum of fiber LMA-8 with perpendicular anchoring (E7) is shown as reference (top spectrum). The simulated spectra are divided into 4 sections by green lines.

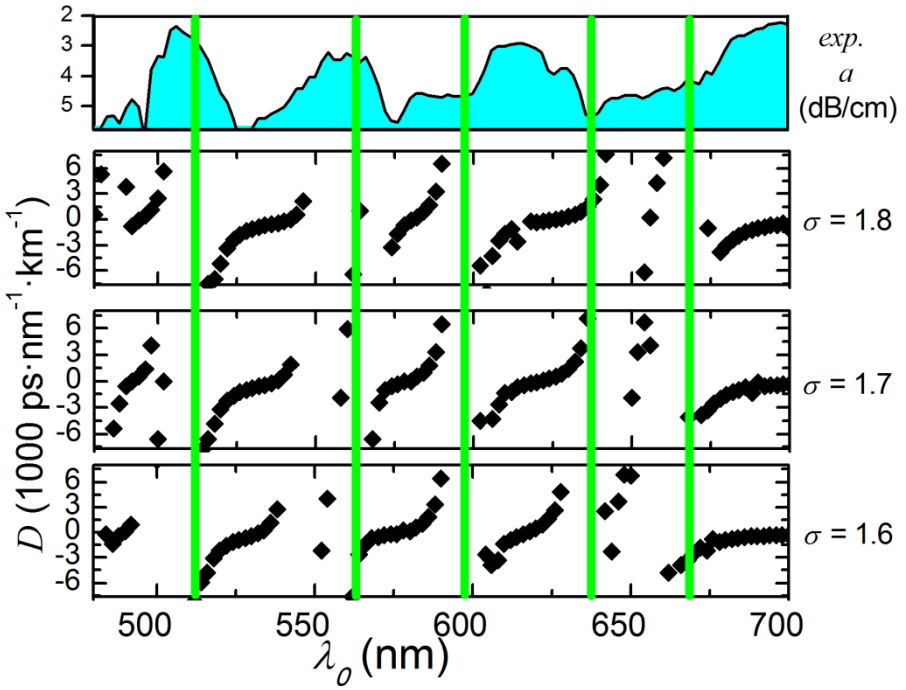

Fig. 67. The parameter σ is systematically varied from 1.8 to 1.6. The experimental spectrum of fiber LMA-8 with perpendicular anchoring (E7) is shown as reference (top spectrum). The simulated spectra are divided into 6 sections by green lines.

The simulated attenuation spectra show that even director fields with a weak escape lead to dramatic changes compared to the uniaxial case $\sigma = 1$. Varying σ in small steps between 1.3 and 2.0 reveals a more stable regime where the spectra share some common properties. The spectra in Fig. 66 are divided in 4 sections with green lines. The details of these regions vary. The lines are inserted to show the rather broad distances between the peaks of two neighboring regions. The chromatic dispersion is shown for $\sigma = 1.7 \pm 1$ in Fig. 67. These spectra show 6 photonic bandgaps. The bandgap at 650 nm is only roughly seen. A value of $\sigma \approx 1.7$ is expected from the analysis of single capillaries. With this information the experimental attenuation spectra of the fiber could maybe also be interpreted to show 6 transmission windows. In this case, the attenuation observed in the transmission windows around 590 and 650 nm would not be as low as in the other transmission windows.

5. Conclusions

In summary, the combination of experimental investigations and simulations led to a better understanding of the attenuation characteristics and the electro-optic switching behavior of liquid crystal-filled photonic crystal fibers with cylindrical liquid crystal inclusions and a solid core.

Such fibers with very homogeneous microstructures were systematically investigated. The fibers had different inclusion radii and the director orientation of the liquid crystals was varied by using two different anchoring agents. In addition to systematical studies with the well known liquid crystal E7, fields of special interest were investigated by using two further liquid crystals and one additional experimental fiber.

An appropriate spectroscopic setup was constructed for the experiments in order to transmit monochromatic light through the filled fibers and investigate the attenuation properties. The light of a Xenon-arc source is transmitted through a fiber coupled monochromator. The monochromatic light is delivered to the filled samples by an optical fiber with matching core diameter. The light-delivery fiber and the filled sample-fiber are then adjusted in order to exclusively transmit light through the glass core of the sample-fiber. The two fibers are spliced in an index matching environment of photo curable optical adhesive. Different detectors can be placed at the free end of the filled fiber.

The setup was tested in the visible and in the infrared spectral region. In the infrared spectral region, qualitative analysis is very well possible but an optical chopper setup would be required for quantitative measurements. However, the spectroscopic setup turned out to be perfectly suited for experiments in the visible spectral region where the emphasis of the current investigations is clearly settled.

A method was developed in order to fabricate rather long infiltrated fibers, so that the well-known cut-back technique could be applied. The latter technique is used to measure attenuation spectra that show exclusively the propagation loss of fibers, independent of the properties of the light source and the fiber splice. For the filled fibers, attenuations below 1 $dB \cdot cm^{-1}$ were observed in certain spectral regions. Already the different E7 filled photonic crystal fibers showed low-attenuation

windows for all wavelengths in the visible spectral region. The attenuation spectra of the filled fibers were dramatically influenced by simply using different anchoring agents. Even fiber pieces with a length as short as ≈ 1 cm showed a very pronounced spectral distribution of the transmitted intensity, so that spectral filters with a high contrast ratio are feasible. The observation of transmission windows with low attenuation is in promising contradiction to earlier observations on the wave guiding properties of liquid crystal-filled waveguides with rectangular shape [14], which indicated a very high attenuation in the entire visible wavelength range due to scattering losses. The microstructured fibers investigated in this work show a core with very high transmission, while losses are caused by scattering due to the liquid crystal inclusions.

The switching behavior of the filled fibers was investigated by coupling light into the waveguiding core region and applying a. c. signals across the fiber profile. The optical output power as a function of wavelength was observed.

Fibers filled with the liquid crystal E7 show highly interesting switching behavior. Electric fields were applied to the filled fibers across the profile by using a bipolar electrode setup. Above threshold, all fibers showed polarization independent responses where the light is completely attenuated in the waveguide once a voltage is applied.

The fields are commonly applied in *y*-direction. If so, the transmission of *x*-polarized light reappears at high voltages while *y*-polarized light is entirely attenuated after a propagation length of only 1.5 cm in fibers with parallel anchoring. A similar effect also occurred in a fiber with rather small inclusion radii in the case of perpendicular anchoring.

Especially the switching dynamics of the fibers with perpendicular anchoring of the liquid crystal are promising. The speed of an on/off-switching cycle of a Fredericks transition is often limited by the relaxation time constant t_{off}. Fortunately, the fibers with perpendicular anchoring showed extremely short time constants below 5 ms. Using very high addressing voltages in the range of $V > 200\ V_{rms}$, the speed of an on/off-switching cycle of an optical modulator based on such a fiber was enhanced by factor ≈ 5 compared to a fiber with planar anchoring.

In addition to the experiments, a simulation model was developed with a commercial available suite for electromagnetic field simulations [62]. The losses

were estimated with a model based on the scattering loss due to thermal fluctuations of the liquid crystal.

The simulation results were compared to well-known data in order to show the high accuracy of the model. This included the simulation of the well-known attenuation properties of a liquid crystal-filled waveguide with rectangular shape and anisotropic scattering properties.

The attenuation spectra of the liquid crystal-filled solid core photonic crystal fibers are simulated by taking into account the geometry and material parameters of the microstructure and the liquid crystal scattering loss mechanism.

The experimental attenuation spectra of the fibers with parallel anchoring of the liquid crystal were very well understood by a uniaxial model of the liquid crystal inclusions. The director fields of the inclusions with applied addressing voltages are not known. Nevertheless, strong similarities of experimental and simulated attenuation spectra were shown. In these simulations a director field was considered where the director had parallel anchoring at the glass boundaries of the inclusions but was aligned parallel to the addressing field lines near the center of the inclusions (circular planar polar director field [51]).

The attenuation spectrum of a fiber with perpendicular anchoring and an inclusion radius of 1.5 μm was simulated by using a two-dimensional projection of the escaped radial director field as approximation for the dielectric tensor inside the liquid crystal inclusions. Tendencies in the attenuation spectrum of a fiber with a smaller inclusion radius were understood at least partially by extensively varying the escape parameter of the escaped radial director field.

The experiments were extended to a liquid crystal mixture with low birefringence (MLC 6815) and a dual frequency addressable liquid crystal (ZLI 2461). These addressing experiments are even more advanced, in both cases. The index step between fused silica and MLC 6815 is smaller than between fused silica and E7. However, the polarization dependent response of the filled fiber was remarkable in the switching experiments. A four electrode setup was used to switch between two perpendicular linear polarizations at a wavelength around 630 nm.

In contrast to using such a low-birefringent liquid crystal, the switching behavior of fibers with planar anchoring was optimized by dual frequency addressing. Generally, fibers with planar anchoring showed short response times

(several ms) if applying a high voltage. But the response time for the relaxation is ≈4 times larger. The dual frequency addressable liquid crystal ZLI 2461 has been applied in fibers with planar anchoring to demonstrate active enhancement of the relaxation process. ZLI 2461 has a lower dielectric anisotropy than E7. Nevertheless, dual frequency addressing was applied to show that the time constant for the relaxation of ZLI 2461 filled fibers can be reduced by one third. For the same liquid crystal under the same anchoring conditions (ZLI 2461, planar anchoring), active on/off switching with an enhanced switching contrast was demonstrated in an experimental fiber where only the first two rings of inclusions had a homogeneous inclusion radius.

6. Outlook

Photonic crystal fibers with a solid core which is surrounded by a small number of rings of homogeneous cylindrical liquid crystal inclusions have been investigated systematically in the current work with emphasis on the visible spectral region. Possible applications of these fibers are situated in the field of fiber optics as switches or as linear polarizers. The polarizing effects of the presented fibers could also be very useful in telecommunication systems. However, investigations in the infrared spectral region are necessary in order to match the requirements of today's telecommunication systems.

Currently, the liquid crystals were applied selectively in the nematic phase. The results show already numerous important influence parameters. The number of rings for example is apparently sufficient in order to obtain windowed attenuation spectra and well developed switching effects. The fiber structure, the liquid crystal and the anchoring agents could nevertheless be varied in order to achieve similar effects at different wavelengths or new effects.

Varying the liquid crystal could lead to new types of active waveguides. For example, nematic liquid crystals with high negative dielectric anisotropy could be used to fill fibers with perpendicular anchoring. The liquid crystal director would align perpendicular to the field lines of an external electrical addressing field. Thus,

addressing fields could lead to a deformation of the director field by causing the director to realign parallel to the capillary long axis near the surface of the inclusions. This could lead to switching effects like the shift of the cladding bandgaps to higher or lower wavelength; the inclusion modes could possibly be shifted to smaller effective refractive indices. The resonances and thus the attenuation windows would be shifted to larger wavelengths in this case – potentially a very interesting polarization independent effect.

Moreover, the variety of liquid crystals is large. Ferroelectric liquid crystals, blue phases, smectic systems or biaxial nematics are only selected examples for liquid crystals which could be used in microstructured waveguides.

In contrast to variations of the filling mesophases, new fiber structures could be applied in order to make use of other waveguiding properties or to simplify the fabrication process. The highly wavelength dependent energetic crosstalk of a waveguiding core with high transmission and liquid crystal-filled inclusions with lower transmission can be expected to be useful in various kinds of microstructured fibers. The fibers investigated so far have a rather large number of liquid crystal inclusions and these inclusions are very well ordered. Maybe, this is not required for the occurrence of interesting tuning effects. Fiber structures which are simpler and have a lower number of inclusions than the photonic crystal fibers presented in the current work could possibly show interesting waveguiding properties as well.

Instead of varying the microstructure or the filling materials, also the electrode setup could be varied. For example, the field strength in the liquid crystal inclusions could be dramatically enhanced by a smaller distance of the electrodes. This could lead to dramatically lower threshold voltages.

7. Appendix

7.1 Dispersion of nematic liquid crystals

The refractive indices of a nematic liquid crystal are measured with a Jelly-type micro refractometer [72] where a slit which is illuminated with monochromatic light is observed through a wedge-cell. The wedge-cell is rubbed to provide a uniform alignment of the liquid crystal. Two virtual images are observed. Evaluation of these ordinary and extraordinary image yields both refractive indices of the liquid crystal. The dispersion of the refractive indices can be observed by measuring at different wavelengths.

The data obtained for E7 is compared to measurements reported in the literature [64] (Fig. 68). The refractive indices were currently measured at room temperature (25°C). The data reported in the literature [64] has been recorded at 30 °C. The curves fit well. However, the measurement method used in the literature [64] has a lower measurement failure (≈0.0002). The current failure is one order of magnitude higher (≈0.002) in the worst cases. The fitting parameters have lower deviations for the measurement with E7. The current measurement setup is still in an experimental state and further optimization can possibly lead to smaller deviations. Nevertheless, the current method is already very well suited to obtain data in order to be used in the simulations.

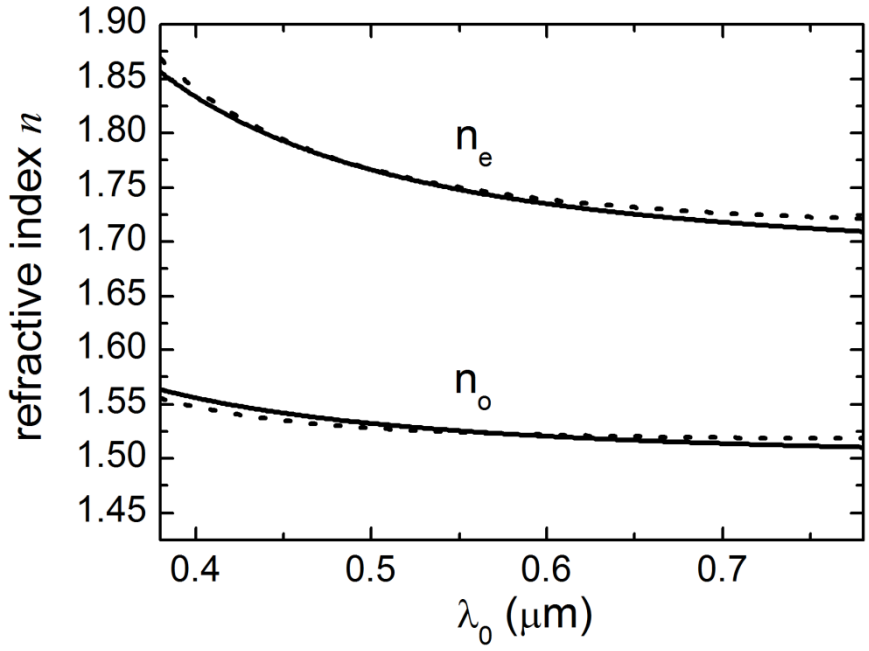

Fig. 68. Comparison of measured (dots) and reported [64] (solid line) refractive indices of E7.

The Cauchy coefficients of the dual frequency addressable liquid crystal ZLI 2461 are not yet provided in the literature[23]. The measurement results are shown in Fig. 69.

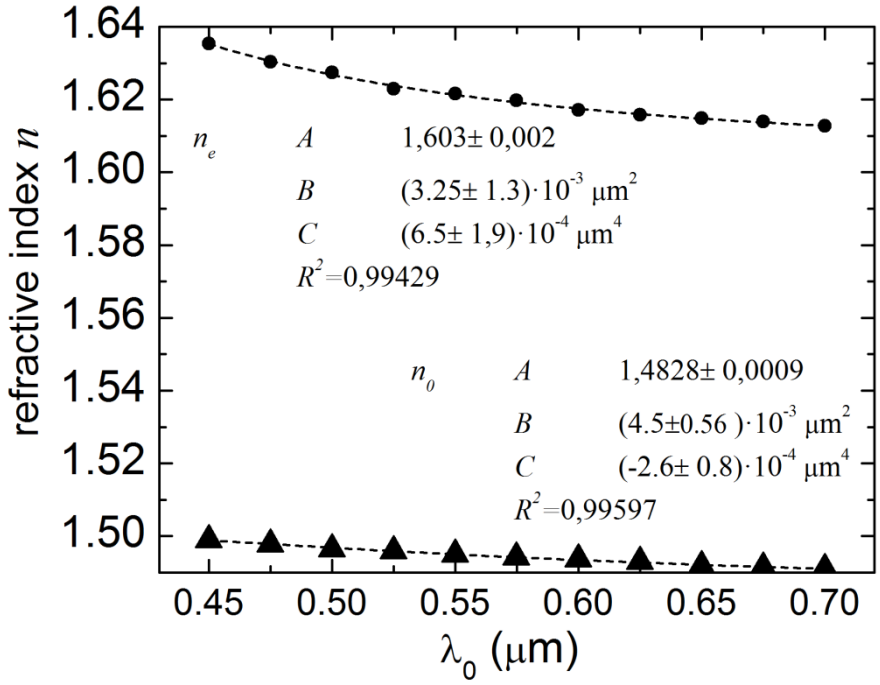

Fig. 69. Measured refractive indices of ZLI 2461 over the wavelength in μm. The Cauchy model is fitted to the experimental data.

[23] According to [LiqCryst 4.7] (2009)

7.2 Time averaged flux of electromagnetic energy

The Poynting vector $\vec{S}$ represents the energy flux density of the electromagnetic field [4]. The direction and magnitude of the Pointing vector are accessible with Eq. 101:

$$\vec{S} = \vec{E} \times \vec{H}. \qquad \text{(Eq. 99)}$$

A plane wave propagating in a material with the refractive index n is formulated for the electric and the magnetic field. The special dependence of the plane wave is represented by a complex spatial amplitude (phasor):

$$\vec{E}_{pw} = \vec{E}_0 \cos(\omega t - \varepsilon_r^2 \vec{k}\vec{r}) = \mathrm{Re}\left(\vec{E}_0 e^{-j\varepsilon_r^2 \vec{k}\vec{r}} e^{j\omega t}\right) = \mathrm{Re}\left(\vec{E}_{sp} e^{j\omega t}\right), \qquad \text{(Eq. 100)}$$

$$\vec{H}_{pw} = \vec{H}_0 \cos(\omega t - \varepsilon_r^2 \vec{k}\vec{r}) = \mathrm{Re}\left(\vec{H}_0 e^{-j\varepsilon_r^2 \vec{k}\vec{r}} e^{j\omega t}\right) = \mathrm{Re}\left(\vec{H}_{sp} e^{j\omega t}\right). \qquad \text{(Eq. 101)}$$

The real part of a complex number is defined as the half of the sum of the number with the corresponding complex conjugate. The Poynting vector at a fixed location is thus obtained for a plane wave:

$$\begin{aligned} \vec{S} &= \vec{E}_{pw} \times \vec{H}_{pw} = \frac{1}{2}\left(\vec{E}_{sp} e^{j\omega t} + \vec{E}_{sp}^{*} e^{-j\omega t}\right) \times \frac{1}{2}\left(\vec{H}_{sp} e^{j\omega t} + \vec{H}_{sp}^{*} e^{-j\omega t}\right) \\ \Leftrightarrow \vec{S} &= \frac{1}{4}\left(\vec{E}_{sp} \times \vec{H}_{sp} e^{2j\omega t} + \vec{E}_{sp} \times \vec{H}_{sp}^{*} + \vec{E}_{sp}^{*} \times \vec{H}_{sp} + \vec{E}_{sp}^{*} \times \vec{H}_{sp}^{*} e^{-2j\omega t}\right) \qquad \text{(Eq. 102)} \\ \Leftrightarrow \vec{S} &= \frac{1}{2}\mathrm{Re}\left(\vec{E}_{sp} \times \vec{H}_{sp}^{*}\right) + \frac{1}{2}\mathrm{Re}\left(\vec{E}_{sp} \times \vec{H}_{sp} e^{2j\omega t}\right). \end{aligned}$$

The first summand of Eq. 102 shows no time dependence. Interestingly, the second summand shows that the energy flux density oscillates with the double frequency of the fields. However, the time average of the exponential $e^{2j\omega t}$ is zero. Thus, the term $\frac{1}{2}\mathrm{Re}\left(\vec{E}_{sp} \times \vec{H}_{sp}^{*}\right)$ is the time average $\bar{S}$ of the energy flux density. The very same formula is obtained from a complex formulation of the Pointing vector:

$$\begin{aligned} \vec{S}_c &= \frac{1}{2}\left(\vec{E}_{sp} \times \vec{H}_{sp}^{*}\right) \\ \Rightarrow \bar{S} &= \mathrm{Re}\left(\vec{S}_c\right) = \frac{1}{4}\left(\left(\vec{E}_{sp} \times \vec{H}_{sp}^{*}\right) + \left(\vec{E}_{sp}^{*} \times \vec{H}_{sp}\right)\right) = \frac{1}{2}\mathrm{Re}\left(\vec{E}_{sp} \times \vec{H}_{sp}^{*}\right). \end{aligned} \qquad \text{(Eq. 103)}$$

For these reasons, the formulation for the time averaged flux of energy considers complex valued amplitudes $\vec{E}_{ph}$ and $\vec{H}_{ph}{}^{*}$ instead of the real valued fields:

$$\bar{S} = \frac{1}{2}\mathrm{Re}\left(\vec{E}_{ph} \times \vec{H}_{ph}{}^{*}\right). \qquad \text{(Eq. 16)}$$

7.3 Contributions in peer reviewed journals

A. Lorenz, R. Schuhmann, H.-S. Kitzerow, "Switchable waveguiding in two liquid crystal-filled photonic crystal fibers," Appl. Opt. **49**, 3846–3853 (2010).

A. Lorenz, R. Schuhmann, H.-S. Kitzerow, "Infiltrated photonic crystal fiber: experiments and liquid crystal scattering model," Opt. Express **18**, 3519-3530 (2010).

A. Lorenz, H.-S. Kitzerow, A. Schwuchow, J. Kobelke, H. Bartelt, "Photonic crystal fiber with a dual-frequency addressable liquid crystal: behavior in the visible wavelength range," Opt. Express **16**, 19375-19381 (2008).

H.-S. Kitzerow, A. Lorenz, H. Matthias, "Tuneable photonic crystals obtained by liquid crystal infiltration", physica status solidi (a) **11** (204), 3754-3767 (2007).

7.4 Conference Contributions

7.4.1 Oral Contributions

(presenting author underlined)

A. Lorenz, R. Schuhmann, H.-S. Kitzerow, "Switchable waveguiding in liquid crystal filled photonic crystal fibers," Convention of the DFG Graduate Program 1464, Paderborn (Mai 27 - 28, 2010).

A. Lorenz, R. Schuhmann, H.-S. Kitzerow, "Liquid crystal infiltrated photonic crystal fibers," DPG Frühjahrstagung der Sektion Kondensierte Materie (SKM), Regensburg (March 21. - 26. 2010).

A. Lorenz, R. Schuhmann, H.-S. Kitzerow, "Waveguiding in infiltrated photonic crystal fibers: experiments and liquid crystal scattering model," 38th Topical Meeting on Liquid Crystals, Mainz (March 10. - 12. 2010).

A. Lorenz, R. Schuhmann, H.-S. Kitzerow, "Scattering in liquid crystals and the useful application in switchable waveguides," Convention of the DFG Graduate Program 1464, Bad Karlshafen (November 26 - 27, 2009).

A. Lorenz, H.-S. Kitzerow, "Switchable waveguides based on optically anisotropic photonic band gap structures for visible and near infrared light," Convention of the DFG Graduate Program 1464, Gehrden (May, 7 - 8, 2009).

A. Lorenz, H.-S. Kitzerow, "Photonic Crystal Fibers filled with Liquid Crystals - Switchable Waveguides in the Visible and Infrared Spectral Region," JCF-Spring symposium (Frühjahrssymposium) March (11 – 14, 2009).

A. Lorenz, H.-S. Kitzerow, A. Schwuchow, J. Kobelke, H. Bartelt, "Photonic crystal fibers filled with Liquid Crystals," International liquid crystal conference 2008, Jeju Island Korea (June 29 – July 4, 2008).

7.4.2 Poster Contributions

A. Lorenz, R. Schuhmann, H.-S. Kitzerow, "Modal Dispersion of Waveguides with Escaped Radial Director Fields: ARROW-Study Of Tunable Photonic Crystal Fibers," 37th Topical Meeting on Liquid Crystals, Stuttgart (April 1 - 3, 2009).

A. Lorenz, H.-S. Kitzerow, A. Schwuchow, J. Kobelke, H. Bartelt, "Photonic Crystal Fiber with Dual Frequency Response," 37th Topical Meeting on Liquid Crystals, Stuttgart (April 1 – 3, 2009).

A. Lorenz, H.-S. Kitzerow, A. Schwuchow, J. Kobelke, H. Bartelt, "Photonic crystal fibers filled with liquid crystals - fibers with active cladding," KSOP Summer School, Bad Herrenalb (August 20 -21, 2008).

A. Lorenz, H.-S. Kitzerow, A. Schwuchow, J. Kobelke, H. Bartelt, "Photonic crystal fibers filled with liquid crystals - fibers with active cladding," International liquid crystal conference 2008, Jeju Island Korea (June 29 – July 4, 2008).

A. Lorenz, H.-S. Kitzerow, "Photonic crystal fibers filled with liquid crystals - band gap fibers with active cladding," 36th Topical Meeting on Liquid Crystals, Magdeburg (March 12 – 14, 2008).

References

1. "The Nobel Prize in Physics 2009," Press release of the Royal Swedish Academy of Sciences, 6. October 2009 (http://nobelprize.org/nobel_prizes/physics/laureates/2009/press.html).
2. J. A. Buck in "Fundamentals of Optical Fibers," ISBN 0-471-30818-8, John Wiley & Sons, New York (1995).
3. D. Gloge, "Weakly Guiding Fibers," Appl. Opt. 10, 2252-2258 (1971).
4. W. Demtröder, "Experimentalphysik 2," 3rd edition, ISBN 3-540-20210-2, Springer publishing (2004).
5. P. S. J. Russell, "Photonic-Crystal Fibers," J. Lightwave Technol. **24**, 4729-4749 (2006).
6. A. Bjarklev, J. Broeng, and A. S. Bjarklev in "Photonic Crystal Fibers," ISBN 978-1402076107, Springer, Berlin (2003).
7. S. Fevrier, R. Jamier, J.M. Blondy, S.L. Semjonov, M.E. Likhachev, M.M. Bubnov, E.M. Dianov, V.F. Khopin, M.Y. Salganskii, and Guryanov, "Low-loss singlemode large mode area all-silica photonic bandgap fiber," Opt. Express **14**, 562–569 (2006).
8. J. D. Joannopoulos, S. G. Johnson, and J. N. Winn in "Photonic crystals: Molding the flow of light," second edition ISBN 978-0691124568, Princeton Univ Press (2008).
9. A. Argyros, T. A. Birks, S. G. Leon-Saval, C. M. B. Cordeiro, F. Luan, P. S. J. Russell, "Photonic bandgap with an index step of one percent," Opt. Express **13**, 309–314 (2005).
10. T. A. Birks, G. J. Pearce, D. M. Bird, "Approximate band structure calculation for photonic bandgap fibres," Opt. Express **14**, 9483-9490 (2006).
11. N. M. Litchinitser, S. C. Dunn, B. Usner, B. J. Eggleton, T. P. White, R. C. McPhedran, C. M. de Sterke, "Resonances in microstructured optical waveguides," Opt. Express **11**, 1243–1251(2003).
12. N. M. Litchinitser, A. K. Abeeluck, C. Headley, B. J. Eggleton, "Antiresonant reflecting photonic crystal optical waveguides," Opt. Lett. **27**, 1592-1594 (2002).
13. M. A. Schmidt, N. Granzow, N. Da, M. Peng, L. Wondraczek, P.S.J. Russell, "All-solid bandgap guiding in tellurite-filled silica photonic crystal fibers," Opt. Lett. **34** (2009).
14. C. Hu, J. R. Whinnery, "Losses of a Nematic Liquid-Crystal Optical-Waveguide," J. Opt. Soc. Am. **64**, 1424–1432 (1974).
15. M. Green, s. J. Madden, "Low loss nematic liquid crystal cored fiber waveguides," Appl. Opt. 5202-5203 (1989).
16. P. G. De Gennes in "The Physics of Liquid Crystals", second edition, Clarendon Press, Oxford, ISBN 0 19 8520247 (1993).
17. T. T. Larsen, A. Bjarklev, D. S. Hermann, and J. Broeng, "Optical devices based on liquid crystal photonic bandgap fibres," Opt. Express **11**(20), 2589–2596 (2003).
18. J. Du, Y. Liu, Z. Wang, B. Zou, B. Liu, and X. Dong, "Liquid crystal photonic bandgap fiber: different bandgap transmissions at different temperature ranges," Appl. Opt. **47** (29), 5321–5324 (2008).
19. W. Yuan, L. Wei, T. T. Alkeskjold, A. Bjarklev, and O. Bang, "Thermal tunability of photonic bandgaps in liquid crystal infiltrated microstructured polymer optical fibers," Opt. Express **17**(22), 19356–19364 (2009).

20. L. Wei, L. Eskildsen, J. Weirich, L. Scolari, T. T. Alkeskjold, and A. Bjarklev, "Continuously tunable all-in-fiber devices based on thermal and electrical control of negative dielectric anisotropy liquid crystal photonic bandgap fibers," Appl. Opt. **48**(3), 497–503 (2009).
21. T. R. Wolínski, K. Szaniawska, S. Ertman, P. Lesiak, A. W. Domanski, R. Dabrowski, E. Nowinowski-Kruszelnicki, and J. Wojcik, "Influence of temperature and electrical fields on propagation properties of photonic liquid-crystal fibres," Meas. Sci. Technol. **17** (5), 985–991 (2006).
22. T. R. Woliński, S. Ertman, A. Czapla, P. Lesiak, K. Nowecka, A. W. Domański, E. Nowinowski-Kruszelnicki, R. Dabrowski, and J. Wójcik, "Polarization effects in photonic liquid crystal fibers," Meas. Sci. Technol. **18**(10), 3061–3069 (2007).
23. C.-H. Lee,C.-H. Chen,C.-L- Kao,C.-P. Yu, S.-M- Yeh, W.-H. Cheng, T.H. Lin, "Photo and electrical tunable effects in photonic liquid crystal fiber," Opt. Express **13**, 2814-2821 (2010).
24. F. Du, Y.Q. Lu, S.T. Wu, "Electrically tunable liquid-crystal photonic crystal fiber," Apl. Phys. Lett. **85**, 2181-2183 (2004).
25. Thomas Tanggaard Alkeskjold, Anders Bjarklev, "Electrically controlled broadband liquid crystal photonic bandgap fiber polarimeter," Opt. Lett. **32**, 1707-1709 (2007).
26. J. Weirich, J. Laegsgaard, L. Scolari, L. Wei, T.T. Alkeskjold, A. Bjarklev, "Biased liquid crystal infiltrated photonic bandgap fiber," Optics Express **17**, 4442–4453 (2009).
27. L. Scolari, T.T. Alkeskjold, J. Riishede and A. Bjarklev, "Continuously tunable devices based on electrical control of dual-frequency liquid crystal filled photonic bandgap fibers," Opt. Express **13**, 7483-7496 (2005).
28. M. W. Haakestad, T. T. Alkeskjold, M. D. Nielsen, L. Scolari, J. Riishede, H. E. Engan and A. Bjarklev, "Electrically tunable photonic bandgap guidance in a liquid-crystal-filled photonic crystal fiber," IEEE Phot. Tec. Lett. **17**, 819-821 (2005).
29. A. Lorenz, H.-S. Kitzerow, A. Schwuchow, J. Kobelke, H. Bartelt, "Photonic crystal fiber with a dual-frequency addressable liquid crystal: behavior in the visible wavelength range," Opt. Express **16**, 19375-19381 (2008).
30. H. Matthias, A. Lorenz, H.-S. Kitzerow, "Tuneable photonic crystals obtained by liquid crystal infiltration," phys. stat. sol. A **11**, 3754-3767 (2007).
31. S. Ertman, T.R. Wolinski, D. Pysz, R. Buczynski, E. Nowinowski-Kruszelnicki, R. Dabrowski, "Low-loss propagation and continuously tunable birefringence in high-index photonic crystal fibers filled with nematic liquid crystals," Opt. Express **17**, 19298-19310 (2009).
32. T. T. Alkeskjold, J. Lægsgaard, A. Bjarklev, D. S. Hermann, A. Anawati, J. Broeng, J. Li, and S. T. Wu, "Alloptical modulation in dye-doped nematic liquid crystal photonic bandgap fibers, " Opt. Express **12**(24), 5857-5871 (2004).
33. J. Sun, C.C. Chan, N. Ni, "Analysis of photonic crystal fibers infiltrated with nematic liquid crystal," Opt. Comm. **278**, 66–70 (2007).
34. C. L. Xu, W. P. Huang, J. Chrostowski, S.K. Chaudhuri, "A full-vectorial beam propagation method for anisotropic waveguides," J. Lightw. Technol. **12**, 1926–1931 (1994).
35. S.-M. Hsu, H.-C. Chang, "Characteristic investigation of 2D photonic crystals with full material anisotropy under out-of-plane propagation and liquid-crystal-filled photonic-band-gap-fiber applications using finite element methods," Opt. Express **16**, 21355–21368 (2008).
36. G. Tartarini, T. Alkeskjold, L. Scolari, A. Bjarklev, P. Bassi, "Spectral properties of liquid crystal photonic bandgap fibres with splay-aligned mesogens," Opt. Quant. Electron. **39**, 913–925 (2007).

37. A. Lorenz, R. Schuhmann, H.-S. Kitzerow, "Infiltrated photonic crystal fiber: experiments and liquid crystal scattering model," Opt. Express **18**, 3519-3530 (2010).
38. C. Caloz, T. Itoh in "Electromagnetic Metamaterials," ISBN 0-471-66985-7, John Wiley & Sons, Inc., Hoboken, New Jersey (2006).
39. R. Paschotta in "Encyclopedia of Laser Physics and Technology," http://www.rp-photonics.com/modes.html, (07.04.2010).
40. D. J. Channin, "Optical waveguide modulation using nematic liquid crystal," Appl. Phys. Lett. **22**, 365–366 (1973).
41. T. G. Euser, M. K. Garbos, J. S. Y. Chen, P. St. Russel, "Precise balancing of viscous and radiation forces on a particle in liquid-filled photonic bandgap fiber," opt. Lett. 34, 3674-3676 (2009).
42. Alexander Lorenz, Rolf Schuhmann, Heinz-Siegfried Kitzerow, "Switchable waveguiding in two liquid-crystal-filled photonic crystal fibers," Appl. Opt. **49**, 3846-3853 (2010).
43. G. B. Ren, P. Shum, L. R. Zhang, X. Yu, W.J. Tong, J. Luo, "Low-loss all-solid photonic bandgap fiber," Opt. Lett. **32**, 1023–1025 (2007).
44. Ger Vertogen, Wim H. de Jeu in "Thermotropic Liquid Crystals, Fundamentals, ", ISBN 3-540-17946-1, Springer-Press, Berlin Heidelberg New York (1985).
45. H. Stegemeyer and guest. ed. in "Liquid Crystals," ISBN 0-387-91421-8, Steinkopff (1994).
46. F. C. Franck, "On the theory of liquid crystals," Discuss. Faraday Soc. **25**, 19-28 (1958).
47. S. T. Wu, "Absorption measurements of liquid crystals in the ultraviolet, visible, and infrared," Journal of Applied Physics **84**, 4462–4465 (1998).
48. P. G. de Gennes, "Long Range Order and Thermal Fluctuations in Liquid Crystals," Mol. Cryst. Liq. Cryst. **7**, 325–345 (1969).
49. D. Langevin, M.A. Bouchiat, "Anisotropy of the turbidity of an oriented nematic liquid crystal," Journal de Physique Colloques, C197 (1975).
50. G. P. Crawford and S. Žumer, "Liquid Crystals in Complex Geometries: Formed by Polymer and Porous Networks," Crc. Pr. Inc. , ISBN 978-0748404643 (1996).
51. S.V. Burylov, "Equilibrium configuration of a nematic liquid crystal confined to a cylindrical cavity," JETP **85**, 873–886 (1997).
52. G.P. Crawford, D.W. Allender, J.W. Doane, "Surface elastic and molecular-anchoring properties of nematic liquid crystals confined to cylindrical cavities," Phys. Rev. A **45**, 8693-8708 (1992).
53. H. Matthias, S. L Schweizer, R. B. Wehrspohn, H.-S. Kitzerow, "Liquid crystal director fields in micropores of photonic crystals," Journal of Optics A: Pure and Applied Optics **9**, S389 (2007).
54. H. Matthias, A. Lorenz, H.-S. Kitzerow, "Tuneable photonic crystals obtained by liquid crystal infiltration," phys. stat. sol. A **11**, 3754-3767 (2007).
55. R. D. Polak, G. P. Crawford, B. C. Kostival, J.W. Doane, S. Zumer, "Optical determination of the saddle-splay elastic constant K24 in nematic liquid crystals," Phys. Rev. E **49**, R978-R981 (1994).
56. M. Gu, S.V. Shiyanovskii, O.D. Lavrentovich, "Polarity-Dependent Dielectric Torque in Nematic Liquid Crystals," Phys. Rev. Lett. **100**, 237801 (2008).
57. D. S. Kliger, J. W. Lewis, C. E. Randall, "Polarized light in optics and spectroscopy, " ISBN 0-12-414975-8, Acad. Press Boston (1990).
58. F. Xu, H.S. Kitzerow, P.P. Crooker, "Electric-field effects on nematic droplets with negative dielectric anisotropy," Phys. Rev. A **46**, 6535-6540 (1992).

59. H.S. Kitzerow, B. Liu, F. Xu, P.P. Crooker, "Effect of chirality on liquid crystals in capillary tubes with parallel and perpendicular anchoring," Phys. Rev. E **54**, 568-575 (1996).
60. M. Schadt, "Low-Frequency Dielectric Relaxations in Nematics and Dual-Frequency Addressing of Field Effects," Mol. Cryst. Liq. Cryst. **89**, 77-92 (1982).
61. H. K. Bücher, R. T. Klingbiel, J. P. VanMeter, "Frequency-addressed liquid crystal field effect," Appl. Phys. Lett. **25**, 186-188 (1974).
62. COMSOL 3.5a, Comsol Multiphysics®, http://www.comsol.com.
63. K. Simonyi in "Foundations of Electrical Engineering," (Elsevier 1964).
64. G. Abbate, V. Tkachenko, A. Marino, F. Vita, M. Giocondo, A. Mazzulla, L. De Stefano, "Optical characterization of liquid crystals by combined ellipsometry and half-leaky-guided-mode spectroscopy in the visible-near infrared range," J. Appl. Phys. **101**, 73105 (2007).
65. J. Jasapara, T.H. Her, R. Bise, R. Windeler, D.J. DiGiovanni, "Group-velocity dispersion measurements in a photonic bandgap fiber," JOSA B **20**, 1611–1615 (2003).
66. Manual of the Comsol RF-module (http://www.comsol.com).
67. O. V. Butov, K. M. Golant, A. L. Tomashuk, M. J. N. van Stralen, A. H. E. Breuls, "Refractive index dispersion of doped silica for fiber optics," Optics Communications **213**, 301–308 (2002).
68. M.A. Khashan, A.Y. Nassif, "Dispersion of the optical constants of quartz and polymethyl methacrylate glasses in a wide spectral range: 0.2-3 μm," Optics Communications **188**, 129–139 (2001).
69. G. Ronald Hadley, "Transparent boundary condition for beam propagation," Opt. Lett. **16**, 624-626 (1991).
70. J.-P. Berenger, "A perfectly matched layer for the absorption of electromagnetic waves," J. Comp. Phys. **114**, 185–200 (1994).
71. M.A. Duguay, Y. Kokubun, T. L. Koch, L. Pfeiffer, "Antiresonant Reflecting Optical Wave-Guides in SiO_2-Si Multilayer Structures," Appl. Phys. Lett. **49**, 13–15 (1986).
72. A. E. Edwards, C. E. Otto, "A Microrefractometer of Sample Design," Industrial & Engineering Chemistry Analytical Edition **10**, 225–226 (1938).